# Rydberg spectroscopy in a gas of ultracold Ytterbium atoms

Inaugural-Dissertation

zur

Erlangung des Doktorgrades der

Mathematisch-Naturwissenschaftlichen Fakultät

der Heinrich-Heine-Universität Düsseldorf

vorgelegt von

**Christian Halter**

aus Hanau

Düsseldorf, Oktober 2021

Aus dem Institut für Experimentalphysik
der Heinrich-Heine-Universität Düsseldorf

Gedruckt mit der Genehmigung der
Mathematisch-Naturwissenschaftlichen Fakultät der
Heinrich-Heine-Universität Düsseldorf

| | |
|---|---|
| Referent: | Prof. Dr. Axel Görlitz |
| Koreferent: | Prof. Dr. Thomas Heinzel |
| Tag der mündlichen Prüfung: | 21.03.2022 |

# Abstract

Rydberg atoms [1] with their fascinating properties have become of great interest in quantum optics. Particularly ultra cold Rydberg atoms with their strong interaction are a promising tool for quantum simulations and information processing [2].

In recent years, Rydberg atoms with two valence electrons have further expanded the already diverse range of applications [3][4][5][6]. Here I present a study of ultra cold ytterbium Rydberg atoms. Another promising atom species, which could expand the range of applications even further.

In the scope of this thesis I present a simple and robust spectroscopy, the MOT depletion spectroscopy. With this technique it was possible to excite and identify several Rydberg states of Yb which had not been measured before and confirm already identified states [7]. With the MOT depletion method it is also possible to determine the polarizabilities of $^1S_0$ and $^1P_1$ Rydberg series. The measured polarizabilities were compared with numerically determined values, using a semi-classical model [8]. Both, the measurements and the numerical values are consistent with each other.

To gain further knowledge about the Yb Rydberg states we also implemented the electric field ionization spectroscopy. This spectroscopy allows to study the ionization behavior of the Yb Rydberg states of the $^1S_0$ and $^1D_2$ series. The exploration of the ionisation process revealed a diabatic and adiabatic passages of the bound Rydberg states through the Stark manifold before they ionize.

The electric field ionization method gives also the opportunity to measure the black-body reduced lifetimes of the Yb Rydberg states. These lifetimes are important information as they provide a time frame for further experiments. The measured black-body reduced lifetimes of the $^1S_0$ and $^1D_2$ series are presented and discussed in this thesis.

# Contents

# List of Figures

# 1.

# Introduction

The study of Rydberg atoms with their astonishing properties, has established itself in many areas of physics. This includes e.g. molecular physics, plasma physics, quantum information and many more. Most of the studies on Rydberg atoms have to date used alkali atoms. The goal of this thesis is to expand the already wide field of Rydberg physics by exploring the special features of Rydberg atoms with two valence electrons, which have recently attracted significant attention. More precisely, this thesis is concerned with the spectroscopy of laser-cooled ytterbium Rydberg atoms.

The two valence electron atom species like ytterbium (Yb), which has an electronic structure that is similar to alkaline earth metal, open the opportunity to perform fundamentally different experiments in the field of cold Rydberg physics. The presence of two valence electrons gives a variety of opportunities. For example the access to singlet and triplet states, which exhibits a wide range of attractive or repulsive interactions [9]. It also provides with its weak intercombination lines an advantageous opportunity for laser cooling to very low temperatures and for Rydberg specific applications like Rydberg dressing [10]. Another possibility is to trap Rydberg atoms and ground state atoms simultaneously [11]. These kind of traps have the potential to serve as a model system for a superconducting metal-like state [12]. The second electron gives also the opportunity to address the Rydberg atom optically due to the optical active core, which allows for optical imaging of the ultra cold Rydberg gas [9].

For all of these applications a detail of knowledge of the structure of the Rydberg atom

is mandatory. The goal of this thesis is to set the foundation for future experiments by studying fundamental properties of Yb Rydberg states. The structure of the energy levels is investigated spectroscopically and the response of the states to external electric field is studied. These studies allow for the determination of the polarizability and ionization thresholds of Yb Rydberg states. Another property, which is investigated in this thesis, is the lifetime of Rydberg states. All these properties of Yb Rydberg states are measured and discussed in the context of this thesis.

In this introductory chapter I will first give a short overview over current developments in the field of ultracold Rydberg physics. Subsequently, I will explain the specific features of Yb that makes it a good candidate for the mentioned study of new phenomena.

## 1.1. Rydberg physics

In recent years, Rydberg states, atomic states of high principal quantum number $n$, have become of great interest in the field of quantum optics. Their properties like the polarizability, the lifetime or just their size are exaggerated compared to low-lying states. The reason for this drastic increase is the scaling of the properties with the principal quantum number $n$. Some of the scaling laws can be seen in table 1.1.

**Table 1.1.:** Scaling laws of Rydberg states. Reproduced from [1]

| | |
|---|---|
| Binding energy | $n^{-2}$ |
| Energy between adjacent $n$ states | $n^{-3}$ |
| Orbital radius | $n^2$ |
| Dipole moment | $n^2$ |
| Polarizability | $n^7$ |
| Radiative lifetime | $n^3$ |
| Dipole-Dipole interaction | $n^{11}$ |

One of the most interesting properties of Rydberg atoms is the interaction strength between Rydberg atoms. As can be seen in table 1.1 the dipole-dipole interaction of Rydberg atoms scales with $n^{11}$. This drastic scaling leads to new binding mechanism between Rydberg atoms in highly excited states [13]. Another effect that arises from the

dipole-dipole interaction is the so called "dipole blockade", which will be briefly explained below. With this effect it is possible to switch off interactions, which can be used to implement controlled-NOT (CNOT) gates in a quantum computing environment with neutral atoms [14]. The dipole blockade opens also the possibility for the formation of complex many-body systems, which will be introduced below.

The interaction between Rydberg atoms and ground state atoms can also lead to the formation of exotic molecules [15]. One example for such a molecule is the excitation of a single Rydberg atom in a Bose-Einstein condensate (BEC) of strontium [3]. In the condensate the long range interactions of the Rydberg atom leads to binding mechanism between hundreds of ground state atoms and a single Rydberg atom. This ultra long range Rydberg molecule gives the opportunity to study collective phenomena in degenerated gas, like the formation of polarons [5].

Besides the interaction between Rydberg atoms, the properties of a Rydberg atom alone offers interesting opportunities to study fundamental quantum physics. One example is a circular Rydberg state. These Rydberg states have a huge principal quantum $n = 300 \rightarrow 600$ as well with a giant orbital momentum ($m_l \approx l \approx n$). The electron wavefunction of these states is orbiting the ionic core in a Bohr-like way and this enables the test of fundamental quantum decoherence [16].

Exploiting these interaction mechanism and unique properties leads also to several other interesting phenomenona, which will not be discussed in detail in this thesis. Some of these interesting phenomenona are a single photon source at room temperature [17] or the formation of anti-hydrogen via an electron cascade caused through Rydberg states [18].

#### Dipole blockade

As described in [19] the strong dipole-dipole interaction between Rydberg atoms causes a shift in the energy levels of surrounding atoms. If the shift is larger than the laser line width of the laser used to excite the Rydberg state, other excitations in the vicinity of

the Rydberg atom are suppressed, which is illustrated in figure 1.1. The blockade of the excitation of the surrounding ground state atoms, if one atom is excited to a Rydberg state, plus the Rydberg atom itself can also be interpreted as shared excitation. This mesoscopic state is often called "superatom"[20].

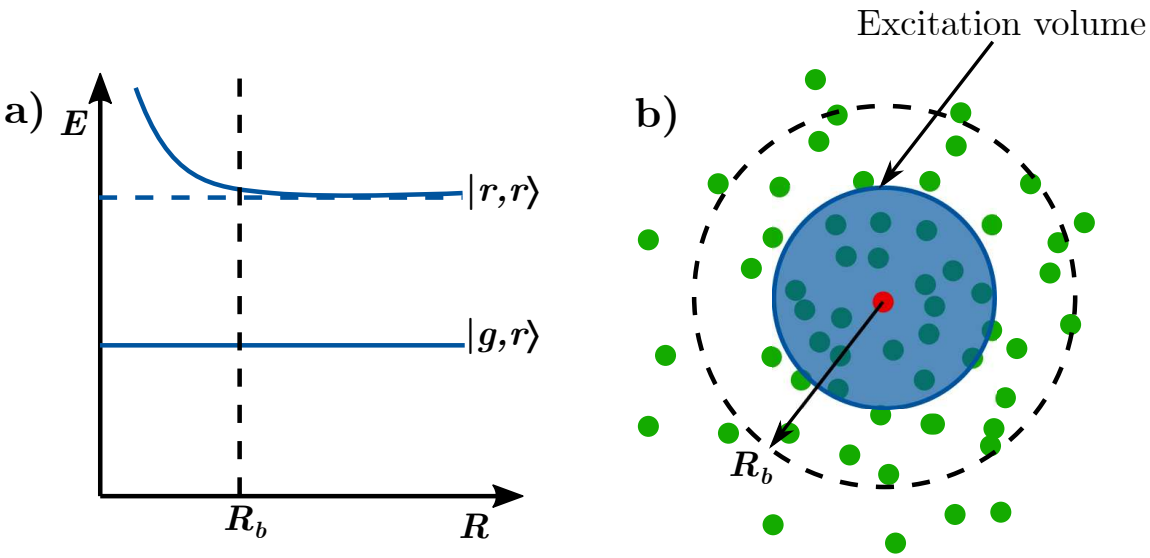


**Figure 1.1.:** *Schematic view of the dipole blockade. a) Energy level scheme of an atom in the vicinity of a Rydberg atom. The energy level of the ground state $|g\rangle$ is not effected by the Rydberg atom. Due to the large dipole interaction the Rydberg state $|r\rangle$ is shifted to a higher energy as the distance decreases. The excitation becomes inaccessible below the blockade radius $R_b$. b) Example of a single Rydberg excitation due to the dipole blockade. There is only one excitation because the excitation volume is smaller than the blockade volume and the atom cloud.*

The shift of the energy levels can also be used to achieve the exact opposite mechanism, an anti-blockade. In this case the excitation laser is detuned in such a way, that the shift of the energy levels caused by the dipole-dipole interaction of a Rydberg atom with the ground state atom compensates the detuning of the excitation laser. This anti-blockade effect causes an avalanche of excitations which results in a formation of an ultra cold neutral plasma [21].

As already mentioned the dipole blockade can be used to implement a CNOT gate, which has been demonstrated by [22]. In that work a CNOT gate is realized by coupling two individually addressed neutral atoms via the dipole mechanism [23] with a CNOT fidelity of 0.73.

#### Many-body systems

In recent studies of superatom states, it was found that the correlation between many superatom states are preserved over large distances [24]. These many-body systems have very complex excitation dynamics and therefore the initial conditions have to be controlled precisely. However in the work of [25] and [26] it was still possible to show a collective behavior of superatom states for traps of different shapes. In [25] it was possible to generate a collective entangled state of a superatom over an entire ring shaped optical trap. In [26] a crystallization effect of superatoms was found in an optical lattice.

In general, the many-body Rydberg systems have many similarities with solid-state systems and therefore can be seen as a great toolbox to study for example quantum phase transitions. These transitions are relevant for the study of the mechanisms behind high-temperature superconductors [27] and heavy-fermion materials [28].

## 1.2. Ytterbium

In the following the special aspects and prospects using Yb in ultracold Rydberg experiments are discussed. The general properties of Yb are highlighted as well as the unique possibilities Yb offers within the framework of Rydberg physics.

Yb is a lanthanoide, a rare earth element. It has the atomic number 70 and its isotopes with their abundance are shown in table 1.2. The ground state has the electron configuration $4f^{14}6s^2$. The energy term of the five stable bosonic isotopes $^{168}Yb$,$^{170}Yb$,$^{172}Yb$,$^{174}Yb$ and $^{176}Yb$ is $^1S_0$. The two stable fermionic isotopes $^{171}Yb$ and $^{173}Yb$ have nuclear spin of $I_{171} = 1/2$ and $I_{173} = 5/2$. Therefore their ground state has a hyperfine structure. The bosonic ground state is a single state with no substructure. Therefore there is no hyperfine splitting and magnetic structure. This offers a simple system for doppler-cooling and the realization of a magneto-optical trap (MOT) [29].

Yb is a rare earth metal and has two valence electrons. Its electronic structure resembles

**Table 1.2.:** Abundance of the Yb isotopes [30] and the inter isotope scattering length taken from [31].

| Isotope | Abundance | Scattering length [nm] |
|---|---|---|
| $^{168}Yb$ | 0.13% | 13.33(18) |
| $^{170}Yb$ | 3.05% | 3.38(11) |
| $^{171}Yb$ | 14.3% | -0.15(19) |
| $^{172}Yb$ | 21.9% | -31.7(34) |
| $^{173}Yb$ | 16.1% | 10.55(11) |
| $^{174}Yb$ | 31.8% | 5.55(8) |
| $^{176}Yb$ | 12.7% | -1.28(23) |

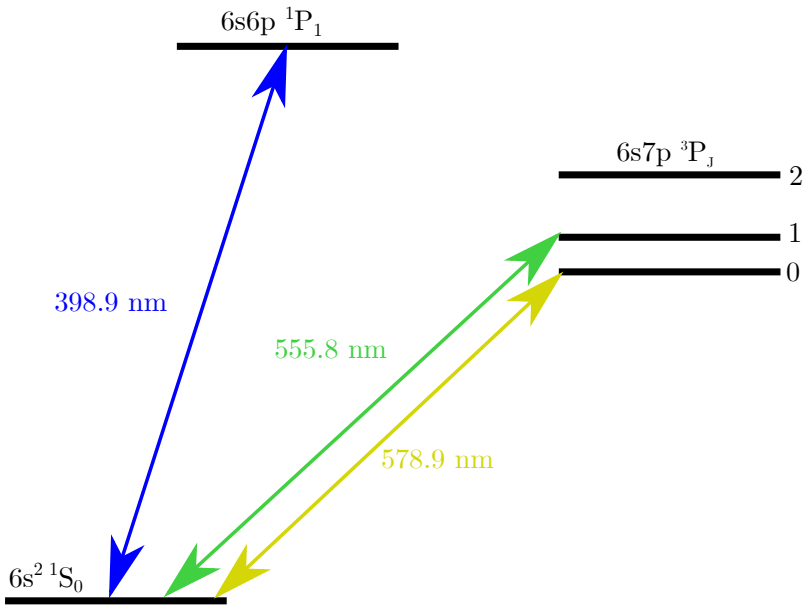


**Figure 1.2.:** *Reduced schematic energy level of Yb. The "blue" 398.9 nm singlet-singlet transition is dipole allowed and can be used for cooling and trapping of hot Yb atoms. The singlet-triplet transition ("green" 555.8 nm and "yellow" 578.9 nm) are actually forbidden, but due to higher order magnetic multipole effects [29] and the mass of Yb the are weakly allowed. They can be for example used to cool the Yb atoms in the $\mu K$ regime, which causes a condensation into a Bose-Einstein condensate [32]. The "yellow" transition can also be used for precise fundamental frequency metrology [33].*

that of alkaline earth atoms. The two valence electrons offer unique methods for the study of Rydberg physics or metrology [33].

Due to the two valence electrons, Yb has singlet and triplet electronic spin states, as can be seen in figure 1.2. According to the electric dipole transition rules the transition between those states are "forbidden", but due to higher order magnetic multipole effects

[29] and the large mass of Yb they are weakly allowed. This results in narrow linewidths, which can be used for cooling the Yb atoms optically to temperatures in the $\mu K$ regime, for example to produce Bose-Einstein condensates [32] subsequently or for fundamental frequency metrology.

There are two possibilities to use Yb as an atomic clock standard. The first one is to trap the neutral Yb atoms in an optical lattice and use the ${}^1S_0 \rightarrow {}^3P_0$, with a natural linewidth of a few 10 mHz, as the clock transition. The fermionic isotopes of Yb with their non zero nuclear spin are used for this kind of clock, because the non zero nuclear spin provides a constant non zero magnetic field, which defines the inter-combination line in a very precise way. A comparison between to systems exhibits an atomic clock instability of $1.6 \times 10^{-18}$ after 7 hours of averaging [33].

Another method is to use $Yb^+$. Here the ions are trapped in a radio-frequency Paul trap. Due to the remaining valence electron the ions can be laser cooled, for example on the ${}^2S_{1/2} \rightarrow {}^2P_{1/2}$ transition. There are several possible clock transitions in Yb+, one of these is the electric octupole (E3) ${}^2S_{1/2}(F=0) \rightarrow {}^2F_{7/2}(F=3)$. Using this transition the most advanced ion clock was build, with a relative measurement uncertainty of $1.1 \times 10^{-18}$ and a systematic uncertainty of $3.2 \times 10^{-18}$.

Another advantage of Yb is the variety of different scattering properties due to the large number of stable isotopes. As can be seen in table 1.2 the inter isotope scattering length varies from attractive to repulsive. This allows to realize quantum degenerate gases with very different properties [34]. This gives the opportunity to study many-body Rydberg systems with very different properties, as described in section 1.1.

### Rydberg dressing

In general the Rydberg dressing method can be used for introducing a novel interaction between ground state atoms [10][35]. The interaction between the ground state atoms is introduced by coupling the ground state over an intermediate state to a Rydberg state. The ground state atoms now interact with each other over the admixed Rydberg state. These interactions can lead to interesting phenomena like the formation of exotic spin and magnetic states [36][37], super solids [38], and three-dimensional solitons [39].

The property, which arises from the two valence electrons opens a variety of novel possibilities in the study of Rydberg physics. One of these possibilities results from the singlet and triplet states (see figure 1.2). As mentioned before, the transition between these states is only very weakly allowed, resulting in very narrow transitions. In the method of Rydberg dressing, these single-triplet transitions have an advantage over one electron atoms.

As described in [40] the advantage of alkaline earth atoms like Yb against alkali atoms lies in the reduction of decoherence from light scattering by coupling to triplet Rydberg state via the long-lived triplet intermediate state. This dressing scheme over the weak coupled intermediate state also enables Autler-Towns spectroscopy of strongly-driven Rydberg systems, where the Rydberg population is small. In alkali atoms this spectroscopy is much more challenging, because typically the laser coupling between the intermediate state and the ground is much stronger than between the Rydberg state and the intermediate state.

#### Ultracold Rydberg molecules

Another possible application of Yb is the study of ultra-long-range Rydberg molecules. These molecules are formed by the scattering of the excited Rydberg electron with a neighboring ground state atom. This novel binding mechanism can form giant molecules with the size of the Rydberg atom and with a permanent dipole moment, even in the case of a homo-nuclear molecule [41]. The so-called "trilobite" molecule states, which are formed with anisotropic $n$P and $n$D Rydberg states, possess very large dipole moments, up to the Kilo-Debye range [42]. However a detailed analysis of the Rydberg molecules is challenging because of the ground state hyperfine and spin-orbit interactions of the Rydberg electron. Theses interactions lead to a mixing of singlet and triplet electronic symmetries, which complicates the analysis of the molecules. Both of these interactions are absent in case of bosonic alkaline-earth atoms, which makes them an attractive system to study Rydberg molecules.

### State selective autoionisation

The two valence electrons support also doubled excited states. In those states both electrons are excited, where one of them is in a Rydberg state. For low l states, the overlap between the Rydberg wavefunction and the excited second electron is significant, which leads to autoionizing of the Rydberg atom. This phenomenon can be used to ionize state selectively the Rydberg atoms [19]. It also enables a spatial resolution of the Rydberg atoms by controlling very precisely the ionisation volume. This diagnostic is not possible with the common selective field ionisation method, unless a complex highly-magnifying charged particle optics is used. [43].

### Ultra cold neutral plasma

Collisions and Pennig ionisation in a cold gas of Rydberg atoms can rapidly transform the gas into an ultra cold neutral plasma [44]. In the case of alkali atoms, the study of the dynamics and the evolution of such exotic states of matter is limited to the detection of charged particles with no spatial resolution.
However, the second valence electron of an alkaline earth atom like Yb enables the possibility to image the ultra cold plasma *in situ*. The single ionized $Yb^+$ for example is still optically active, due to the remaining electron transition $^2S_{1/2} \rightarrow ^2 P_{1/2}$ with a wavelength of 369.5 nm. This feature of two electron atoms has already been used to study ion dynamics in ultra cold neutral plasma of Strontium [4] [45].

# 2.

# Basic experimental and theoretical concepts

In the first part, this chapter summarizes the basic principle of cooling and trapping of neutral atoms. It explains how a Zeeman slower decelerates a thermal atomic beam (section 2.1.1) of Yb atoms. It also describes how a magneto-optical trap (MOT) cools and traps the slowed Yb atoms (section 2.1.2 and 2.1.3). The explanations and formula in the corresponding sections are taken from [46].
In the second part, this chapter gives a short introduction into the basic concepts of Rydberg physics. It explains the quantum defect theory, which can be used to describe the energy levels of Rydberg states. It will further introduce the multi channel quantum defect theory, which is an essential tool to describe two-electron Rydberg atoms like Yb. This chapter will also describe how Rydberg states are affected by an external electric field. In this context, it also describes how the interaction of Rydberg atoms with each other affects the energy level of the Rydberg states.

## 2.1. Cooling and trapping of atoms

The cooling and trapping of neutral atoms with lasers is based on the scattering process between a photon and a neutral atom. Each scattering of a photon transfers momentum to the atom. The force resulting from this process depends on the momentum of the photon $\hbar\vec{k}$ and the scattering rate $\Gamma$:

$$\vec{F} = \hbar\vec{k}, \tag{2.1}$$

where $\vec{k}$ is the wave-vector of the light field. While the wavenumber $|\vec{k}| = 2\pi/\lambda$ depends on the wavelength of the photon, which scatters from the atom. The scattering rate $\Gamma$ is given by [46]

$$\Gamma = \frac{\gamma}{2} \frac{S_0}{1 + S_0 + (2\delta/\gamma)^2}, \tag{2.2}$$

where $\gamma$ is the linewidth of the atomic transition and $\delta$ is the detuning of laserlight to the transition wavelength. The saturation parameter $S_0$ is defined as $S_0 = I/I_{sat}$. While $I$ is the intensity of the light field and $I_{sat}$ the saturation intensity of the atomic transition, which is given by [46]

$$I_{sat} = \frac{\pi hc}{3\lambda^3 \tau}, \tag{2.3}$$

where $\tau$ is the lifetime of the excited state and therefore $S_0$ is specific for a given atom species and transition. The scattering rate $\Gamma$ is maximal if the detuning $\delta = 0$. Since the atom is in motion it experiences a Doppler shift of the laser light field, which changes due to the deceleration, caused by the scattering process. The Zeeman effect can be used to compensate this variation of the detuning, which is the basic principle of the Zeeman slower (see section 2.1.1).

### 2.1.1. Zeeman slower

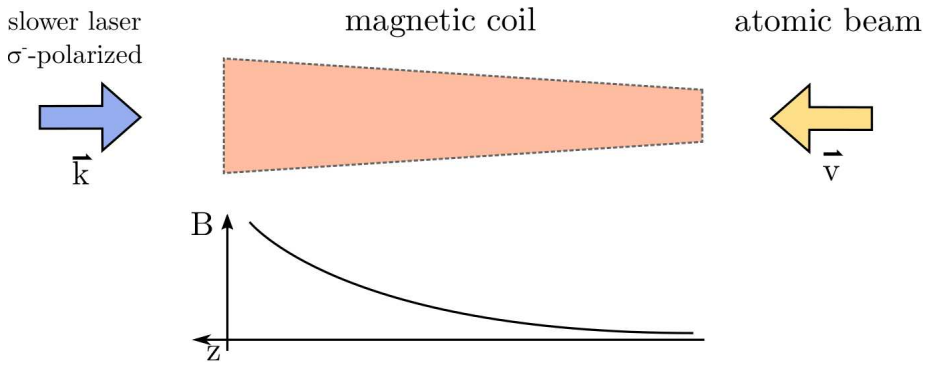


**Figure 2.1.:** *Working principle of a Zeeman slower. The atomic beam and the slower laser beam are conterpropagating. The magnetic field B generated by the slower coil compensates the Doppler shift. Adapted from [47].*

The MOT is loaded from an Yb atom beam (see section 2.1.3). This beam is generated

in an oven, the Yb atom therefore has a high thermal velocity. Before the atoms can be trapped in a MOT, they have to be slowed down. One method to slow the atoms down is the Zeeman slower, which also cools the atom beam. The structure of the slower consists of the atomic beam, a laser beam and a magnetic field. The atom beam and the laser beam are counter-propagating. The magnetic field is aligned along the direction of propagation of both beams (see figure 2.1). The detuning to the atomic transition $\delta_0$ is given by [46]

$$\delta = \delta_0 - \vec{k} \cdot \vec{v} - \frac{\mu' B}{\hbar}, \tag{2.4}$$

where $\vec{k}$ is the wavevector of the light field and $\vec{v}$ the velocity of the atoms. $B$ is the magnetic field and $\mu'$ the effective magnetic moment, which is given by [46],

$$\mu' = (g_e m_e - g_g m_g)\, \mu_B. \tag{2.5}$$

Here $ge, g$ and $m_{e,g}$ are the Landé g-factors and magnetic quantum number of the ground and excited state.

The velocity of the atoms is changing during the scattering process. This changes the effective detuning of the laser beam as can be seen in equation 2.4. The basic concept of the Zeeman slower is to compensate the change in the detuning with a spatially varying magnetic field. To derive the needed magnetic field geometry we first look at the maximal deceleration $a_{max}$. For high intensity of the light field $I >> I_{sat}$ and zero detuning the maximal deceleration is given by,

$$|a_{max}| = \frac{F_{max}}{m} = \frac{\gamma}{2}\frac{\hbar k}{m} \tag{2.6}$$

The position dependent velocity of the atom is therefore given by,

$$v(z) = \sqrt{v_0^2 - s|a_{max}|z}. \tag{2.7}$$

with the z-axis chosen as the propagation direction of the atom beam and $v_0$ is the maximal velocity of an atom that can be slowed down by the Zeeman slower. With $\delta = 0$ the required magnetic field can be derived from 2.4,

$$B\,(z) = \frac{\hbar}{\mu'}\left(\delta_0 + k\sqrt{v_0^2 - s|a_{max}|z}\right) \tag{2.8}$$

The equation 2.8 describes an increasing magnetic field along the propagation of the atom beam. The detuning of the laser beam has to be $\delta = -kv_0$ to be in resonance with the atomic transition. The laser is therefore red detuned to the atomic transition, which is advantageous compared to the opposite geometry, where magnetic field decreases along the propagation of the atom beam. With the increasing geometry the slower beam is not resonant with the cold and slowed atoms when they reach the MOT position.

### 2.1.2. Optical molasses

An optical molasses is used to cool atoms in three dimensions, it is formed by six pairwise counterpropagating laser beams. These beams exert a force on the atoms, which is proportional to the velocity of the atoms. For one dimension the force is given by [46],

$$\vec{F}_{\pm} = \pm\hbar\vec{k}\frac{\gamma}{2}\frac{S_0}{1+S_0+\left(\frac{2(\delta\mp kv}{\gamma}\right)^2} \tag{2.9}$$

The total force in one dimension that is exerted on the atom, is given by the sum of both laser beams,

$$\vec{F}_{OM} \quad = \quad \vec{F}_{+} + \vec{F}_{-} = -\beta\vec{v}, \tag{2.10}$$

where $\beta$ acts as a damping constant, if the laser beams are red detuned ($\delta < 0$). This force damps the atomic motion, with

$$\beta = \frac{8\hbar k^2 \delta S_0}{\gamma\left(1+S_0+\left(\frac{2\delta}{\gamma}\right)^2\right)^2}\,. \tag{2.11}$$

Since the force of the optical molasses is not position dependent, it can only be used to cool the atoms, not to trap them. A position dependency can be introduced with a magnetic field, which combined with a optical molasses, forms a magneto-optical trap (MOT) (see section 2.1.3). With the optical molasses the atom can be cooled to the Doppler cooling limit, which is given by [46],

$$T_D = \frac{\hbar\gamma}{2k_B}. \tag{2.12}$$

The limit arises from the momentum transfer caused by the absorption and emission of photons. The limit depends on the atom species and the transition used for the molasses. The Doppler limit is typically in the order of 100 $\mu$K.

### 2.1.3. Magneto-optical trap

The MOT is formed by adding a quadrupole magnetic field to the laser field. This field introduces a spatial dependent force to the atoms. The atoms can therefore be trapped in the center of the magnetic field. The principle of the Yb MOT is illustrated in figure 2.2. For the sake of simplicity, the following descriptions of the principle is only explained for one dimension. The "blue" Yb MOT, which is used in the experiment, uses the $6s^2\ ^1S_0(J=0) \rightarrow 6s6p\ ^1P_1(J=1)$ transition, for cooling and trapping the atoms. A spatially varying magnetic field $B(z) = B_0 z$ splits the upper $6s6p\ ^1P_1$ state into its three Zeeman sub-components, with the quantum numbers $m_J = -1, 0, 1$. Since the laser beams are circularly polarized and red detuned to the atomic transition (dashed line in figure 2.2) they are only in resonance with the atomic transition, on one side of the MOT. This means that more light is scattered from the $\sigma_-$ polarized beam on the $z > 0$ side of the MOT than from the $\sigma_+$ polarized beam and vice versa. This distinction in direction causes the atoms to experience a force that drives them towards the center of the magnetic field. The total force, which acts on the atoms, is given by [46]

$$\vec{F}_{MOT} = \frac{8\hbar k^2 \delta S_0 \vec{v}}{\gamma\left(1 + S_0 + \left(\frac{2\delta}{\gamma}\right)^2\right)^2} + \frac{\mu' B_0}{\hbar} \frac{8\hbar k^2 \delta S_0 \vec{r}}{\gamma\left(1 + S_0 + \left(\frac{2\delta}{\gamma}\right)^2\right)^2} = -\beta\vec{v} - \kappa\vec{r} \qquad (2.13)$$

Sine the force depends on the position and velocity of the atoms, it forms a trap which cools and traps neutral atoms. With this kind of trap it is possible to capture atoms with a maximal velocity $v_c = \sqrt{2 r_c \hbar k \gamma / m}$, where $r_c$ is the radius of the trap. The capture volume depends on the size of the atom beam, the intensity and the magnetic field gradient. The trapping radius is a critical parameter for the release-recapture method [48], which is also used in this Thesis (see section 3.4.3).

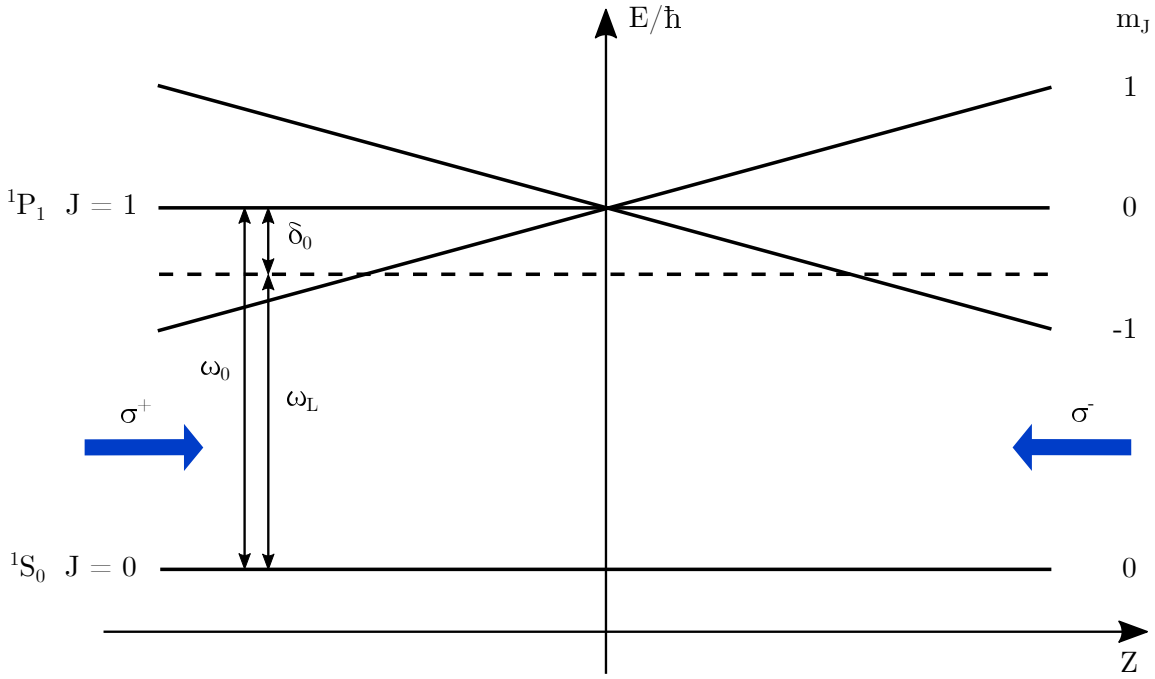


**Figure 2.2.:** *Basic principal of a magneto-optical trap for Yb in one dimension. The two counterpropagating laser beams are red detuned to the* $6s^2\,{}^1S_0(J=0) \rightarrow 6s6p\,{}^1P_1(J=1)$ *transition (dashed line) and* $\sigma_+/\sigma_-$ *polarised. The magnetic field* $B(z) = B_0 z$ *splits the* $6s6p\,{}^1P_1(J=1)$ *into its Zeeman substructure. The figure is adapted from [47].*

## 2.2. Energy levels of Rydberg atoms

For the analysis of the Rydberg state spectroscopy, which is a key result of this thesis, it is useful to determine the quantum defect of each state. The following sections will give a brief introduction into the quantum defect theory (QDT) and multi channel quantum defect theory (MQDT). The explanations and formulas in the context of the QDT are summarized from [1]. The references [49], [50] and [7] are the background for the description of the MQDT.

### 2.2.1. Quantum defect theory

To describe the energy levels of a Rydberg atom we start at the most simple case, namely the hydrogen atom. There, the energy levels are given by the Rydberg series [1]. For hydrogen-like Rydberg atoms the energy levels are given by [1]:

$$E_{n,l} = E_{ion} - \frac{R_y}{n_l^*} \tag{2.14}$$

where $E_{ion}$ is the Ionisation energy of the specific atom, $R_y = hcR_\infty$ with the Rydberg constant$R_\infty = 1.0973731568160(21) \times 10^7\,1/\mathrm{m}$ and $n_l^*$ is the effective quantum number. The difference between hydrogen and other elements is the effective quantum number $n_l^*$. So the question is: How does $n_l^*$ differ from hydrogen? To determine this difference we have to look at the wave function of the Rydberg atoms. For this purpose, we start to solve the time dependent Schrödinger equation [1]in atomic units for hydrogen

$$\left(-\frac{\Delta^2}{2} - \frac{1}{r}\right)\Psi = E\,\Psi, \tag{2.15}$$

where $E$ is the energy of the electron, $r$ is the distance between electron and proton. Since the atom has a spherical symmetry we can use spherical coordinates. If we assume that the wave function is separable in a radial and a spherical component like,

$$\Psi = Y(\Theta,\phi)\;R(r), \tag{2.16}$$

the solution for the spherical part is,

$$Y_{l,m}(\Theta,\phi) = \sqrt{\frac{(l-m)!2l+1}{(l+m)!4\pi}}P_l^m(\cos\Theta)\,e^{im\phi}, \tag{2.17}$$

where $P_l^m(x)$ is the unnormalized Legendre polynomial. The radial problem is given by

$$\frac{\partial^2 R}{\partial r^2} + \frac{2}{r}\frac{\partial R}{\partial r} + \left[2\epsilon + \frac{2}{r} - \frac{l(l+1)}{r^2}\right]R = 0. \tag{2.18}$$

and according to [1] the problem can be converted to the standard form of the coulomb problem by introducing $\rho(r)$. With the substitution $R(r) = \rho(r)/r$ the equation can be simplified to:

$$\frac{\partial^2 \rho}{\partial r^2} + \left[2\epsilon + \frac{2}{r} - \frac{l(l+1)}{r^2}\right]\rho = 0. \tag{2.19}$$

Here $\epsilon$ is the energy of the state relative to the ionisation threshold. The potential, we have to consider, has two components. The $1/r$ term is the Coulomb potential and $l(l+1)/2r^2$ is the centrifugal potential of the electron. This differential equation gives the familiar term for the allowed energies 2.14. A detailed derivation can be found in [1].

To extend this model to a single valence electron atoms with spherical ionic cores, we

have to modify the potential. The difference between a hydrogen atom and alkali atom is the core of the atom, which includes the nucleus and all electrons in closed shells. The core of a non-hydrogen atom has a finite sized ionic core with radius $r_{Yb^+} \approx 128\,\text{pm}$, which is several magnitudes larger than the hydrogen core $r_H = 0.84\,\text{fm}$. From a large distance the ionic core can be treated as point-like and singly charged for the valence electron, because the inner electrons shield the nucleus. However at smaller distance, the valance electron penetrates the electron cloud an thus the charge of the nucleus is not shielded completely. This leads to significant modification of the inner part of the potential.

This new potential $V_{\text{eff}}$ is deeper than the Coulomb potential, because of the lesser shielding.

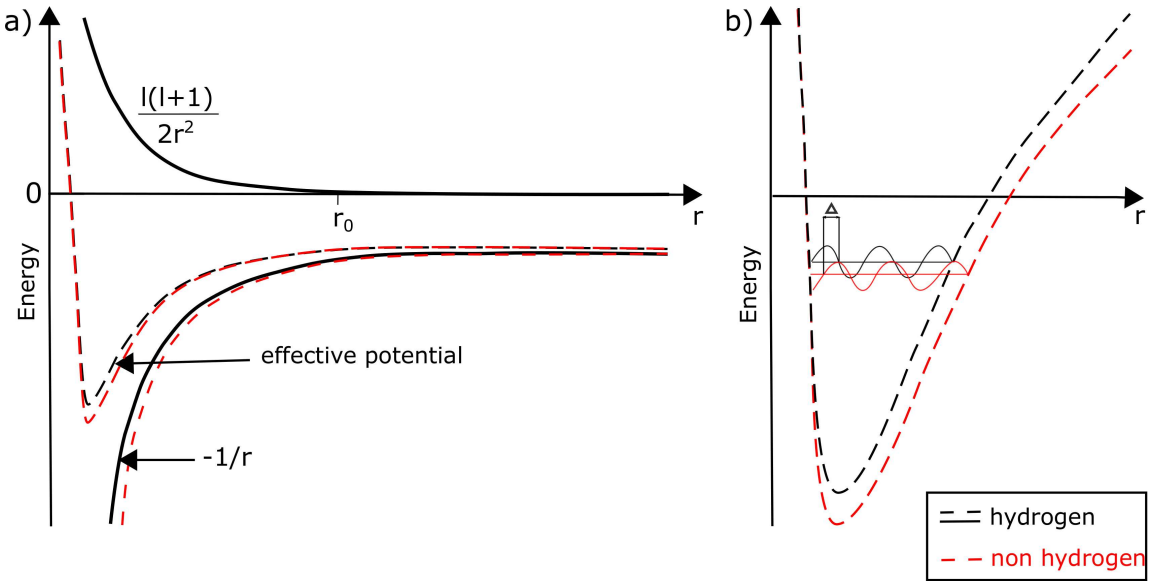


**Figure 2.3.:** *Schematic sketch of the atomic potential for hydrogen (black) and non hydrogen (red) atoms, with angular momentum $l$. a) The black solid lines are the centrifugal (upper) and the Coulomb (lower) potential. The black dashed line is the resulting potential for a hydrogen atom. The lower red dashed line is the modified Coulomb potential for non hydrogen atoms. The upper red dashed line is the resulting potential for non hydrogen atom. $r_0$ is taken as the size of the ionic core. b) Zoomed view of the potential. The black solid line shows the energy level and wave function of an electron in the potential of a hydrogen atom. The red solid line represents the non-hydrogen case. The energy level is shifted downwards and has a phase shift $\Delta$ compared to the hydrogen case.*

If we assume that the core is spherical symmetric, the effective potential $V_{\text{eff}}$ is still separable. Therefore the angular wave function (equation 2.17) is unchanged.

Figure 2.3 shows in a schematic way how the Coulomb potential alters in case of a finite

sized ionic core. Above $r_0$, the size of the ionic core, the potential is approximated by to the Coulumb potential. For $r < r_0$ the potential is deeper, which leads to an increase in the kinetic energy of the electron and a decrease of the wavelength of the radial oscillation relative to hydrogen. In the case of $r > r_0$ the difference between an alkali and hydrogen is a phase shift $\Delta$ in the wave function. The magnitude of the radial phase shift is given by the difference in momentum of an electron with an energy $E$ integrated from $r = 0$ to $r_0$, in a non hydrogen atom potential and in a hydrogen atom potential. Therefore the magnitude of the radial phase shift for an s electron relative to hydrogen is given by [1],

$$\Delta = \int_0^{r_0} \left[ [E - V_{non-H}(r))^{1/2} - \left( E + \frac{1}{r} \right)^{1/2} \right] \tag{2.20}$$

Considering this shift, it is possible to solve the Schrödigner equation for the alkali atoms in the region $r > r_0$ and get the following expression for the energy levels [1]

$$E_{n,l} = E_{ion} - \frac{R}{(n - \delta_{l,n})^2} \ , \tag{2.21}$$

where $\delta_{l,n}$ is the so-called quantum defect, which depends on the principle quantum number $n$ and the orbital angular momentum quantum number $l$. Concerning the binding energy, the complete difference to a hydrogen atom can be expressed by this defect.

### Rydberg-Ritz formula

The quantum defect $\delta_{n,l}$ varies slowly within a specific $nl$ series. To describe this variation it is common to use the Rydberg-Ritz formula ([7],[51] and [52]), which is a Taylor expansion of the quantum defect. The formula reads:

$$\delta_{n,l} = \delta_0(l) + \frac{\delta_1(l)}{n - \delta_0(l)^2} + \frac{\delta_2(l)}{n - \delta_0(l)^4} + ... \ , \tag{2.22}$$

where $\delta_0(l)$ is the quantum defect at the ionization limit and the other terms are defined by the energy dependency of the quantum defect. With large $n$ the quantum defect reaches the limit $\delta_0(l)$ (ionisation limit) and becomes independent of $n$.

### 2.2.2. Multichannel quantum defect theory

In case of Yb, which has two valence electrons, the assumption that the core is spherical symmetric is not necessarily valid. The presence of a second electron induces perturbations in the energy levels of the Rydberg electron. One possibility to model this problem is to use the multi channel quantum theory (MQDT)[49]. The MQDT describes the interaction of a single active electron with the core through an effective core-dependent potential. The following description of the MQDT is summarized from the reference [50]. In the context of the MQDT the different channels are associated to different configurations of the active electron and the core. The wave function of the total system is a linear combination of the wave functions of each channel. An extensive MQDT study of Yb can be found in [7]. In the following the main ingredients of the MQDT are briefly summarized.

To model the interaction of the core with the perturbations we start with the radial Schrödinger equation 2.19. For each channel the active electron has to satisfy the equation. So we can write down the radial Schrödinger equation for each channel as:

$$\frac{\partial^2 \rho_i}{\partial r^2} + \left[2\mu\epsilon_i + \frac{2\mu}{r} - \frac{l_i(l_i+1)}{r^2}\right]\rho_i \quad = \quad 0. \tag{2.23}$$

Here $i$ is the index for the channel and $\epsilon_i$ the energy of the electron in that specific channel. It is customary to use the wavenumber as the unit for the energy of the states and it is common to express the energy relative to the ground state not to the ionisation limit. Thus

$$\epsilon_i \quad = \quad (E - I_i)\, hc, \tag{2.24}$$

where $c$ is the speed of light and $h$ is Planck's constant. $I_i$ is the ionisation energy of the channel $i$. Since equation 2.23 is a second order equation, the solution can be expressed by a linear superposition of two independent solutions $f(l_i, \epsilon_i, r)$ and $g(l_i, \epsilon_i, r)$. These solutions are commonly termed as the regular and irregular Coulomb functions [53]. In [54] it is described how to calculate these functions numerically by using standard algorithms. We thus rewrite an approach for the solution for 2.23 as,

$$\rho_i \quad = \quad f(l_i, \epsilon_i, r)\cos\theta_i + g(l_i, \epsilon_i, r)\sin\theta_i, \qquad r >> a_0. \tag{2.25}$$

The superposition of the Coulomb functions is weighted by an angle $\theta_i$. This angle can be expressed by the effective quantum number

$$\theta_i = \pi n_i^* \tag{2.26}$$

with

$$n_i^* = n - \delta_i, \tag{2.27}$$

where $\delta_i$ is the n and l dependent quantum defect, described in section 2.2.1.
Considering the different channel wave functions, the eigenfunctions of the atomic Hamiltonian become a superposition of these wave functions where the eigenfunction $\Psi$ of a specific state has the form,

$$\Psi = \mathcal{A} \sum_i A_i \, \rho_i \, \chi_i. \tag{2.28}$$

In comparison to equation 2.16, $\chi_i$ describes not just the angular and spin dependence of the active electron, it also describes the radial, angular and spin dependence of all other electrons. The symbol $\mathcal{A}$ indicates, that the sum over all channels i is antisymmetrized. The coefficients $A_i$ are the n and l dependent weight coefficient, that define the mixture of the channel functions in the eigenstate $\Psi$.
In principle it is possible to diagonalize these short range interactions and get a set of N linearly independent uncoupled wave functions $\psi_a$ $(\alpha = 1, ..., N)$. By a unitary transformation one can relate these wave functions to the channel wave functions $\rho_i \, \chi_i$. Considering this for large r

$$\begin{aligned} \psi_\alpha &= \left( \mathcal{A} \sum_i U_{i\alpha} f\left(l_i, \epsilon_i, r\right) \, \chi_i \right) \cos\left(\pi \mu_\alpha\right) \\ &- \left( \mathcal{A} \sum_i U_{i\alpha} g\left(l_i, \epsilon_i, r\right) \, \chi_i \right) \sin\left(\pi \mu_\alpha\right), \end{aligned} \tag{2.29}$$

where $U_{i\alpha}$ are the coefficients of the unitary matrix and $\mu_\alpha$ is called eigenquantum defects [55]. This defect depends linearly on the energy level, so it can be described by

$$\mu_\alpha = \mu_\alpha^0 + \epsilon \mu_\alpha^1 \tag{2.30}$$

with

$$\epsilon \;=\; \frac{1}{(n_i^*)^2} \tag{2.31}$$

Now it is possible to express the wave function $\Psi$ in the basis set of the equation 2.28 and 2.29,

$$\mathcal{A}\sum_i A_i\,\rho_i\,\chi_i \;=\; \sum_\alpha B_\alpha\,\psi_\alpha. \tag{2.32}$$

Solving the coefficients of the equations $f\,(l_i,\epsilon_i,r)$ and $g\,(l_i,\epsilon_i,r)$ separately and considering the limit $r\to\infty$ in equation 2.32, gives the following relation:

$$A_i\,e^{-i\pi n_i^*} \;=\; \sum_\alpha U_{i\alpha}\,B_\alpha\,e^{i\pi\mu_\alpha} \tag{2.33}$$

$$B_\alpha\,e^{-i\pi\mu_\alpha} \;=\; \sum_i U_{i\alpha}\,A_i\,e^{-i\pi n_i^*} \tag{2.34}$$

The fact that the wavefunctions $\psi_\alpha$ and $\rho_i$ are real requires that the coefficients of $A_i$ and $B_\alpha$ are real. This leads to a set of equations,

$$\sum_\alpha U_{i\alpha}\,A_i\sin\left[\pi\,(n_i^*+\mu_\alpha)\right] \;=\; 0 \qquad \alpha \;=\; 1,...,N. \tag{2.35}$$

Therefore

$$\det\left|\,U_{i\alpha}\,A_i\sin\left[\pi\,(n_i^*+\mu_\alpha)\right]\,\right| \;=\; 0. \tag{2.36}$$

This equation is a constraint for the effective principle quantum number $n_i^*$, by a given unitary matrix $U_{i\alpha}$ and an eigenquantum defect $\mu_\alpha$. Considering also the boundary condition, that $\Psi\to 0$ as $r\to\infty$ leads to the familiar equation,

$$E \;=\; I_i - \frac{\tilde{R}}{n_i^{*2}}, \quad \text{with} \quad i \;=\; 1,...,N\,, \tag{2.37}$$

where $I_i$ is the ionisation limit of channel $i$ and $\tilde{R}$ is the finite mass corrected Rydberg constant. For Yb the corrected Rydberg constant is given by,

$$\tilde{R}_{Yb} = R_\infty\cdot\frac{m_{Yb}}{m_{Yb}+m_e}\,. \tag{2.38}$$

Here $R_\infty$ is the Rydberg constant, $m_{Yb}$ the Yb atom mass and $m_e$ the electron mass. With the unitary matrix $U_{i\alpha}$ and the eigenquantum defect $\mu_\alpha$, we have a full set of parameters, which characterizes a series of Rydberg states. These parameters can be calculated *ab initio* [56] or can be derived by fitting to experimental data [7], [50].
It is common to describe the $\alpha$ channels in a $LS$ coupling scheme, where the eigenchannels $\bar{\alpha}$ are introduced with a pure $LS$ coupling $n_0 l_0 j_0\, nljJ$ with a analytically known unitary matrix $U_{i\bar{\alpha}}$. The unitary matrix $U_{i\alpha}$ can be factorized as a product of rotation matrices

$$U_{i\alpha} = U_{i\alpha}\, V_{\bar{\alpha}\alpha}\,, \tag{2.39}$$

where the rotation matrix $V_{\bar{\alpha}\alpha}$ can be written in terms of $2 \times 2$ rotation matrices $R_{\alpha\bar{\alpha}}\,(\theta_{\alpha\bar{\alpha}})$ with the rotation angle $\theta_{\alpha\bar{\alpha}}$. The angles are defined by the coupling of the different channels. The eigenquantum defect $\mu_\alpha$ of each channel and their rotation $\theta_{\alpha\bar{\alpha}}$ are the free parameters, which characterize the weight of the channel to the unitary matrix. Due to the non commutative product of rotation matrices product, the order of the rotation is also a parameter for the transformation matrix.

### Bound state energies

The principle aim of the MQDT is to predict energy levels of bound states. For this purpose the free parameters $\mu_\alpha$ and $\theta_{\alpha\bar{\alpha}}$ are fitted to experimental data of a Rydberg series. The energies $E$ of a series are given by equation 2.37. The eigenquantum defect used to calculate the energies has to satisfy the equation 2.36. To find these energies one has to select two channels $i$ and $k$, which are expected to dominate the series. The next step is to guess the effective principle quantum number $n_j^*$, by using the experimental data and equation 2.37. With $n_j^*$ and the equation 2.37 it is possible to derive the corresponding values $n_j^*$, by introducing the function

$$F_i\left(n_j^*\right) \;=\; \left[\frac{I_i - I_J}{\tilde{R}} + \frac{1}{(n_j^*)^2}\right]^{-1/2}. \tag{2.40}$$

By setting

$$n_j^* \;=\; F_i(n_j^*) \qquad \text{with} \qquad i \neq j, \tag{2.41}$$

it is possible to determine the corresponding principle quantum numbers $n_j^*$, apart from $n_k^*$. With these quantum numbers and equation 2.36, we define an implicit function, which determines the value of $n_k^*$ for a given unitary matrix $U_{i\alpha}$. To find the principle quantum numbers where both equations 2.36 and 2.37 are fulfilled it is convenient to define a function $G_k\left([U_{i\alpha}]\,;n_j^*\right)$ such that 2.36 is fulfilled when,

$$n_k^* \;=\; G_k\left([U_{i\alpha}]\,;n_j^*\right) \tag{2.42}$$

with the condition defined in equation 2.41. To obtain the values of $n_j^*$ of the corresponding bound states energies, we seek for the roots of the function

$$\Xi\left(n_j^*\right) \;=\; G_k\left([U_{i\alpha}]\,;n_j^*\right) - F_i(n_j^*) \tag{2.43}$$

The resulting energy levels given by equation 2.37, are the energy bound states defined by the MQDT model.

## 2.3. Rydberg atoms and electric fields

Due to their properties Rydberg atoms are very sensitive to external electric fields. In this section, the Stark effect is described. There the response of the Rydberg states to electric fields is described by its polarizability. In this context the state dependence of the polarizability is discussed in the second-order perturbation theory. Furthermore the pair-state interaction between two Rydberg atoms is briefly introduced to estimate possible interactions in our experiments.

### 2.3.1. Stark effect

The stark effect describes the interaction of an atom or molecule with an external electric field. In general one has to distinguish between a DC Stark effect for static external electric fields and an AC Stark effect for oscillating external electric fields (typically light fields). In the following we investigate the behavior of the Rydberg atoms in a static electric field, so we look closer at the DC stark effect.

The interaction between an atom or molecule and a static external electric field is given

by,

$$\Delta E = -F \cdot d_{el} \,, \tag{2.44}$$

where $F$ is the electric field and $d_{el}$ is the electric dipole moment of the atom or molecule . If the states of the atom are degenerate with respect to their orbital momentum $l$, like in hydrogen, they are hybrid orbitals. These orbitals have a permanent dipole moment $d_{el}$. This leads to a linear shift of the state energies with the electric field (see figure 2.4 a)). Due to the specific form of these orbitals some of these states shift to lower energies (red shift), others shift to higher energies (blue shift).

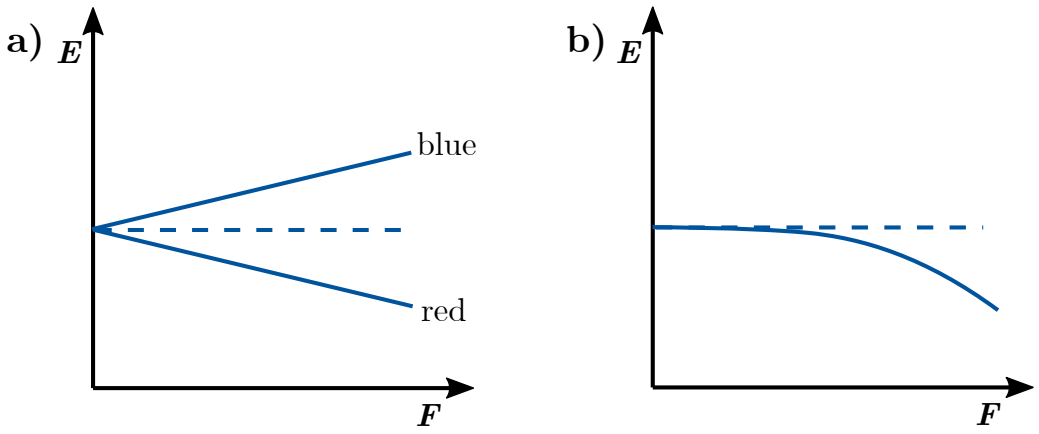


**Figure 2.4.:** *a) linear stark shift of hydrogen state b) quadratic shift of non hydrogen atom in an external electric field.*

In non-hydrogen atoms like Yb the states are non-degenerate with respect to the orbital momentum $l$, so these states have no intrinsic dipole moment. In this case the dipole is induced by the external electric field,

$$d_{el} = \frac{1}{2}\alpha_0 \cdot F \tag{2.45}$$

Here $\alpha_0$ is the polarizability of the state. Therefore the Stark shift of the energy of the state is quadratic (see figure 2.4 b)) and is given by,

$$\Delta E = -\frac{1}{2}\alpha_0 \cdot F^2 \tag{2.46}$$

A quantum mechanical description using the electric dipole approximation offers insight to the state dependence of the polarizability. Within this approximation, the interaction Hamiltonian $H' = -\hat{d} \cdot F$, with $\hat{d}$ as the dipole operator, describes the perturbation caused by the electric field. Where the dipole operator is given by $\hat{d} = e \times r$. In second order perturbation theory, we obtain for the Stark shift [57]

$$\Delta E = \frac{1}{3(2J+1)} \sum_{n'l'm'} \frac{\langle \psi_{nlm} | \hat{d} | \psi_{n'l'm'} \rangle \langle \psi_{n'l'm'} | d | \psi_{nlm} | \rangle}{E_{nl} - E_{n'l'}} \cdot F^2 \tag{2.47}$$

Here $\psi_{nlm}$ is the wavefunction of the electron, with the total angular momentum $J$ and the energy level $E_{nl}$. With this expression and eq. 2.46, it is possible to identify the following expression for the polarizability,

$$\alpha_0(n,l,j) = \frac{2}{3(2J+1)} \sum_{n'l'm'} \frac{\left| \langle \psi_{n'l'm'} | \hat{d} | \psi_{nlm} \rangle \right|^2}{E_{n'l'} - E_{nl}} \tag{2.48}$$

We now assume, that for the scaling behavior of the polarizability the main contribution comes from a single state. This state must be dipole allowed and is the closest in energy (i.e. $l' = l \pm 1$). Because the matrix element $\langle \psi_{n'l'm'} | d | \psi_{nlm} \rangle$ is proportional to length, it has the same scaling as the expectation value for the orbital radius,

$$\langle r \rangle \sim n^2 \,. \tag{2.49}$$

The scaling behavior of the energy difference can be calculated as,

$$\begin{aligned} \lim_{n\to\infty} E_{n,l+1} - E_{nl} &\propto \lim_{n\to\infty} \frac{1}{2n^2} - \frac{1}{2\,(n+\epsilon)^2} \\ &\propto \lim_{n\to\infty} \frac{1}{2} \cdot \frac{2n\epsilon + \epsilon^2}{n^2\,(n-\epsilon)^2} = \epsilon\, n^{-3}. \end{aligned} \tag{2.50}$$

Where $\epsilon$ represents the energy difference between the $l$ and $l+1$ states. These two scalings (equation 2.49 and 2.50) combined lead to an asymptotic behavior for the scalar polarizability,

$$\alpha_0 \sim n^7 \,. \tag{2.51}$$

This scaling with the principal quantum number makes Rydberg atoms with high principal

quantum number very sensitive to external electric fields, which allows for a wide range of possible application, i.e. radio-frequency electric field sensors [58] or the dipole blockade mechanism, which is an essential ingredient for using Rydberg atoms as qbits in quantum information [14].

## 2.4. Pair-state interaction

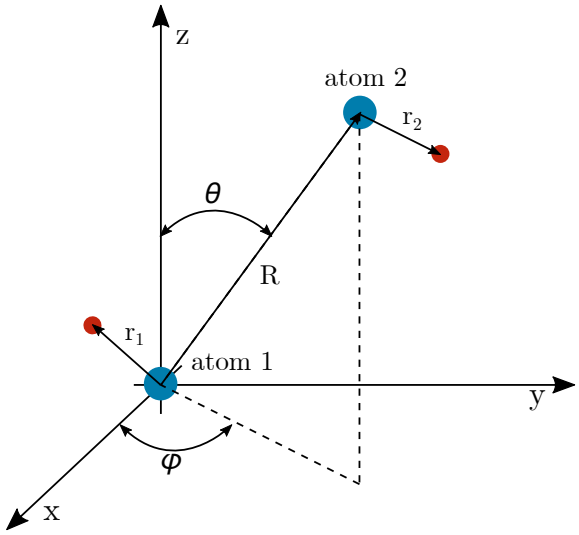


**Figure 2.5.:** *Coordinate system for the pair-state interaction. The polar angle $\theta = 0...\pi$ and the azimuthal angle $\phi = 0...2\pi$ defines the relative orientation to the z-axis, which is specified by the laser driving the Rydberg excitation.*

Rydberg atoms interact over a long range, because of their extremely large dipole moments. This kind of interaction behavior can be used for controlled quantum information processing [2] and for studying effects like for e.g. the superradiance [59]. For this thesis it is important to know at which inter-atomic distance the Rydberg-Rydberg interactions are so strong that they disturb the Rydberg excitation itself (Rydberg blockade). This section gives an estimation at which inter-atomic distance the pair-interaction has to be considered.

To estimate the interaction between two Rydberg atoms we first choose the coordinate system like shown in figure 2.5. The inter-atomic distance is given by $R$ and the relative orientation to the z-axis is given a the polar angle $\theta = 0...\pi$ and the azimuthal angle $\phi = 0...2\pi$. The orientation of the z-axis (quantisation axis) is specified by the polarisation

of the laser that drives the Rydberg excitation. The coordinates $r_1$ and $r_2$ are relative to the respective nuclei.

The pair-wise interaction between two Rydberg atoms can be expressed in multipole form as [60],

$$V(R) = \sum_{L_1,L_2=1}^{\infty} \frac{V_{L_1,L_2}(r_1,r_2)}{R^{L_1+L_2+1}}, \tag{2.52}$$

with $L_1+L_2 = 2$ for dipole-dipole interactions, $L_1+L_2 = 3$ for dipole-quadrupole interactions and $L_1 + L_2 = 4$ for quadrupole-quadrupole interactions. $V_{L_1,L_2}(r_1,r_2)$ is given by

$$\begin{aligned} V_{L_1,L_2}(r_1,r_2) &= \frac{(-1)^{L_2}4\pi}{\sqrt{(2(L_1+1)(2L_2+1)}} \\ &\times \sum_m \sqrt{\binom{L_1+L_2}{L_1+m}\binom{L_1+L_2}{L_2+m}} r_1^{L_1} r_2^{L_2} \\ &\times Y_{L1,m}(\hat{r}_1) Y_{L2,-m}(\hat{r}_2), \end{aligned} \tag{2.53}$$

where $\binom{n}{k}$ is the binomial coefficient and $Y_{L,m}(\hat{r})$ spherical harmonics. The energy level of the pair state can be calculated by diagonalising the matrix elements $\langle j_1 m_{j1}|V_{L_1,L_2}|j_2 m_{j2}\rangle$. If the quantisation axis is aligned along the internuclear axis $R$ the matrix elements $\langle j_1 m_{j1}|V_{L_1,L_2}|j_2 m_{j2}\rangle$ are easily evaluated. If the orientation of the quantisation axis differs from the internuclear axis, the orientation can be described by the polar angle $\theta$ and the azimuthal angle $\phi$ (see figure 2.5). For the calculation of the coupling, the atom states $|j, m_j\rangle$ have to be rotated with WignerD matrices $w_D(\theta,\phi)$.

The description of the pair interaction with the multipole approach is only valid if the wavefunctions of both atoms do not overlap. This is the case if the distance is larger than the Le Roy radius [61],

$$R_{LR} = 2\left(\langle r_1^2\rangle^{1/2} + \langle r_2^2\rangle^{1/2}\right). \tag{2.54}$$

The Ley Radius for $nS$ states is approximately $0.1\,\mu$m for $n \approx 20$ and reaches $1\,\mu$m for $n \approx 60$.

Consider now a pair of two atoms in the Rydberg pair-state $|r, r\rangle$, which are dipole coupled

to the states $|r'\rangle$ and $|r''\rangle$. The energy difference between the dipole coupled states is given by

$$\Delta = E_{r'} + E_{r''} - 2E_r. \tag{2.55}$$

Here $E_r$ is the energy of the initial state and $E_{r',r''}$ are the energies of the dipole coupled states. The Hamiltonian in the pair-state basis $\{|rr\rangle, |r'r''\rangle\}$ is therefore given by

$$\mathcal{H} = \begin{pmatrix} 0 & V(R) \\ V(R) & \Delta \end{pmatrix}. \tag{2.56}$$

For large distance ($V(R) << \Delta$) it is possible to calculate the interaction between two Rydberg atoms with the perturbation theory. The nature of the interaction, attractive or repulsive, is determined by the sign of $\Delta$. The interaction is proportional to the dispersion coefficient $C_6 \propto n^{11}$.

For a small inter-atomic distance ($V(R) >> \Delta$) the pair-state with the smallest absolute energy difference $|\Delta|$ has the biggest contribution to the atom-atom interaction. For real systems it is necessary to consider the effects of all near resonant pair-states. To calculate the interaction it is necessary to diagonalise the pair state interaction Hamiltonian to consider all states in the vicinity of the pair state. In figure 2.6 the resulting energy levels of the pair state of two rubidium atoms in the $80S_{1/2}$ state are shown. For the calculations all pair states in the range of $n = 80 \pm 5$ and $l = 0...4$ were taken into account. The calculation shows that a significant shift of the energy level starts at inter-atomic distance of approximately $5\,\mu$m. Above this distance there are no interactions which could lead to e.g. a dipole blockade [20].

Rubidium was chosen for the calculation because it has only one valence electron and the energy levels of this system are well known. The calculation of the pair-interaction energy in rubidium are therefore reliable. Due to the similar hydrogen like structure of all Rydberg atoms, the result in rubidium can be used to estimate the order of magnitude of the inter-atomic distance at which the interaction between Yb Rydberg atoms becomes important.

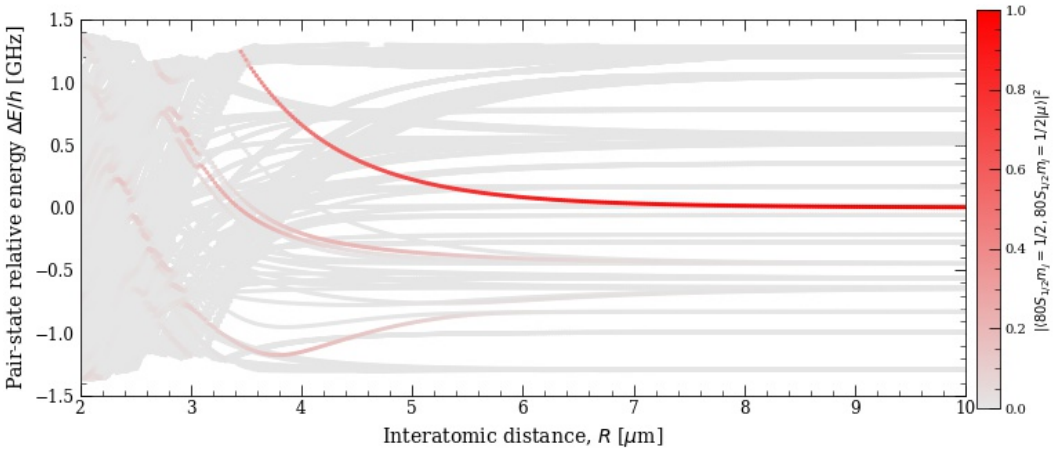


**Figure 2.6.:** *Simulated pair interaction between two $80S_{1/2}$ Rydberg states in Rubidium. The relative energy shift is determined by diagonalizing the pair-state interaction Hamiltonian. For the pair-state Hamiltonian all pair states in the range of $n = 80 \pm 5$ and $l = 0...4$ are taken into account. The simulation and figure is done with [62].*

# 3.

# Experimental apparatus

This chapter describes the experimental apparatus that was used for the experiments performed within this thesis. The apparatus is based on a setup, initially developed in the thesis of Bastian Schepers [63]. The core of the apparatus consists of a vacuum chamber with attached coils and electrodes for the required magnetic and electric fields (see section 3.1). A detailed discussion of the electric field, that is generated by the electrode setup can be found in section 3.2. Subsequently, section 3.3 describes basic measurement techniques like the data acquisition system and the ion detection system. In section 3.4 the properties of the cold Yb gas captured in the MOT are described. Section 3.5 describes the laser systems of the apparatus, which serve two purposes. The first one is cooling and trapping of Yb atoms and the second one is the excitation into Rydberg states.

## 3.1. Overview

The experiments that are presented in this thesis are all performed in an ultra-high vacuum chamber, with a pressure of approximately $10^{-10}$ mbar. In the course of this thesis significant additions were made to the apparatus. The setup of the experiment can be separated into two stages. In the first stage we performed a spectroscopic study with the MOT depletion spectroscopy (see chapter 4) and the measurement of the polarizability of the states (see chapter 5), using a simple electrode configuration. In the second stage we installed a multi channel plate (MCP) and a sophisticated electrode setup for the ionisation measurement technique (see chapter 6). The difference between those two stages only concerns the experimental chamber. The remaining part of the apparatus had the same setup in both

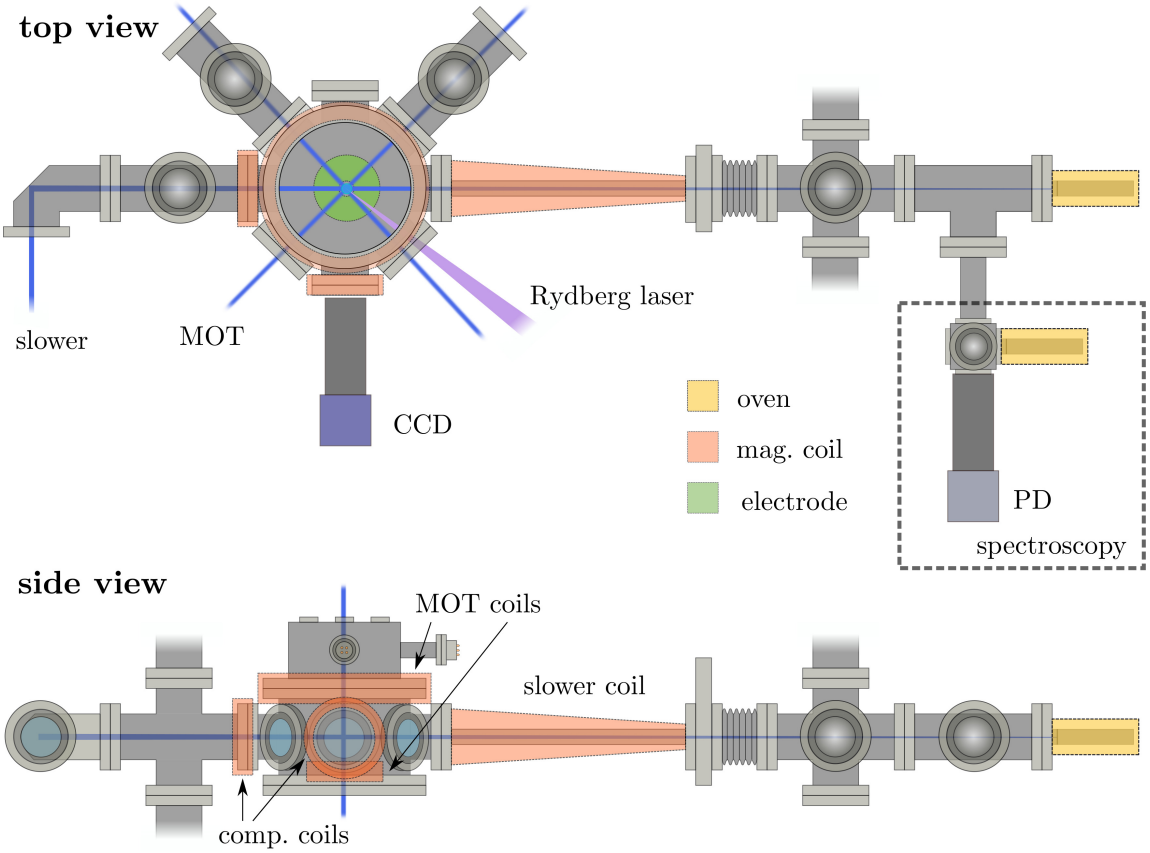


**Figure 3.1.:** *Overview of the Yb Rydberg apparatus. In the top view the cap of the experiment camber is cut off. All grey components show cross sections. For the sake of simplicity ion pumps, titan sublimation pumps and other standard vacuum devices are not shown in this sketch.*

stages and is described below. The overall setup is shown in figure 3.1. This overview shows the second stage (current status) of the apparatus. The main chamber with nine windows gives access to the six MOT beams, the slower beam, the Rydberg laser beam and a CCD Camera for imaging of the atoms.

The experimental chamber is connected to a Zeeman slower. The setup and functionality of the Zeeman slower is described in detail in chapter 2.1.1. Also attached to the vacuum chamber is a small spectroscopy chamber which is used for frequency stabilization of the MOT laser system (see section 3.5.1 for details).

The magnetic field that is needed for the magneto-optical trap is generated by two magnetic field coils in an anti-Helmholtz configuration. Both coils are mounted outside of the chamber (see figure 3.1). The big coil (diameter: 15.2 cm) is attached on the top of the experimental

chamber. The small coil (diameter: 3.4 cm) is mounted inside a recessed flange, so that the distance between this coil and the MOT is as small as possible and a large magnetic field gradient can be realized. For the compensation of residual magnetic fields at the position of the atoms, two additional coils are attached to the chamber (see figure 3.1).
In the following the interior of the experimental chamber is described which has been changed during the two stages of the experiment. The difference in the setup is illustrated in figure 3.2.

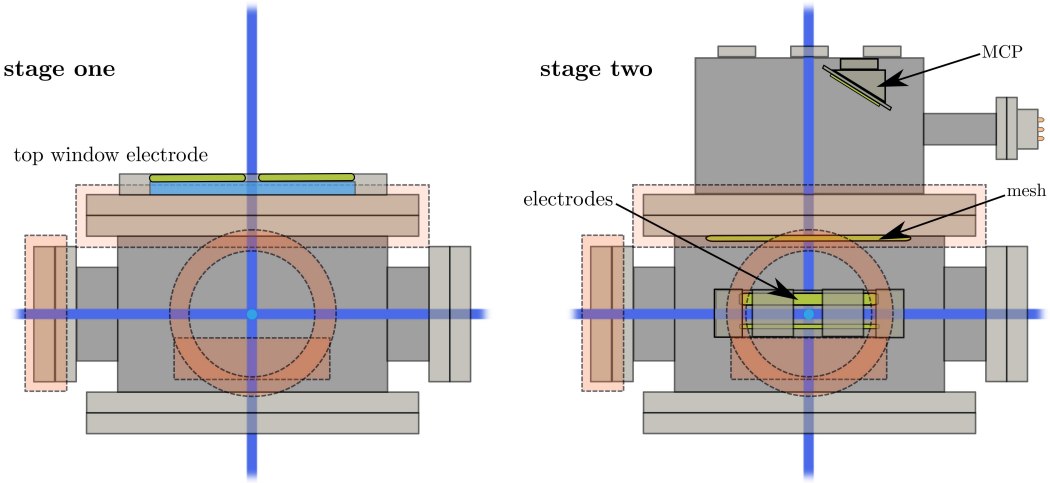


**Figure 3.2.:** *Sketch of the experimental chamber in the two stages of the experiment. In the first stage, on the left side, the electrode for electric field control is mounted on the top window of the chamber. There are no components inside the chamber. On the right is the second stage of the experiment. An extension flange is added to the chamber to make room for the MCP. A wire mesh is installed between the MCP and the Rydberg atoms. The electrodes for the electric field control are mounted on a 2D resonator. The optical access for the resonator is provided by four windows on the top of the chamber. A fifth window in the center gives access to the vertical MOT beam.*

### First stage

In stage one, the experimental chamber had no electrode inside the vacuum chamber. As an electrode a cooper plate with a diameter of 150 mm and a center hole of 25 mm for optical access was used. The plate was mounted on the top window of the chamber and the distance between the atoms and the electrode was approximately 75 mm. There was no other electrode or device installed in the apparatus.

#### Second stage

In the second (current) stage, several changes have been done to the setup of the experimental chamber. With the addition of a two dimensional resonator [64] (see figure 3.3), it is now possible to trap the atoms conservatively in a two dimensional optical lattice. The optical lattice will be used in future experiments to trap the atoms.
The electrodes for the electric field compensation and the high voltage pulse generation, are attached to the resonator. A detailed description of the electrode setup and a simulation of the electric field inside the vacuum chamber is given in section 3.2.
The MCP for Rydberg ion detection is located inside the extension flange (see figure 3.8). In order to shield the Rydberg atoms from the electric field of the MCP, an electrically conductive mesh is mounted between the MCP and the location of the MOT, where the Rydberg atoms are produced.

## 3.2. Electric fields

Due to the large polarizability of Rydberg states, which scales with $n^7$ (see chapter 1.1), they are very sensitive to electric fields. The Stark effect splits and shifts the energy levels (see section 2.3.1 for more details). It is also possible to ionize the Rydberg atoms with a sufficiently large electric field (more details in chapter 6). For investigation of the Stark effect as well as for a well-controlled field ionisation it is important to precisely control the electric field in our experiment. The section 3.2.1 describes the basics of the finite integration technique, which is used to simulate the electric field. In section 3.2.2 the setup of the electrodes and the resulting electric field is described. It also explains how the high voltage pulse pattern for the ionisation of the Rydberg atoms is generated (see 3.2.5 section). Section 3.2.4 presents a detailed study about the geometry of the electric field, that it generated by the electrode setup.

### 3.2.1. Simulation of the electric field

A simulation of the electric field in the vacuum apparatus is shown in chapter 3.2.3. The electric field is numerically simulated with a software[1], that uses the finite integration

[1] CST Studio Suite

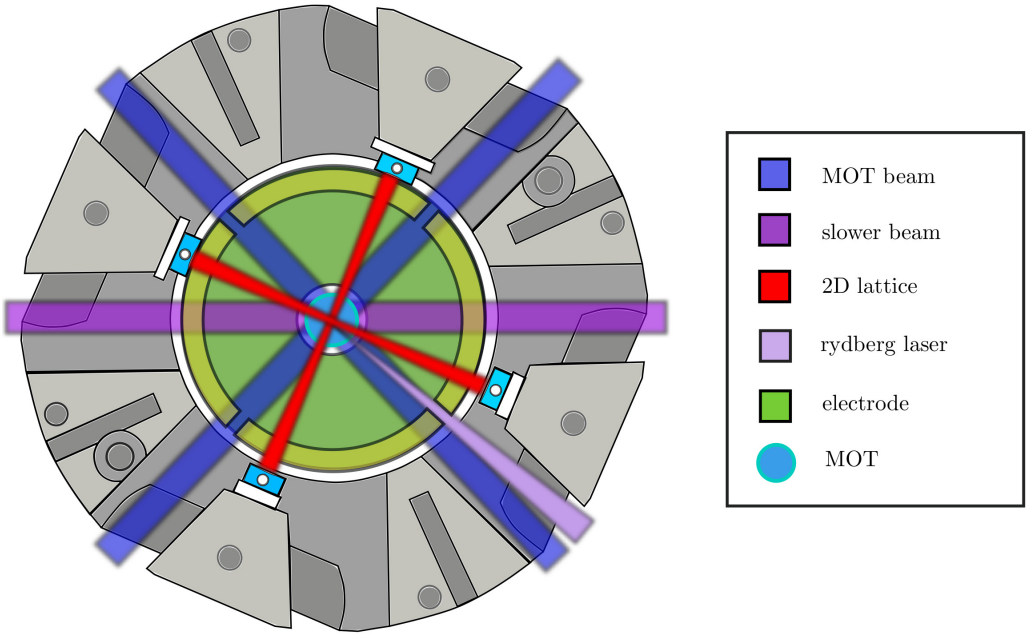


**Figure 3.3.:** *Sketch of the intra-vaccum resonator setup. Two perpendicular confocal resonators form a two-dimensional optical lattice. Both resonators have a length of approximately* 50 mm *and a beam waist of* 50 $\mu$m*. The laser beams are coupled into the resonator via a mirror, mounted behind the resonator mirrors. These deflection mirrors are aligned in such a way that laser beams ,coming from above, enter the resonator. The resonator is designed to provide optical access to the MOT beams, the Rydberg laser, the slower beam and the camera. The electrodes for electric field control are also attached to the resonator setup.*

technique (FIT) to solve the Maxwell equations. One input for the simulation is a three dimensional model of all components of the experiment (electrode setup, MCP and vacuum chamber), including the material properties. For each of these components an electric potential value is defined. With this information the FI-method can calculate the three dimensional electric field. In the following the FI-method is described in detail. The following description of the method is a summary of reference [65].

The FI-method divides the complete system into mesh cells. Thereby the mesh is not limited to a Cartesian coordinate system of a specifically shaped mesh. Actually the simulations performed in this thesis are made with a hexahedral mesh in a Cartesian coordinate system.

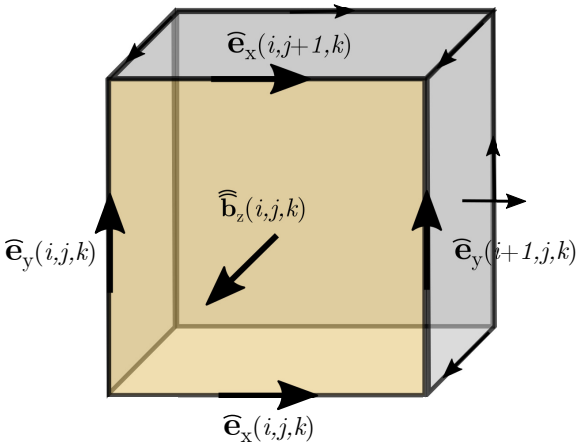


**Figure 3.4.:** *Sketch of the cell $V_{i,j,k-1}$ in cell complex $G$. The edges of the surface $A$ are associated with the electric grid voltage $\widehat{e}$ and the corresponding surface is associated with the magnetic facet flux $\widehat{\widehat{b}}$. The figure is reproduced from [65].*

For the sake of simplicity the following explanation is based on a brick shaped mesh in Cartesian coordinate system. Therefore, the cell complex for Cartesian coordinates is given by,

$$\begin{aligned} G \;&:=\; \{V_{i,j,k} \in R^3 \mid V_{i,j,k} := [x_i, x_{i+1}] \times [y_j, y_{j+1}] \times [z_k, z_{k+1}]\,, \\ &\quad i = 1, ..., I-1,\ j = 1, ..., J-1,\ k = 1, ..., K-1\}, \end{aligned} \tag{3.1}$$

where the nodes $(x_i, y_j, z_k)$ are enumerated with the parameters $i$, $j$ and $k$ along the $x$-, $y$- and $z$-axis. The total number of mesh point is therefore given by

$$N_p \;:=\; I \cdot J \cdot K\,. \tag{3.2}$$

For the simulation of the the electric field we start with Faraday's law in integral form. The law applied to a single cell in the grid $G$ is given by

$$\oint_{\partial A} \vec{E}\,(\vec{r}, t) \cdot d\vec{s} = -\iint_A \frac{\partial}{\partial t} \vec{B}\,(\vec{r}, t) \cdot d\vec{A}\; \forall\, A \in \mathcal{R}^3, \tag{3.3}$$

where $\vec{E}\,(\vec{r}, t)$ is the electric- and $\vec{B}\,(\vec{r}, t)$ magnetic-field. $A$ represents a facet of the cell. For a facet oriented along the $z$-axis the law can be rewritten as

$$\widehat{e}_x\,(i, j, k) + \widehat{e}_y\,(i+1, j, k) - \widehat{e}_x\,(i, j+1, k) - \widehat{e}_y\,(i, j, k) = -\frac{d}{dt}\,\widehat{\widehat{b}}_z\,(i, j, k)\;, \tag{3.4}$$

where the scalar value

$$\widehat{e}_x\,(i,j,k) \;=\; \int_{(x_i,j_j,z_k)}^{(x_{i+1},j_j,z_k)} \vec{E}\cdot d\vec{s} \tag{3.5}$$

is the electric voltage along one edge of the facet $A_z(i,j,k)$ as shown in figure 3.4. The magnetic flux through the cell facet $A_z(i,j,k)$ is represented by the scalar value

$$\widehat{\widehat{b}}_z\,(i,j,k) \;=\; \int_{A_z(i,j,k)} \vec{B}\cdot d\vec{A}. \tag{3.6}$$

The discrete form of Faraday law eq.3.4 is valid for each single facet and can be extended to larger facet areas by:

$$A \;=\; \bigcup A(i,j,k) \tag{3.7}$$

with the relation

$$\sum \oint_A (i,j,k) = \oint_A \,. \tag{3.8}$$

By ordering the electric voltages $\widehat{e}(i,j,k)$ and the magnetic face flux $\widehat{\widehat{b}}(i,j,k)$ lexicographically over the complete cell system $G$ the grid voltages and magnetic field fluxes can be written in the form of two column vectors

$$\widehat{e} := (\widehat{e}_{x,n} \mid \widehat{e}_{y,n} \mid \widehat{e}_{z,n})^T_{n=1,\ldots,N_p} \in \mathcal{R}^{3N_p} \tag{3.9a}$$

$$\widehat{\widehat{b}} := (\widehat{\widehat{b}}_{x,n} \mid \widehat{\widehat{b}}_{y,n} \mid \widehat{\widehat{b}}_{z,n})^T_{n=1,\ldots,N_p} \in \mathcal{R}^{3N_p}. \tag{3.9b}$$

With the definitions 3.9a and 3.9b and the relation 3.8, equation 3.4 can be written in the matrix form,

$$\underbrace{\begin{pmatrix} \cdots\cdots\ \cdots & & & \\ 1\cdots\ 1\cdots & -1\cdots & -1 & \\ \cdots\cdots\ \cdots & & & \end{pmatrix}}_{\mathbf{C}:=} \underbrace{\begin{pmatrix} \widehat{e}_{n_1} \\ \vdots \\ \widehat{e}_{n_2} \\ \vdots \\ \widehat{e}_{n_3} \\ \vdots \\ \widehat{e}_{n_4} \end{pmatrix}}_{\widehat{\mathbf{e}}} = -\frac{d}{dt} \underbrace{\begin{pmatrix} \vdots \\ \widehat{\widehat{b}}_n \\ \vdots \end{pmatrix}}_{\widehat{\widehat{\mathbf{b}}}} \tag{3.10}$$

The matrix $\mathbf{C}$ has only the coefficients $\mathbf{C}_{i,j} \in \{-1, 0, 1\}$ and contains the topological information on the incidence relation of the cell edges within $G$ and their orientation. $C$ represents the discrete *curl*-operator on the grid $G$.

The next differential operator that has to be discretized is the *divergence* operator $\mathbf{S}$. This operator can be derived from the Maxwell's equation describing the non-existence of magnetic charges (Gauss's law of for magnetism)

$$\iint_{\partial V} \vec{B}\,(\vec{r}, t) \cdot d\vec{A} = 0 \qquad \forall\, V \in \mathcal{R}^3. \tag{3.11}$$

Considering this equation for a cell $V_{i,j,k}$ as shown in figure 3.5 yields the following equation:

$$\begin{aligned} -\widehat{\widehat{b}}_x\,(i,j,k) + \widehat{\widehat{b}}_x\,(i+1,j,k) - \widehat{\widehat{b}}_y\,(i,j,k) + \widehat{\widehat{b}}_y\,(i,j+1,k) & \\ -\widehat{\widehat{b}}_z\,(i,j,k) + \widehat{\widehat{b}}_z\,(i,j,k+1) &= 0. \end{aligned} \tag{3.12}$$

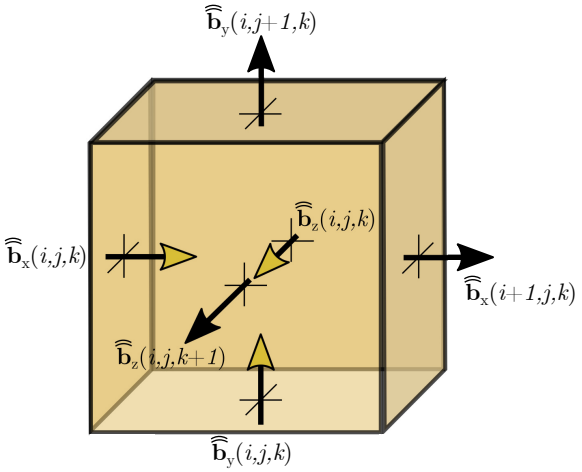


**Figure 3.5.:** *Sketch of the magnetic flux trough the facets of a cell of the cell complex $G$. The sketch shows the flow in and out of the volume. Due the the non-existence of magnetic charges the net flow is zero.The figure is reproduced from [65].*

Expanding equation 3.12 to the complete cell complex $G$ yields the following matrix form of the Maxwell equation

$$\underbrace{\begin{pmatrix} & \cdots & \cdots & \cdots & & \\ \cdots & -1 & 1 & -1 & 1 & -1 & 1 \cdots \\ & \cdots & \cdots & \cdots & & \end{pmatrix}}_{\mathbf{S}:=} \underbrace{\begin{pmatrix} \vdots \\ \widehat{\widehat{b}}_{m_1} \\ \widehat{\widehat{b}}_{m_2} \\ \widehat{\widehat{b}}_{m_3} \\ \widehat{\widehat{b}}_{m_4} \\ \vdots \end{pmatrix}}_{\widehat{\widehat{\mathbf{b}}}} = 0\,. \tag{3.13}$$

Just as the *curl*-operator $\mathbf{C}$ the discrete divergence (source) operator $\mathbf{S} \in \mathcal{R}^{N_p \times 3N_p}$ depends on the grid topology.

For the discretization of the two remaining Maxwell equations a second cell complex $\tilde{G}$ has to be introduced. The second grid is defined by taking the center of the cells of the primary grid $G$ as the grid-points of the grid $\tilde{G}$, as shown in figure 3.6. This definition ensures a one-to-one relationship between the cells edges of $G$ and the cell surfaces of $\tilde{G}$ and vice versa. If we integrate the magnetic field intensities $\vec{H}$ along the edges $\tilde{L}_k$ of the so defined

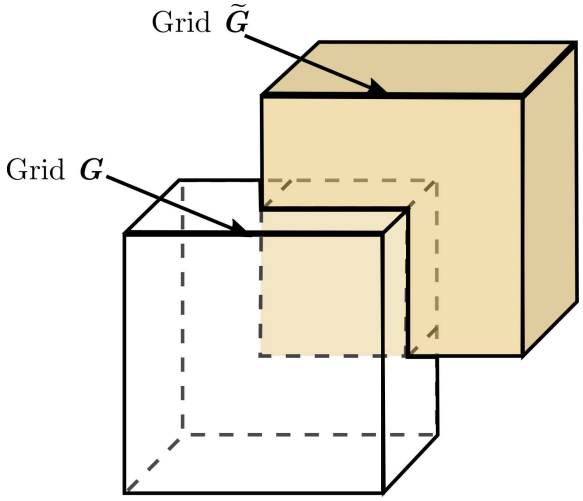


**Figure 3.6.:** *Relationship between the two cell complexes $G$ and $\tilde{G}$. The vertices of $\tilde{G}$ are the foci of cells of complex cell system $G$. There is a one-to-one relationship between the cells edges of $G$ and the cell surfaces of $\tilde{G}$ and vice versa. The figure is reproduced from [65].*

dual grid we get the magneto motive force

$$\widehat{h}_k = \int_{\tilde{L}_k} \vec{H} \cdot d\vec{s}, \tag{3.14}$$

where the physical unit of the force is *Ampére*. The electric currents $\vec{I}$ and the dielectric fluxes $\vec{D}$ on the surfaces of $\tilde{G}$ are defined in analogy to the grid voltages and the magnetic facet fluxes on $G$.

The integral of the charge density in a cell of the dual grid $\tilde{G}$ can be described as a point charge on the grid point of the primary grid $G$, which is placed in the center of a cell of $\tilde{G}$ with the volume $\tilde{V}$.

The Ampére's law in the integral form is given by

$$\oint_{\partial \tilde{A}} \vec{H}\left(\vec{r},t\right) \cdot d\vec{s} = -\iint_{\tilde{A}} \left( \frac{\partial}{\partial t} \vec{D}\left(\vec{r},t\right) + \vec{J}\left(\vec{r},t\right) \right) \cdot d\vec{A} \qquad \forall\, \tilde{A} \in \mathcal{R}^3, \tag{3.15}$$

where $\vec{J}$ is the current density through a surface of the cell of the grid $\tilde{G}$. The discretization of Ampere's law follows in complete analogy to the discretization of the Faraday's law. To obtain the displacement current $\frac{\partial}{\partial t}\vec{D}\left(t\right)$ and the conductive current $\vec{J}$ through the cell facet, the magnetic grid voltages of the considered cell are summed up.

The Gauss' law in integral form

$$\iint_{\partial\tilde{V}} \vec{D}\,(\vec{r},t)\cdot d\vec{A} = q \qquad \forall\,\tilde{V}\in\mathcal{R}^3, \tag{3.16}$$

can also be discretized for the dual grid $\tilde{G}$. The discretization of Gauss' law leads to the topological grid operator $\tilde{S}$ for the dual discrete *divergence* and the discretization of the Ampére's law results in the operator $\tilde{C}$, which is the dual *discrete* curl operator. The complete set of discrete matrix equation for the grid pair $\{G,\tilde{G}\}$ is called Maxwell-Grid-Equations (MGE) and is given by:

$$\mathbf{C}\,\widehat{\mathbf{e}} = -\frac{d}{dt}\,\widehat{\mathbf{b}}, \tag{3.17a}$$

$$\mathbf{S}\,\widehat{\mathbf{e}} = 0, \tag{3.17b}$$

$$\tilde{\mathbf{C}}\,\widehat{\mathbf{h}} = -\frac{d}{dt}\,\widehat{\mathbf{d}} + \widehat{\mathbf{j}}, \tag{3.17c}$$

$$\tilde{\mathbf{S}}\,\widehat{\widehat{\mathbf{d}}} = \mathbf{q}. \tag{3.17d}$$

Here $\widehat{\mathbf{d}}$ is the dielectric flux vector and $\widehat{\mathbf{j}}$ conductive current vector of the cell complex pair $\{G,\tilde{G}\}$, in analogy to the definition 3.9a and 3.9b. In the context of the FI-method it is convenient to use electric grid voltages, which are associated with the cell edges. These grid voltages can be expressed as a difference of two nodal potential values $\Phi(i,j,k)$, which are associated with intersecting grid mesh point of the grid $G$. This difference is given by

$$-\Phi(i+1,j,k) + \Phi(i,j,k) = \widehat{e}_x(i,j,k) \tag{3.18}$$

Following the same collecting scheme as in derivation of the MGE yields the relation,

$$\widehat{\mathbf{e}} = -\mathbf{G}\Phi, \tag{3.19}$$

where $\mathbf{G}$ is the discrete *gradient* matrix

$$\mathbf{G} = -\widehat{\mathbf{S}}^T. \tag{3.20}$$

The same method can be used to introduce a magnetic scalar nodal potential vector $\Psi$. There the magnetic potentials are associated with the vertices of the dual grid $\tilde{G}$. Following

the derivation yields the following relationship:

$$\widehat{\mathbf{h}} = -\tilde{\mathbf{G}}\Psi = -\mathbf{S}^T\Psi, \tag{3.21}$$

Until now the discretization of the Maxwell equations has lead to a set of equations which holds only the information about the integral state variables, which are either associated with vertices (potentials), edges (voltages) surfaces (fluxes) or the cell volume (charges). The approximation enters this method, when the two cell complexes are related to each other over the constitutive material equations. Under the condition that the two cell complexes $G$ and $\tilde{G}$ are orthogonal and have a one-to-one relationship between their facets and edges, the discrete material matrix relations are,

$$\widehat{\mathbf{d}} = \mathbf{M}_\epsilon\, \widehat{\mathbf{e}} + \widehat{\widehat{\mathbf{p}}}, \tag{3.22a}$$

$$\widehat{\mathbf{j}} = \mathbf{M}_\kappa\, \widehat{\mathbf{e}}, \tag{3.22b}$$

$$\widehat{\mathbf{h}} = \mathbf{M}_\nu\, \widehat{\mathbf{b}} + \widehat{\mathbf{m}}. \tag{3.22c}$$

Where $\mathbf{M}_\epsilon$ is the permittivity matrix, $\mathbf{M}_\kappa$ is the matrix of conductivities and $\mathbf{M}_\nu$ is the matrix of reluctivities. The vectors $\widehat{\widehat{\mathbf{p}}}$ and $\widehat{\mathbf{m}}$ arise from the permanent electric and magnetic polarisations.

In figure 3.7 an example of the coupling of the grid $G$ and $\tilde{G}$ over the constitutive material equations is shown. There the electric field voltage $\widehat{\mathbf{e}}_m$ is related to the facet flux $\widehat{\mathbf{j}}_m$.
Since the four MGE 3.17a-3.17d are an exact representation of the Maxwell equation, the error in the FI-method appears in the discrete constitutive material equations 3.17a-3.17c. There are several averaging methods and cell filling techniques to handle the error of this method (see reference [65]). The solver of the software[2] we use to simulate the electric field has therefore a refinement step of the mesh in the solving process to reduce the error of the simulation under a pre-chosen limit.

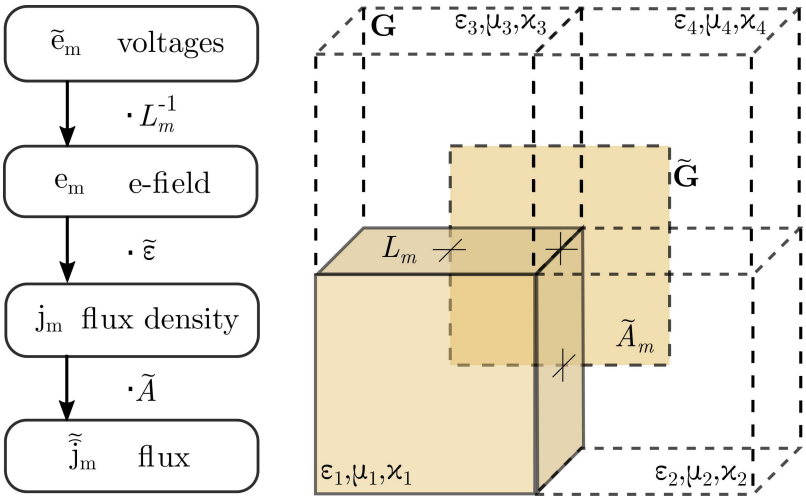


**Figure 3.7.:** *The coupling between the grid $G$ and the dual grid $\tilde{G}$ is done via the constitutive material equations. Here the electric grid voltage $\widehat{e}_m$, allocated on the edge $L_m \in G$, is couple to the facet flux $\widehat{\tilde{j}}_m$ on the dual cell facet $\tilde{A}_m \in \tilde{G}$. The coupling relation reads as $j_m = \overline{\kappa}_m e_m$, where $j_m = \widehat{\tilde{\mathbf{j}}}_m / \int_{\tilde{A}_m} dA$ and the averaged electric field intensity $e_m = \widehat{\mathbf{e}}_m / \int_{\tilde{L}_m} dA$. The permittivity of the cell $\tilde{V}$ $\overline{\kappa}_m$ is derived by averaging the four cell permittivities $\kappa_1$,...,$\kappa_4$. The figure is reproduced from [65].*

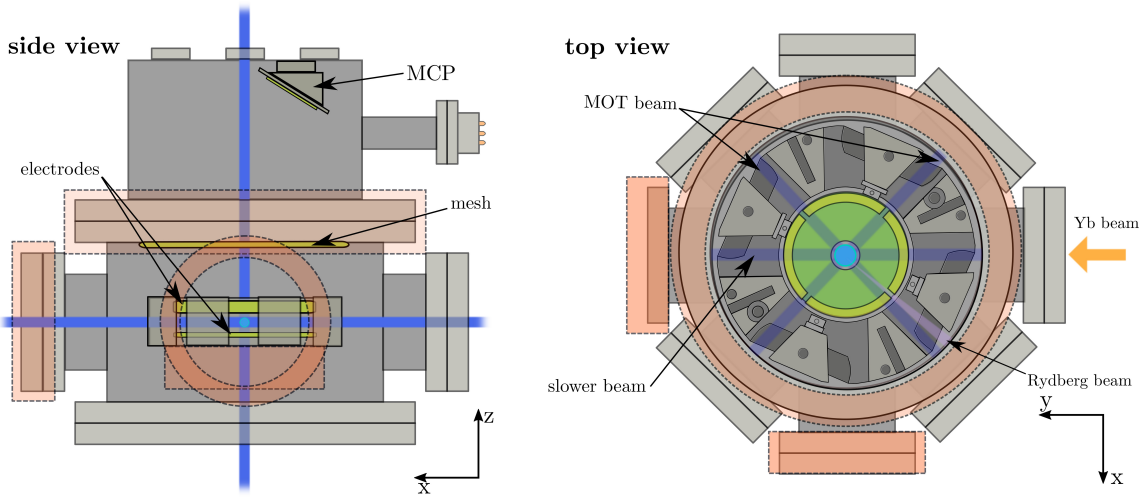


**Figure 3.8.:** *Close up of the experiment chamber. The electrodes are colored in green. The magnetic coils are red. The chamber itself is connected to ground. The upper electrode is a four segmented ring. The lower electrode is a plate with 10 mm hole in the center for optical access. The mesh above the electrodes has also a hole for the same reason.*

### 3.2.2. Electrode setup

A close up of the experimental chamber with all components is shown in figure 3.8. The electrodes for the electric field compensation and for the ionisation pulse consist of a segmented ring electrode and a plate. The ring is divided into four segments and has a diameter of 37 mm, as can be seen in figure 3.9. The horizontal field produced by segment 1 and 3 points towards the MCP (see figure 3.10)(see figure 3.10). The axis of segment two and four is orientated orthogonally to this axis. The plate below the ring has a 10 mm hole in its center passing through of the vertical MOT beams. The distance between the plate and the ring is 7.5 mm. The electrodes are attached to the resonator in a way that the atoms are located in the common center of the resonator and the electrode setup. A mesh above the electrodes shields the atoms against the electric field from the MCP, as can be seen in figure 3.10. The mesh has a center hole for the optical access of the vertical MOT beam. The MCP is mounted inside the extension flange at the top of the experimental chamber. Because of the vertical MOT beam the MCP has to be mounted off axis. The MCP is tilted such that the effective surface is facing the MOT.

a) b)

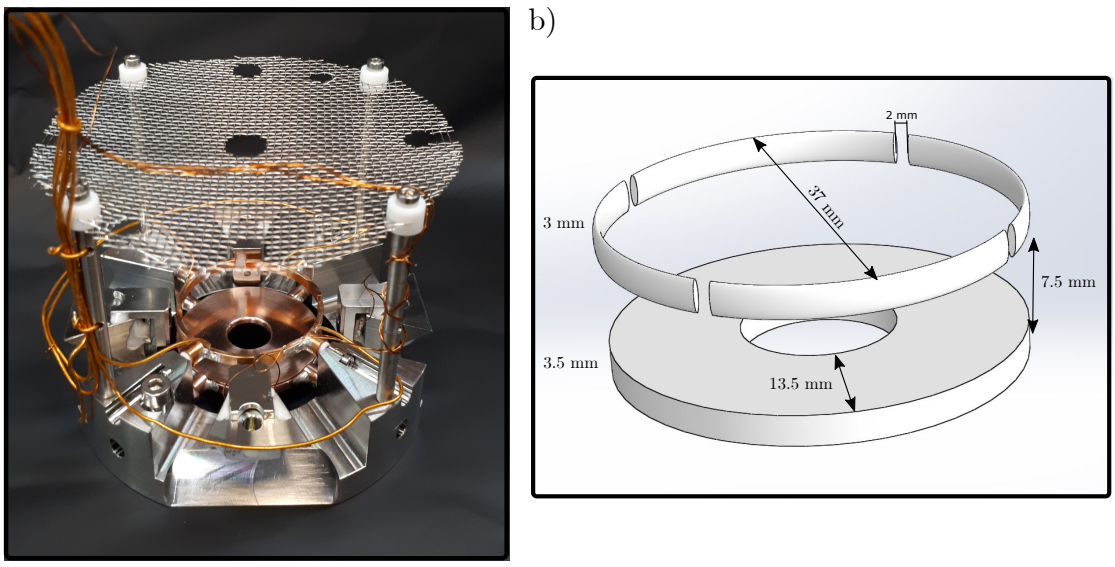


**Figure 3.9.:** *a) Picture of the electrode setup including the intra-vacuum resonator, the wiring of the electrodes and the mesh. b) Sketch of the electrode setup including the spatial dimensions.*

[2] CST Studio Suite

### 3.2.3. Compensation field

Patch charges on dielectric surfaces inside the experimental chamber cause a stray electric background field, that has to be compensated by the electrodes inside the chamber. A typical compensation field in our experiment is shown in figure 3.10.

To determine this field we use the turning point of a Stark map of highly excited Rydberg states ($n > 70$). A detailed description of measurement technique can be found in section 4.1. To simplify the optimization of the field compensation we reduce the amount of free parameters in our setup by combining the six potentials $U_1$,$U_2$,$U_3$,$U_4$,$U_{plate}$ and $U_{mesh}$, according to the formulas below. First we choose the coordinate system, as shown in figure 3.10. Then we relate the potentials of the electrodes to four parameters $P_x$,$P_y$,$P_z$ and

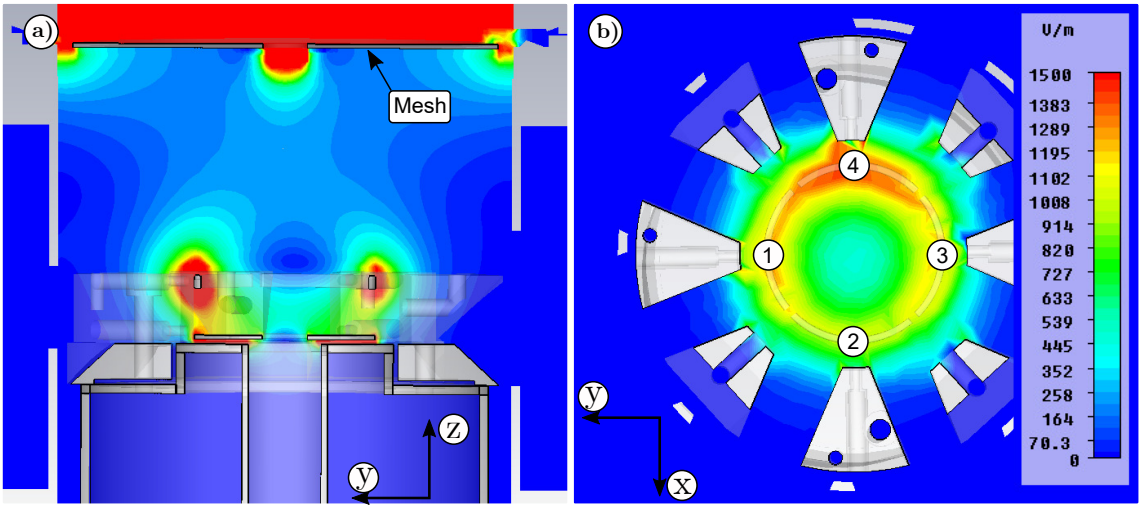


**Figure 3.10.:** *Contour plot of a typical compensation field inside the experimental chamber. This field was determined by finding the turning point of a Stark map of highly excited Rydberg states ($n > 70$). The corresponding voltage applied to the electrodes can be found in table 3.1. The simulation also includes the MCP, which is held at 2500 kV. The mesh shields the lower part of the experimental chamber from the electric field of the MCP, as can be seen in the side view a). For a better view of the stary field, the maximum value of the used color coding scheme is chosen to 1500 V/m. The compensation field has to be stronger in the y-axis, which is defined by electrodes two and four, as can be seen in the top view b).*

$P_{offset}$, which are controlled in the experiment:

$$U_1 = A \cdot \left( P_{offset} - \frac{P_x}{2} + \frac{P_z}{2} \right) \tag{3.23}$$

$$U_2 = A \cdot \left( P_{offset} - \frac{P_y}{2} + \frac{P_z}{2} \right) \tag{3.24}$$

$$U_3 = A \cdot \left( P_{offset} + \frac{P_x}{2} + \frac{P_z}{2} \right) \tag{3.25}$$

$$U_4 = A \cdot \left( P_{offset} + \frac{P_y}{2} + \frac{P_z}{2} \right) \tag{3.26}$$

$$U_{plate} = A \cdot \left( P_{offset} - \frac{P_z}{2} \right) . \tag{3.27}$$

The parameter $A$ just scales the amplitude of the electric field and can therefore be used to scale the compensation field without changing its orientation. It is initially set to one for the compensation field. The other parameters are not completely independent of each other. Therefore we have to proceed iteratively in the search for the compensation field. Experimentally we first set $P_x$,$P_y$ and $P_{offset}$ to zero and find the optimal value for $P_z$. Then we proceed with the optimization of the field in the x- and y-axis. Before we repeat the process, we find the optimal value for $P_{offset}$, which changes the symmetry in $P_z$. After several iterations the algorithm converges and we get the following values for the parameters,

**Table 3.1.:** Parameters for the resulting voltages for the compensation field and the absolute value of the compensation field $|\vec{E}|$ at the nominal MOT position (after mesh compensation). The electric field is determined with the simulation described in section 3.2.1.

| parameter | value | potential | voltage $[V]$ |
|---|---|---|---|
| $P_x$ | -0.5 | $U_1$ | 13.02 |
| $P_y$ | 5.5 | $U_2$ | 10.38 |
| $P_z$ | 17.1 | $U_3$ | 12.58 |
| $P_{offset}$ | 6.0 | $U_4$ | 15.22 |
| $A$ | 0.88 | $U_p$ | -2.24 |
| | | $U_{mesh}$ | -5.00 |

$$|\vec{E}(A = 1)| = 432.98\,\mathrm{V/m} \text{ and } |\vec{E}(A = 0.88)| = 390\,\mathrm{V/m}$$

The voltage $U_{mesh}$ is adjusted according to the intensity of the ion signal, subsequently

compensated with the electrodes by adjusting the amplitude factor $A$, which changes its value from initially 1 to 0.88. With the parameters shown in table 3.1 the electrodes generate an electric field that compensates the electric stray field at the MOT position. At the same time, these parameters allow for maximum ion signal after electric field ionization. To be able to measure the ions at all, they must be generated with a high voltage pulse. This pulse, the acceleration and deflection of the ions are described in section 3.2.5.

### 3.2.4. Spatial variation of the compensation and ionisation field

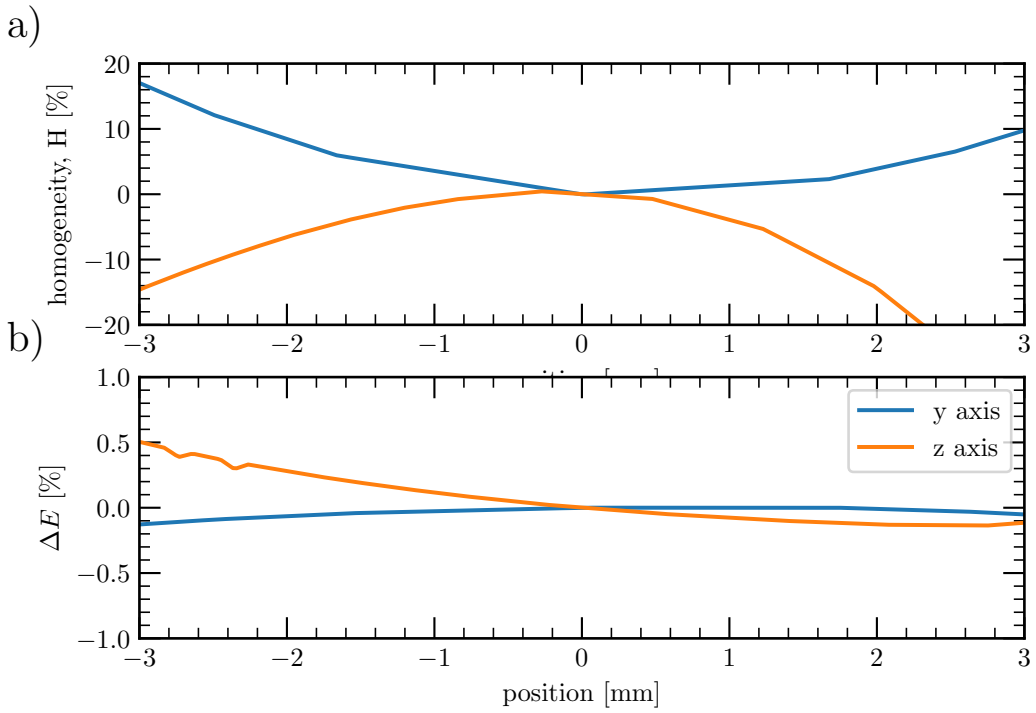


**Figure 3.11.:** *Analysis of the homogeneity and relative change of the compensation field generated by the electrodes. a) Homogeneity of the compensation field along the y and z axis. b) Variation of the change of the electric field $\Delta E$ (see equation 3.30) along the y and z axis. For the determination of the change, the electric field is varied by* 10%.
*The analysis of the Homogeneity yields that the electric field changes by approximately* 10% *on the horizontal axis in the region of* 2 mm *around the MOT position. On vertical axis the electric field changes up to 15% in the* 2 mm *uncertainty region of the MOT position. The variation of the change of the electric field is less than 0.5% on both axis.*

Besides the absolute value of the electric field the spatial variation of the compensation

(figure 3.11) and ionisation field (figure 3.13) has a big impact on the excitation and ionisation of the Rydberg atoms, as well as for the determination of the polarizability of the Rydberg atoms.

The homogeneity $H$ for the horizontal axis y and the vertical axis z is given by

$$H_y = \left(\frac{E_y}{E_c} - 1\right) \cdot 100\% \tag{3.28}$$

$$H_z = \left(\frac{E_z}{E_c} - 1\right) \cdot 100\%, \tag{3.29}$$

is important for the excitation of the Rydberg atoms. $E_c$ is the absolute value of the electric field at the nominal position of the MOT center. The horizontal homogeneity $H_y$ (shown in figure 3.11a blue line) has the largest impact on the excitation of the states, because the excitation laser is focussed onto the MOT position and slices through the MOT only horizontally on approximately the bisector of the $y$ and $x$ axis. For the discussion of the horizontal homogeneity the electric field along the $y$-axis is used, because the in-homogeneity on this axis is the largest as can be seen in figure 3.11. The simulation of the compensation field yields a horizontal homogeneity of 10% in a region of 2 mm around the center of the setup. The graph in figure 3.11 is a line-out from the simulation of the compensation field, shown in figure 3.10.

For the determination of the polarizability of a Rydberg state (see chapter 5) it is important to quantify the uniformity of the change of the electric field while the electrode voltages are changed. Therefore we define a uniformity parameter

$$\Delta E_i = \left(\frac{E_{high,i}}{E_{low,i}} - \frac{E_{high,c}}{E_{low,c}}\right) \cdot 100\% \,. \tag{3.30}$$

where $E_{high}$ and $E_{low}$ are the absolute values of the electric field along the $y$- or $z$-axis for two sets of electrode voltages differing by 10% in amplitude. Figure 3.11 b) shows variation of the compensation field $\Delta E$ along the horizontal y- and z-axis. These two simulations yield a maximal change of the variation of the compensation field of less than 0.5% along the z-axis and and less than 0.2% along the y axis in a region of 2 mm around the center position. This analysis shows that the exact position has no big influence on the scaling of electric field with the amplitude of the applied voltage. In contrast to the homogeneity $H$, which is up to one order of magnitude more sensitive to the position than the electric field

change $\Delta E$. Therefore the homogeneity of the electric field will dominate the error of the polarizability of the Rydberg states. The homogeneity changes by $\pm 15\%$ in the probable stay volume of the MOT ($\pm 2\,\mathrm{mm}$).
Another factor that has to be considered by the determination of the polarizability and the ionisation threshold is the uncertainty of the distance between the segmented electrode ring and the electrode plate. Simulations with a variation of the distance by $\pm 500\,\mu\mathrm{m}$ show a change of $\pm 1.5\%$ of the absolute value of the electric field at the nominal MOT position. The uncertainty of the MOT position and the uncertainty of the distance between the electrodes therefore results in an uncertainty of 16.5% of the absolute value of the electric field. Due to quadratic scaling of the polarizability with the electric field (see chapter 5) this uncertainty causes an relative error of 36% in the determination of the polarizability of the Rydberg states.

### 3.2.5. Ionisation pulse

One way to detect the Rydberg atoms is via field ionisation [1] of the atoms with a sufficiently large electric field. In our setup, this field is generated by a high voltage pulse applied to the plate electrode. The time profile of this pulse (see figure 3.12) has to be well defined and as short as possible. In our experiment, pulses are generated using self-built high voltage switches. These switches can produce a minimal pulse length of 180 ns and the amplitude in our experiment can be varied between 30 V to 450 V. For the detection of the ions three steps are important.

1. Ionisation of the Rydberg atoms.
2. Acceleration towards the MCP.
3. Deflection of the ions towards the active surface of the MCP.

These three steps aren't independent of each other, but for the measurement of the Rydberg atoms they have to be separated as far as possible. For the well-defined ionisation of Rydberg states, one needs to know the electric field, that is generated by the high voltage pulse. For this purpose, the electric field is simulated with the program described in section 3.2.3. For the conversion between the applied voltage and the electric field, the electric field

in our setup is simulated with 30 V and with 450 V applied to the plate. The electric field at the MOT position in both cases is:

$$\vec{E}_{30} = \begin{bmatrix} 0.9202 \\ -19.361 \\ 966.10 \end{bmatrix} \left[\frac{V}{m}\right] \qquad \vec{E}_{450} = \begin{bmatrix} 0.9310 \\ -19.400 \\ 18468.5 \end{bmatrix} \left[\frac{V}{m}\right] \tag{3.31}$$

Where the x and y components of the ionization pulse originate from the compensation field. Due to technical reasons, the voltages at the upper four ring segments are not switched during the ionization pulse. Linear interpolation leads to the electric field calibration

$$\vec{E}\,(U) \quad = \begin{bmatrix} 0.9202 \\ -19.361 \\ 966.10 \end{bmatrix} + \quad \begin{bmatrix} 0.00002 \\ -0.00095 \\ 41.6723 \end{bmatrix} \left[\frac{1}{m}\right] \cdot (U - 30\,\mathrm{V}) \ , \tag{3.32}$$

or

$$|\vec{E}| = 966.29 + 41.67\,[\,1/\mathrm{m}] \cdot (U - 30\,\mathrm{V}) \ . \tag{3.33}$$

In order to separate the ionisation and the acceleration of the ions, it is possible to apply two different high voltage pulses to the plate electrode (see figure 3.12). Both pulses can be independently adjusted in pulse length and amplitude. Because of restriction due to the logic circuit of the high voltage switch, there is a minimal delay of 330 ns between both pulses.

To obtain the strongest possible ion signal, the ions have to be deflected, so that their trajectory hits the effective surface of the MCP. This deflection is realized by a third pulse applied to the first segment of the electrode (see figure 3.10), which is at the opposite side of the MCP. This pulse deflects the ions towards the MCP. To ensure that the detection is as independent as possible of the ionization process, the following conditions are used when designing the time sequence of the pulses. As a first condition the ionisation pulse has to be as short as possible, so that the resulting (unwanted) acceleration due to this pulse, is as small as possible. Second, the accelerating pulse should not generate secondary ionisation and thus shall to have an amplitude below the electric-field ionization threshold. The third condition requires a deflection pulse that has to be as high as

possible, so that the initial momentum of the ions after ionisation has a minimal impact on their trajectories. Another effect that has to be considered is the ionisation caused by the deflection pulse. By only applying the deflection pulse to the Rydberg atoms we experimentally verified that ions created by the deflection pulse are not detected by the MCP which is why the effect can be ignored. In a typical ionisation sequence, the

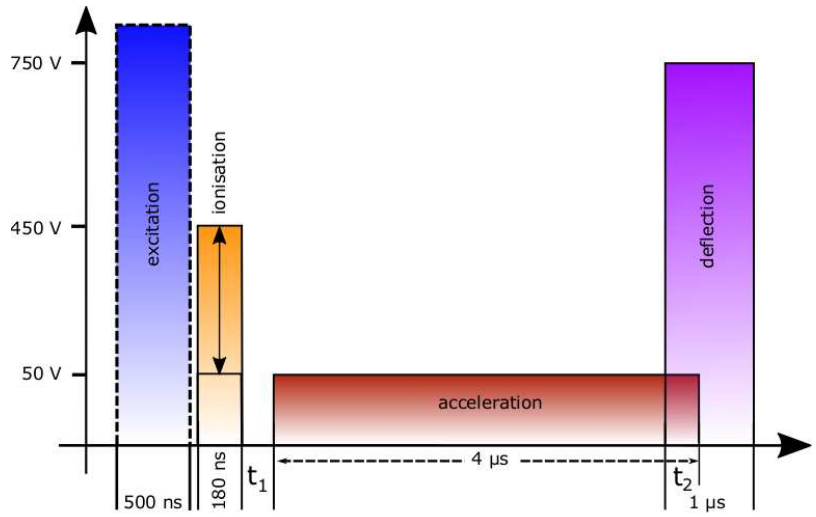


**Figure 3.12.:** *Time profile of the high voltage pulses and the light pulse for the excitation of the Rydberg atoms (blue). The shown amplitude of the light pulse is just for demonstration and is not correlated to the voltage axis. The delay $t_1$ between ionisation pulse (yellow) and acceleration pulse (red) is* 330 ns. *The overlap $t_2$ between the acceleration pulse an the deflection pulse (purple) is* 570 ns. *The ionisation pulse can be adjusted in amplitude. The ionisation pulse and the acceleration pulse are applied to the plate electrode. The deflection pulse is applied to segment one , see figure 3.10.*

resulting time sequence is shown in figure 3.12. The duration of the ionisation pulse is 180 ns and is followed by a 4 $\mu$s long acceleration pulse. The absolute value of the electric field of the acceleration pulse is 21.4 V/cm ($U_p = 50$ V) and the delay between the pulses is $t_1 = 330$ ns. The acceleration pulse is overlapping with the deflection pulse. The deflection pulse starts $t_2 = 570$ ns before the acceleration pulse ends. The deflection pulse has an absolute value of the electric field of 320.3 V/cm ($U_1 = 750$ V) and a duration of 1 $\mu$s. For the determination of the ionisation threshold (see chapter 6), the absolute value of the ionisation field is important. In contrast to the excitation of the Rydberg atoms, where the laser sets the excitation volume along the horizontal axis, we also have to consider the homogeneity $H$ along the z-axis. The homogeneity of the ionisation field is shown

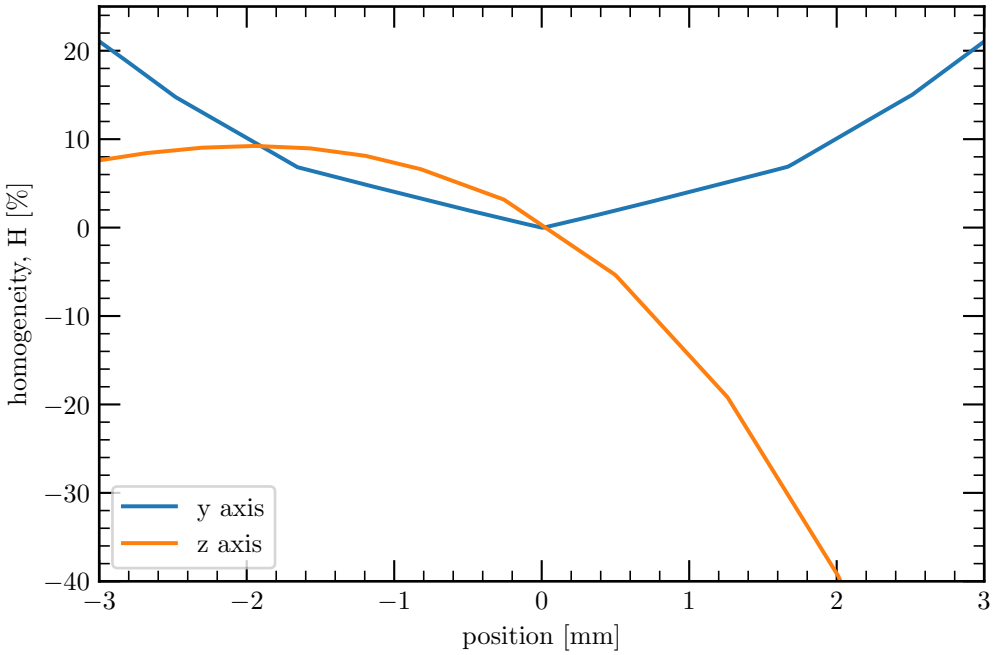


**Figure 3.13.:** *Analysis of the homogeneity of the ionisation field generated by the electrodes. The voltage at the ring segments $U_1$,...,$U_4$ can be taken from the table 3.1. The plate electrode is set to the maximal ionisation voltage of* 450 V*. The homogeneity of the field changes by* 10% *on the horizontal y-axis in the* 2 mm *surrounding of the MOT position. The electric field reduces by 40% on z-axis within a distance* 2 mm *from the predicted MOT position.*

in figure 3.13. The blue line shows the homogeneity $H$ along the horizontal axis and the orange line along the z-axis. In the 2 mm surrounding of the MOT position, the homogeneity of the ionisation field changes on the horizontal axis by 10% and on the z-axis up to 40%, with increasing distance to the plate electrode (see figure 3.10). This analysis yields that the position along the z-axis has the biggest influence on the absolute value of the electric field and will therefore dominate the error of the ionisation threshold.

## 3.3. Measurement techniques

For a detailed study of the Yb Rydberg atoms we have to measure several quantities. For the depletion spectroscopy for example we have to measure the population of the cold

atoms inside the trap. To calculate this quantity we measure the fluorescence light from the MOT. Section 3.3.1 contains a brief description of the imaging system for spectroscopy. A detailed discussion of the depletion spectroscopy measurement can be found in chapter 4. To directly detect the Rydberg atoms we measure the Yb ions with a MCP. The ions are created by a high voltage pulse, which ionizes the Rydberg atoms (see chapter 6 and 3.2.5). The functionality of a MCP and the detection respectively the counting of the ions is described in section 3.3.2.

To record all the data we use a software network of several client programs, which send their data to a central data server. This server combines the data and stores them in a data base. The data acquisition network and the control program, that executes the time sequence is described in section 3.3.3.

### 3.3.1. Fluorescence measurement

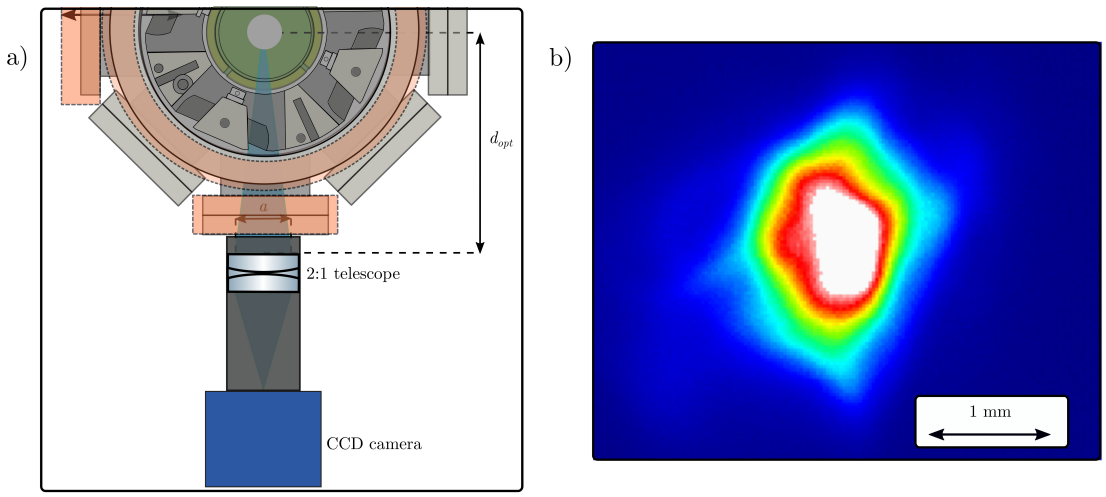


**Figure 3.14.:** *a) Fluorescence imaging System. The distance between the MOT and the telescope is* $d_{opt} = 21.4\,\mathrm{cm}$. *The aperture of the telescope is* $a = 25.4\,\mathrm{mm}$. *b) Fluorescence image of the MOT with an exposure time of* $300\,\mu\mathrm{s}$, *in false colors.*

The fluorescence of the MOT is measured by a CCD camera. With the images, that the CCD camera[3] takes from the MOT (see figure 3.14 b)) several quantities of the MOT can be determined. It is possible to calculate the population, the size, the density and the position of the trap (see section 3.4). The fluorescence measurement is also fundamental

[3]Company: ABS GmbH Jena; Typ: UK1117-M

for the MOT depletion method (see section 4.1), which we use for the spectroscopy study of the Rydberg states.

The setup for the imaging system is shown in figure 3.14 a). The camera is attended to an optical sealed 2:1 telescope. The distance from the telescope to the MOT position is $d_{opt} = 21.4\,\text{cm}$ and the aperture of the telescope is $a = 25.4\,\text{mm}$. The technical data of the CCD are:

- pixel size: $8.3 \times 8.3\,\mu\text{m}$
- chip size: $640 \times 480$
- delay between trigger and the start of the exposure: $3200\,\mu\text{s}$
- minimal exposure time: $50\,\mu\text{s}$

The camera is triggered directly with a TTL signal from the National Instrument card, which controls the entire experiment (detail view 3.17). A LabView program is recording the images of the CCD camera and stores them in a data base. Python and Matlab programs are used to evaluate these images in order to determine the quantities, such as the atom number, size, density and position of the MOT. The LabView program also records the pixel-sum of the MOT image, which is used for the MOT depletion spectroscopy (see section 4.1).

### 3.3.2. Ion detection

For the direct detection of the Rydberg atoms we use the electric field ionisation method. Thereby the Rydberg atoms are ionized with a fast electric field pulse (see reference [1]). The ions created in this way are then guided to a MCP, with the help of additional electric fields (see section 3.2.5).

The setup of the MCP inside the vacuum chamber is shown in figure 3.8. The distance between the MOT and the MCP is $\approx 10\,\text{cm}$. The MCP has two stages and is shown in detail in figure 3.15 b). The channel diameter is $12\,\mu\text{m}$ and the input electrode has an effective diameter of 20 mm. The input electrode is held on a potential of $-2.5\,\text{kV}$ and the anode is at ground potential. A detailed electronic circuit including the signal processing unit can be found in figure A.1 in the appendix. The cold Yb atoms are shielded from the high MCP potential, by a self-built wire mesh, made of steel. The mesh has a distance of

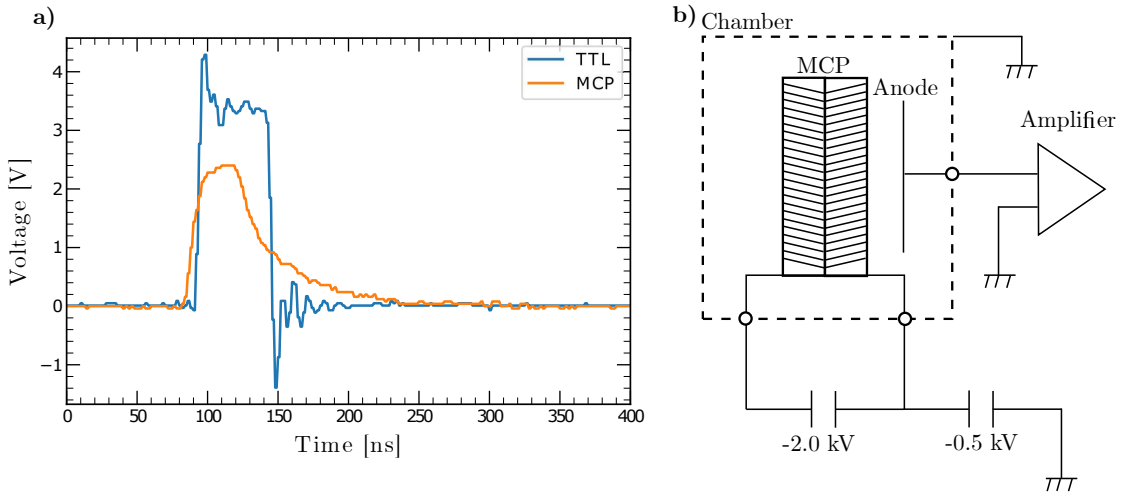


**Figure 3.15.:** ***a)*** *Typical ion signal from the MCP and the corresponding TTL conversion from the signal processing unit.* ***b)*** *Wiring diagram of the MCP including the amplifier.*

5 cm from the atoms and the potential of the mesh can be adjusted to optimize the ion collection efficiency.

The MCP is directly connected to an instrumentation amplifier, that amplifies the signal by a factor of 2 (a typical ion signal at the output of the instrumentation amplifier is shown in figure 3.15 a)). After the initial amplification, the signal is processed by a discriminator, with an ECL (emitter-coupled logic) output level. The discriminator is followed by a fast frequency divider and a 12 bit counter integrated circuit (IC). The output of this circuit is converted to the TTL level and detected by an arduino. With this setup it is possible to count individual events with 13 ns resolution, limited by the 12 bit counter.

With the arduino it is also possible to implement a gate for the measurement, to filter out false events. These false events are for example created by spurious signals due to the high voltage pulses, which are applied to the electrodes (see section 3.2). The typical gate for the ion measurements in this thesis, starts 5 $\mu$s after the high voltage pulse and lasts for 50 $\mu$s. This delay of the gate is sufficient for separating false from true events because the time of flight from the ions to the MCP is larger than 5 $\mu$s. The arduino counts the events detected by the MCP and the high voltage pulses and transfers the information via USB to a data grabber program, that itself transmits the information to a server. A detailed description of the data acquisition and computer control is given in section 3.3.3. The limitation of this counting method is set by the number of events that can be counted in one cycle as

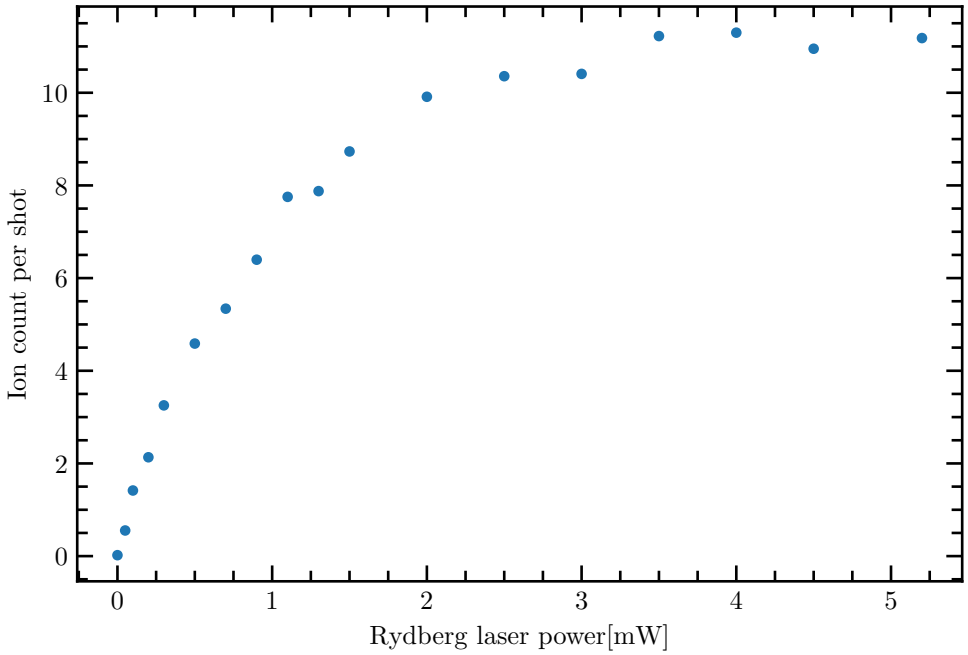


**Figure 3.16.:** *Ion counts per experiment cycle. The Rydberg beam pulse has a duration of* 500 ns *and it is focused onto the MOT with a beam waist of* 110 $\mu$m*. The maximal count of 11 ions per cycle is limited by the time resolution of the counter unit and the simultaneity of the ion events.*

is shown in figure 3.16. There, the ion count per experiment cycle as a function of to the power of the Rydberg laser is shown. It exhibits a saturation behavior with a maximal count number of around 11 counts. The saturation is caused by the time resolution of the counting unit and simultaneity of the ion events, if large numbers of Rydberg atoms are produced at higher laser power. Since the saturation behavior falsifies the actual counting rate, the power of the Rydberg beam must be adjusted for each measurement such that no saturation occurs.

### 3.3.3. Control and Acquisition

The experiment has a high level of automation. It is controlled by a GUI-based control system called "Cicero Word Generator" [66], that makes use of a client-server separation. With the client we design the time sequence of our experiment. For an example of a control

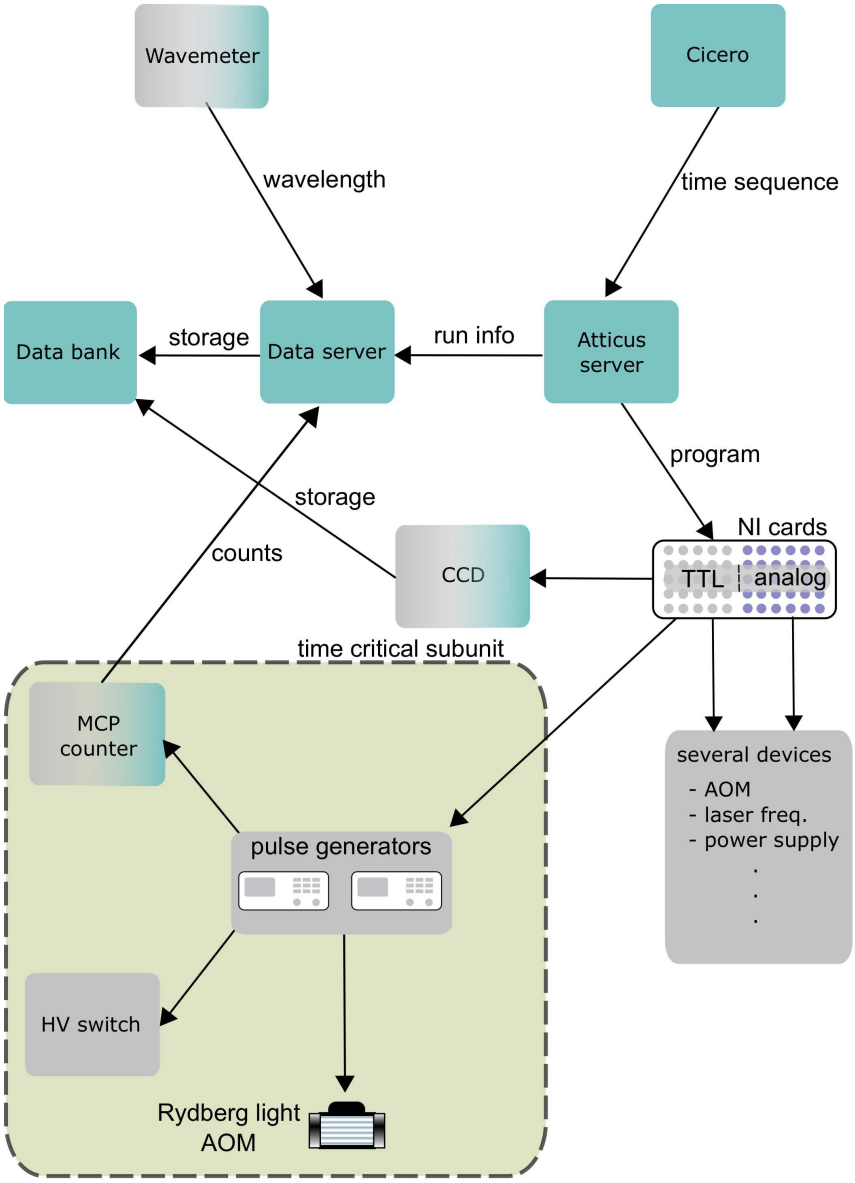


**Figure 3.17.:** *Sketch of the data acquisition and control network of the apparatus. Grey boxes are devices. Blue boxes are computer programs . Multi color boxes are devices with a program interface.*

sequence see figure 3.18. The server programs two multi function I/O cards[4]. These two cards have in total 32 analogue and 32 digital output channels to control the experiment.

The I/O cards have a maximum time resolution of 50 ns, which is more than sufficient for the standard control of the experiment. However, for the fast dynamics of the Rydberg atoms we need a sub-unit, that controls the time critical components, such as the high

[4]Company: National Instrument (NI); Typ: PCI-6229, PCI 6723


**Figure 3.18.:** *Typical time sequence of the experiment, programmed in Cicero [66]. The columns represent the time steps of a control sequence. Each time step has a fixed length and can be enabled or disabled separately. For each time step the output of the digital channels (lower rows) and of the analog channels (upper rows) can be separately adjusted. In the sequence shown the MOT is first loaded and then radiated by the Rydberg laser. After the Rydberg laser pulse an electric field pulse is generated by the electrodes. After 128 repetitions of laser light and electric field pulse a picture of the MOT is taken.*

voltage pulse switch or the AOM for the Rydberg light pulse. This sub-unit consists of two commercial pulse generators[5] with a channel to channel time jitter of 50 ps and a time resolution of 5 ps.

A detailed scheme of the control and data acquisition network is shown in figure 3.17. In this network several devices transmit their data via clients to a central data server, which combines the data and stores them in a data bank. Both the client and the sever are python based and use the socket module for communication. The acquisition devices are the self-built Michelson-Morley wavemeter [67], the self-built arduino based counter electronic (see section 3.3.2) and the CCD camera.

[5] Company: Stanford research systems; Typ: DG535

## 3.4. Ytterbium MOT

The cold Yb gas, in which the Rydberg atoms are created is produced in a MOT. This MOT is loaded from an atomic beam, that is slowed by a Zeeman slower. The Zeeman slower has an increasing magnetic field geometry to compensate the Doppler shift during the slowing process. In the MOT, three pairs of counter propagating laser beams, which intercept inside the experimental chamber, produce a frictional force in all three spatial dimensions. Together with a quadrupole magnetic field and the circular polarisation, the laser lights forms the magneto optical trap. A brief introduction into the principle of laser cooling and trapping of neutral atoms can be found in section 2.1 and in the reference [46]. The setup used to generate the Yb MOT in the experiment was build by Bastian Schepers in the context of his master thesis [63].

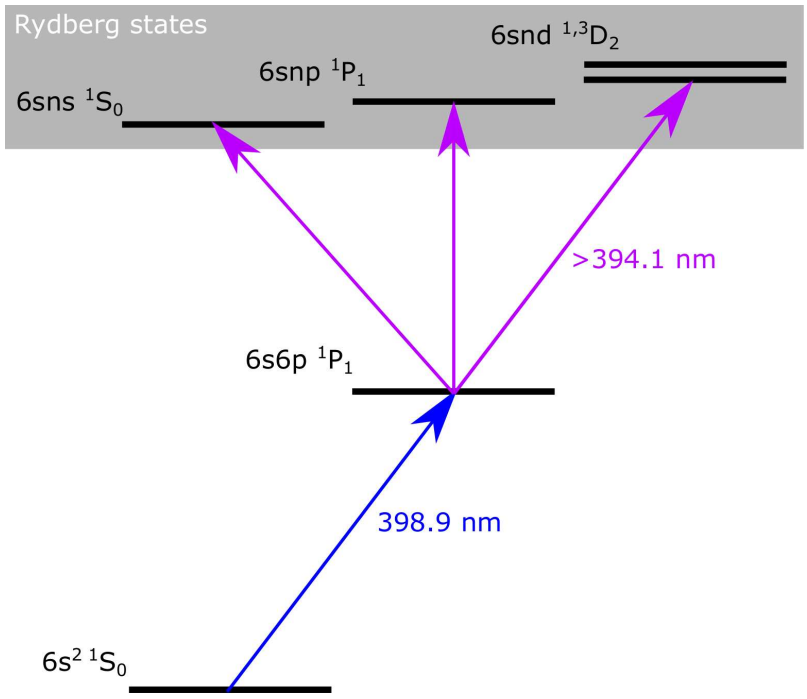


**Figure 3.19.:** *Energy level structure of Yb. The transition* $6s^2\,{}^1S_0 \rightarrow 6s6p\,{}^1P_1$ *with a wavelength of* 398.9 nm*, is used for the cooling transition of the MOT and also as an intermediate state for the Rydberg excitation into S-,P- and D- states. The excitation into the* $6snp\,{}^1P_1$ *series is dipole forbidden, but due to state mixing in an external electric field it is possible to excite these states from the* $6s6p\,{}^1P_1$ *sate. The minimal wavelength for the Rydberg excitation is* 394.1 nm *corresponding to the ionisation threshold.*

Yb is a rare earth element and has 7 stable isotope, 2 are fermions and 5 are bosons.

All measurements in this thesis are done with $^{174}Yb$, the most common isotope with an abundance of 31.8%.

Due to the lack of a nuclear spin and thus a hyperfine splitting in the ground state of the bosonic iostopes, the relevant energy level structure (see 3.19) is quite simple. The cycling transition at 399 nm from $6s^2\,{}^1S_0 \rightarrow 6s6p\,{}^1P_1$ is used for the Zeeman slower and the MOT. The laser system that provides the required wavelengths is described in section 3.5.1.

The MOT operates on the same transition as Zeeman slower ($6s^2\,{}^1S_0 \rightarrow 6s6p\,{}^1P_1$), with an adjustable red detuning between 10 and 30 MHz. The Zeeman slower has a red detuning of 500 MHz. The horizontal width of the MOT beams is 5 mm and the vertical width is 3 mm. The Zeeman slower laser beam is focused on the aperture of the oven. The oven, which produces the atomic beam, is heated to a temperature of 420 °C. To measure the size and atom number of the cold cloud, we record the fluorescence of the atoms with a CCD camera (see also section 3.3.1).

### 3.4.1. Size and atom number of the MOT

With the fluorescence measurement of the $6s6p\,{}^1P_1 \rightarrow 6s^2\,{}^1S_0$ transition, it is possible to measure the size of the MOT and the number of atoms in the ${}^1P_1$ state. To determine the size of the trap the magnification of $m = 0.5$ of the imaging system has to be considered. Assuming a two dimensional Gaussian distribution of the atom cloud,

$$f_{2D}(x,z) \quad = \quad A_{2D} \cdot \exp\left(-\frac{x^2}{2\sigma_x^2} - \frac{z^2}{2\sigma_z^2}\right), \tag{3.34}$$

a fit to the fluorescence image yields a typical MOT size of $\sigma_{y,z} = 1000\,\mu$m. Here $A$ is the maximal pixel value of a MOT image. For determination of the atom number inside the trap, we now assume equal sizes of the cloud in the x and y direction ($\sigma_x = \sigma_y$). The distribution of the atom cloud can then be described as

$$f_{3D}(x,y,z) \quad = \quad A_{3D} \cdot \exp\left(-\frac{x^2}{2\sigma_x^2} - \frac{y^2}{2\sigma_y^2} - \frac{z^2}{2\sigma_z^2}\right). \tag{3.35}$$

Where $A_{3D}$ is related to $A_{2D}$ via the integral

$$f_{2D}(x,z) \quad = \quad \int_{-\infty}^{\infty} f_{3D}(x,y,z)dy = \underbrace{A_{3D} \cdot \sqrt{2\pi} \cdot \sigma_y}_{A_{2D}} \cdot \exp\left(-\frac{x^2}{2\sigma_x^2} - \frac{z^2}{2\sigma_z^2}\right). \tag{3.36}$$

The digital CCD signal $N_{cam}$ that is proportional to the number of atoms inside the MOT is given by,

$$N_{cam} = (2\pi)^{3/2} \cdot A_{3D} \cdot \sigma_x \cdot \sigma_y \cdot \sigma_z. \tag{3.37}$$

For the conversion of the camera signal to a real atom number, several quantities have to be considered. Only a small fraction of the scattered light is entering the image system. This is described by the solid angle factor $a_{ang}$, which is given by,

$$a_{ang} = \frac{a}{4 \cdot d_{opt}} \tag{3.38}$$

Where $a$ is the aperture of the image system and $d_{opt}$ is the distance between the MOT and the image system. Also the absorption of all optical components reduces the amount of photons reaching the CCD chip. This reduction is expressed by the absorption factor $a_{abs}$. The CCD chip counts the photons and creates a digital signal where the value is proportional to the photon number via the camera specific quantum efficiency $a_{CCD}$. This leads to the following expression for the amount of emitted photons from the atom cloud $N_{ph}$

$$N_{cam} = a_{CCD} \cdot a_{abs} \cdot a_{ang} \cdot N_{ph} = a_{tot} \cdot N_{ph} \tag{3.39}$$

The maximum number of photons scattered by the atom cloud during the exposure time $t_{exp}$ is given by,

$$N_{ph} = N \cdot \gamma \cdot t_{exp} \tag{3.40}$$

Where $\gamma$ is the natural line width of the MOT transition and $N$ the number of excited atoms inside the MOT. From this follows for the atom number the following expression:

$$N = \frac{N_{cam}}{\gamma \cdot a_{tot} \cdot t_{exp}} \tag{3.41}$$

Considering all those parameters the analysis of fluorescence data yields a typical atom number of $N \approx 1 \times 10^7$ in the $^1P_1$ state. The atom number in the cloud depends on a variety of different parameters. This includes the detuning of the MOT beams, the magnetic field gradient, the size and power of the MOT beams, the temperature of the Yb oven and

the pressure inside the vacuum chamber. All theses parameters have to be optimized for on an optimal performance of the MOT.

### 3.4.2. Lifetime

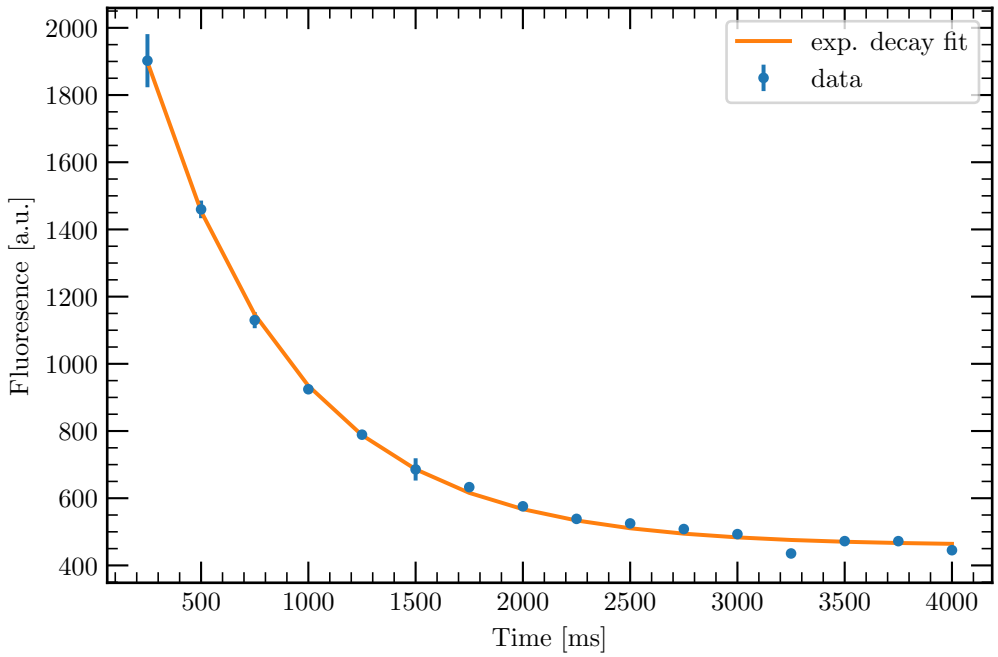


**Figure 3.20.:** *Lifetime of the MOT. The exponential fit yields a a lifetime of* $\tau = 677 \pm 17\,\mathrm{ms}$

By switching off the slower beam a "lifetime" of the MOT can be measured. Thereby the fluorescence of the atom cloud is measured as a function of time, after the slower and thus the MOT loading was switched off. As can be seen in figure 3.20 the fluorescence decays exponentially with a typical lifetime of the MOT is $\tau = 677 \pm 17\,\mathrm{ms}$. The lifetime is limited because the cooling transition $6s6p\ ^1P_1 \rightarrow 6s^2\ ^1S_0$ is not radiatively closed. Some off the excited atoms decay into meta-stable states and are therefore lost from the MOT. The atoms decay into the meta-stable triplet states $^3P_{2,0}$, via the $6s6p\ ^1P_1 \rightarrow 5d6s\ ^2D_{2,1}$ transition [68][69]. The decay to the meta-stable states depends on the excitation level of the MOT, which can be controlled by the trap-beam power [70]. Another limiting factor

for the lifetime of the MOT could be the collision of cold atom cloud with hot background gas. But the measured lifetime lies well below the expected background-gas limited lifetime of several 10 seconds [71].

### 3.4.3. Temperature

One way to measure the MOT temperature is the release-recapture method [48]. In this method the cold atom cloud is released from the trap by switching of the MOT beams. Subsequently the MOT beams are turned off again after a time interval $\Delta t$ and the atoms are recaptured. The fraction of atoms $f_R$, which are recaptured is directly correlated to the temperature of the atom cloud. If the cloud is allowed to expand homogeneously with a Gaussian velocity distribution the fraction of atoms $f_R$ after a release time $\Delta t$ is given by [48],

$$f_R = \frac{1}{\pi^{3/2}} \int_0^{v_c/v_t} e^{-u^2} 4\pi u^2 \, du \tag{3.42}$$

Where the thermal velocity $v_t = \sqrt{2k_BT/m}$ and the critical velocity $v_c = R_c/\Delta t$. The critical velocity is defined by the radius $R_c$, which marks the recapture volume of the MOT. The integration of equation 3.42 yields the following relation between the fraction of atoms, the recapture time $\Delta t$ and the temperature $T$ [48]:

$$f_R = -\frac{2R_c}{\sqrt{2\pi k_BT/m}\Delta t} \exp\left(\frac{R_c^2 m}{2k_BT\Delta t^2}\right) + \mathrm{Erf}\left(\frac{R_c}{\Delta t\sqrt{2k_BT/m}}\right) \tag{3.43}$$

A typical example for a fit of equation 3.43 to the measured recaptured fraction of the atoms is shown in figure 3.21. The radius of the recapture volume is estimated with $R_c = 1.5\,\mathrm{mm}$. The recapture volume is influenced by the size of the MOT beams and the magnetic field gradient and is therefore the quantity with greatest uncertainty. A small change of the recapture radius $R_c$ causes a shift in the order of the error of the determined temperature. At a MOT beam power of 15 mW and a MOT detuning of 15 MHz the fit yields a MOT temperature of $3.8 \pm 1.1\,\mathrm{mK}$. This temperature is hotter than the Doppler cooling limit of 0.69 mK. Even at very low MOT beam intensities, measurements showed, that this limit can't be reached because of other heating mechanisms, caused possibly by standing wave effects [72].

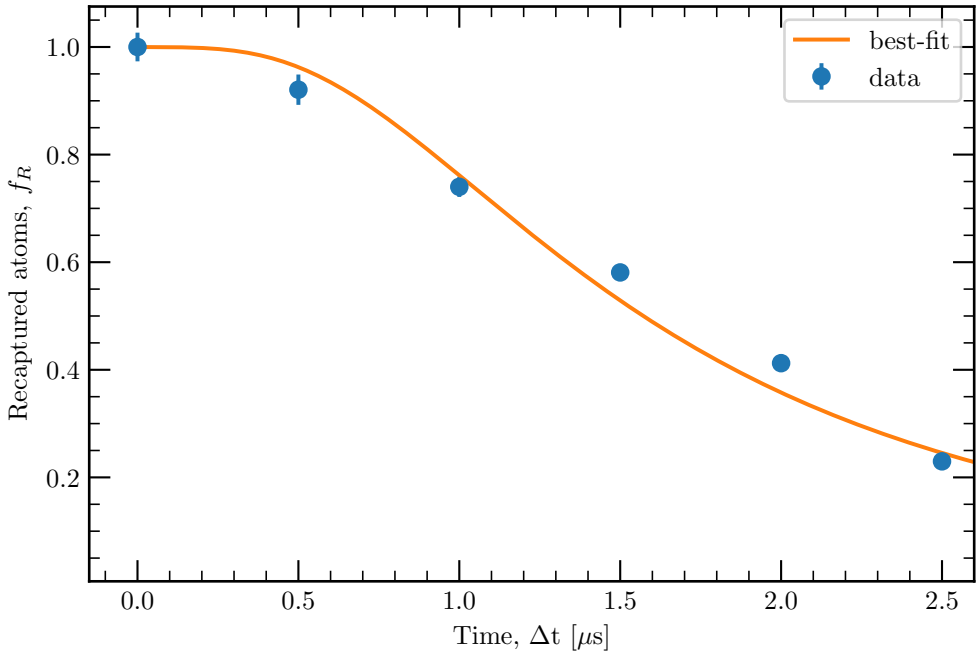


**Figure 3.21.:** *Release-recapture measurement for the determination of atom cloud temperature. The fit of equation 3.43 with a fixed recapture radius of* $R_c = 1.5\,\mathrm{mm}$*, yields a temperature of* $T = 3.8 \pm 1.1\,\mathrm{mK}$.

### 3.4.4. Density of the MOT and Rydberg-Rydberg interaction

Another important property of the MOT is the atom density. It defines the distance between the atoms and therefore the interaction between them. The density is derived from the size of the MOT and the number of atoms inside the trap.

$$\rho_{max} = \frac{N}{2\pi^{3/2} \cdot \sigma_x \cdot \sigma_y \cdot \sigma_z} \tag{3.44}$$

Assuming a Gaussian distribution, the above-mentioned atomic number and MOT size result in an atom peak density of $\rho_{max} \approx 9 \times 10^8\,\mathrm{cm}^{-3}$. Therefore the mean interatomic distance is $R_{min} \approx 10\mu m$. As shown in section 2.4 the pair interaction between two Rydberg atoms for such an interatomic distance leads to no significant shift of the energy levels of the Rydberg states. The density of the MOT is therefore not high enough to observe interactions between the Rydberg atoms, like the dipole blockade [73]. However, a MOT based on the

inter-combination transition ${}^1S_0 \rightarrow {}^3P_1$ would have up to two orders of magnitude higher density [69], which is dense enough to observe Rydberg-Rydberg interactions between the Yb atoms. Therefore, we will implement such a "green" MOT laser at 556 nm for future experiments.

## 3.5. Laser systems

In this section, the setup of the two laser systems of the apparatus is described. The first laser system provides the laser light for the MOT beams and the slower beam. Both operate on the $6s^2\ {}^1S_0 \rightarrow 6s6p\ {}^1P_1$ transition with a wavelength of $\lambda_{M,S} = 399\,\text{nm}$. The second laser system generates laser light for the excitation into the Rydberg states via the $6s6p\,{}^1P_1$ MOT state. The wavelength for the transition from the $6s6p\,{}^1P_1$ state to the Rydberg states is approximately $\lambda_R = 394\,\text{nm}$, depending on the specific Rydberg state. The energy level scheme with excitation path into the Rydberg states is shown in figure 3.19.

### 3.5.1. MOT laser system

The laser system for the blue MOT and the slower consists of two laser diodes in master-slave configuration and is shown in figure 3.22.

The master laser [6], with a small frequency bandwidth of a few 100 kHz, is stabilized to a Yb spectroscopy. For this purpose the laser light is frequency modulated with an acousto-optical modulator (AOM) (see figure 3.22 AOM 1). To minimize the intensity modulation of the spectroscopy signal through spatial modulation of laser light caused by the AOM, the laser passes the AOM in a double-pass configuration. The error signal, for the frequency stabilization, is generated by the demodulation of the spectroscopy signal using a lock-in technique.

The light from the master diode is used for the Zeeman slower (2 mW) and for injection of the slave diode[7]. AOM 2 is used for a first frequency shift of the laser light from the master diode before it gets injected into the slave diode.

The laser light from the slave diode (20 mW) passes through AOM 3, which is used for power adjustment, frequency control and fast switching of the MOT light.

[6] Company: Nichia; Typ: NDHV310ACAEI; Wavelength: 399 nm; Output 10 mW
[7] Company: Nichia; Typ: NDV4313E; Wavelength: 400 nm; Output 50 mW

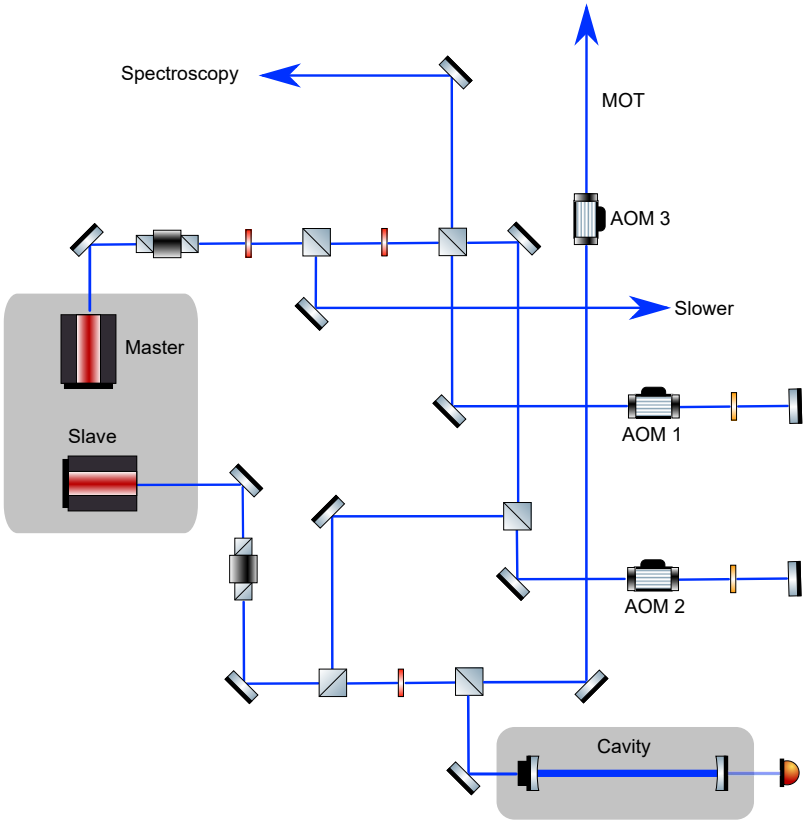


**Figure 3.22.:** *Sketch of the laser system for the operation of the MOT. The light of the master laser is split in three path. One path is for the frequency stabilisation, which is done using a spectroscopic method. The other path is used for the Zeeman slower and the last one injects a slave diode. The laser light of the Slave diode is used for the MOT.*

### 3.5.2. Rydberg excitation Laser

The excitation of the Yb atoms into Rydberg states is done via the intermediate $6s6p\,^1P_1$ state, which is also the excited state of the MOT and the Zeeman slower. The energy pathway of the excitation, is shown in figure 3.19. The first photon for the transition into the intermediate state is provided by the MOT beams. For the second transition from the intermediate state to Rydberg states we need a photon with an energy, that corresponds to a wavelength of approximately 394 nm and higher, depending on the specific state.

To obtain these wavelengths with a suitable amount of power of a few milliwatts, we use the laser system shown in figure 3.23. In this system a commercial grating-stabilized diode laser[8] is amplified to 500 mW output power, by a taperd amplifier[9]. After the amplification,

[8] Company: Toptica; Typ: DLPro; Wavelength: 780 nm
[9] Company: m2k-laser GmbH; Typ: m2k-TA-0780-2000

the laser light is frequency doubled in a home-build resonant Bow-Tie cavity [74], with a lithium triborate crystal (LBO). The cavity length is locked using a Hänsch-Couillaud [75] locking-scheme. The maximum output power of the frequency doubling cavity is 20 mW at 394 nm.

Before the laser light for the Rydberg excitation is guided to the experimental chamber via an optical fiber, it passes an AOM. Both the AOM and optical fibre reduces the output power of the laser system by factor of 2, which finally corresponds to a maximum output power of 5 mW at the experiment chamber. The fast switching of the AOM enables light pulses with a minimum duration of $10 - 100$ ns. for a defined excitation of the Rydberg states, the light is then focused onto the MOT with a beam waist of 100 $\mu$m.

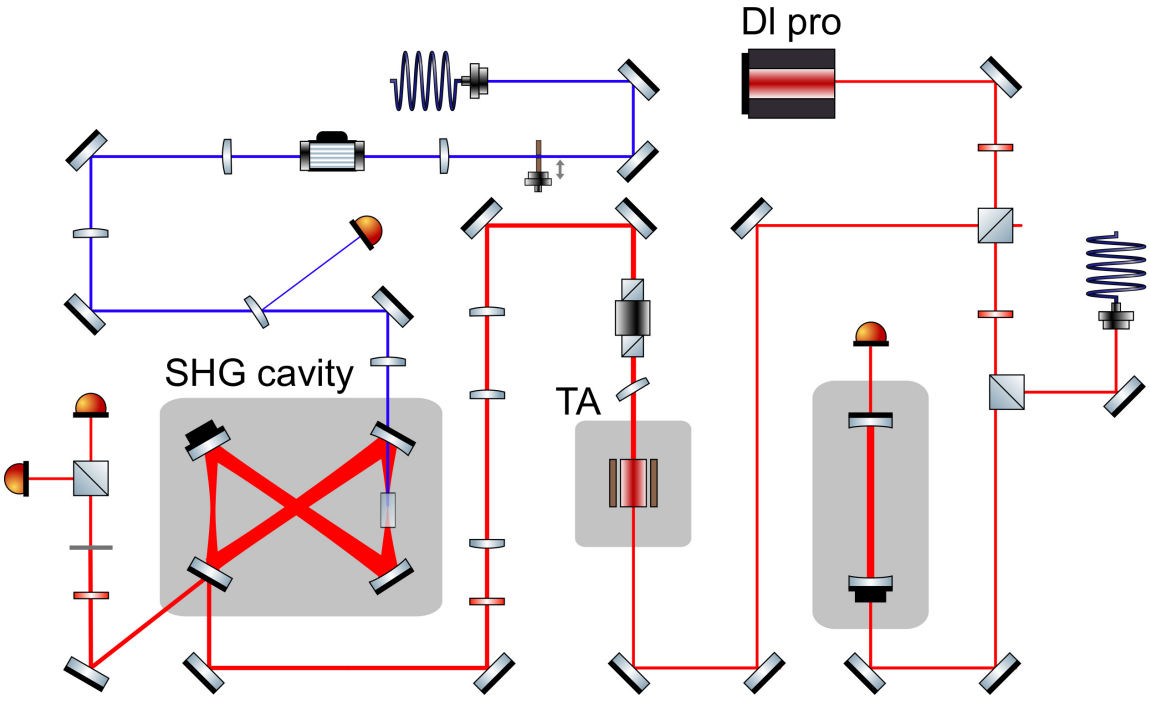


**Figure 3.23.:** *Sketch of the laser system, used for the excitation into the Rydberg states. The laserlight of the commercial laser (Toptica Dl pro) is amplified by tapered amplifier (m2k-TA-0780-2000) to a maximal output power of* 1 W. *The output of the tapered amplifier is frequency doubled in a cavity using a LBO crystal. The resulting wavelength is close to the ionisation threshold of* 394.1 nm *and has an output power of up to* 20 mW.

# 4.

# Spectroscopy of Rydberg S- and P-states

The level structure of a specific atom species is the basis for the investigation of Rydberg physics. Here we present a straight forward method for measuring the energy levels of several Rydberg series in a cold gas of ytterbium. The basic theory of Rydberg energy levels was already summarised in chapter 2.2, where the quantum defect and the multi channel quantum defect theory were introduced. In this chapter the results from the spectroscopy measurements are compared with previous studies of the ytterbium Rydberg states [7, 76].

## 4.1. Experimental procedure

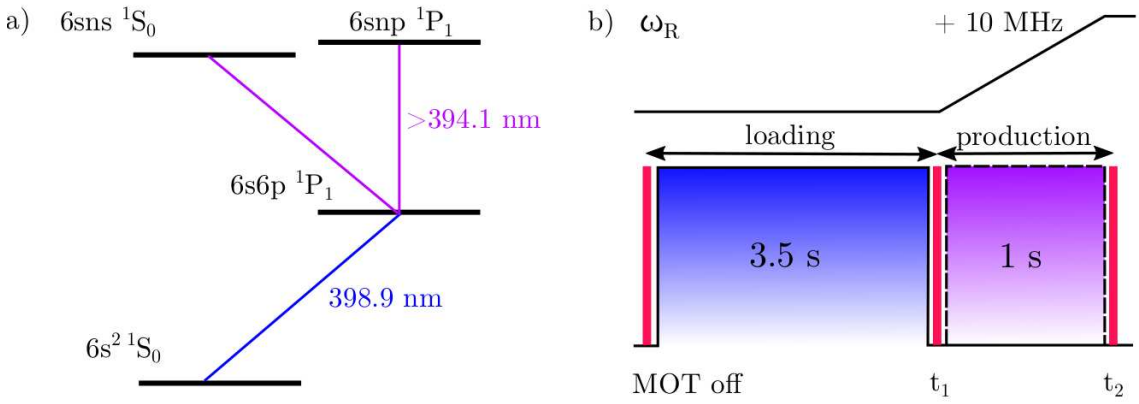


**Figure 4.1.:** *a) Excitation pathway to the Rydberg states over the intermediate state $6s6p\,^1P_1$, which is also used for the MOT. b) Time sequence for the step scan technique. At time $t_1$ a picture of the MOT is taken followed by the radiation of the Rydberg laser. At time $t_2$ another picture is taken to determine the remaining atoms inside the MOT. During the radiation the frequency $\omega_R$ of the Rydberg laser is changed by* 10 MHz.

Rydberg atoms are produced using a two photon excitation $h\nu_{Ryd} = h\nu_{MOT} + h\nu_{Ryd.laser}$, as illustrated in figure 4.1 a). The first transition $6s^2\ ^1S_0 \rightarrow 6s6p\ ^1P_1$ is already provided by the light $\lambda_{MOT} = 389.9\,\text{nm}$ from the MOT itself. The second step in the excitation is provided by the laser system described in chapter 3.5.2. The laser has a minimal wavelength of 394.1 nm and a maximal power of 5 mW inside the experiment chamber. The laser is focussed into the MOT region with a focus radius of 110 $\mu$m. In this study the Rydberg atoms are detected indirect by measuring the remaining atoms in the MOT. This method is called depletion spectroscopy and was performed with the setup from the first stage of the experiment described in chapter 3.1.

The sequence that we use for the depletion Spectroscopy of the Rydberg states is illustrated in figure 4.1 b).

1. To wipe out any remaining atoms from the trap the MOT light is turned off for 100 ms.
2. The MOT is turned on and loaded for 3.5 s, to get a reproducible number of atoms (loading interval).
3. The slower is turned off, the MOT starts to deplete.
4. The fluorescence of the MOT is measured to get the number of atoms inside the trap.
5. The Rydberg laser is turned on, introducing an additional loss of atoms inside the MOT (production interval).
6. After 1 s radiation time of the Rydberg laser the fluorescence of the trap is measured again. During the radiation time, the frequency $\omega_R$ of the Rydberg laser is changed linearly by a small frequency interval of 10 MHz.

Every fifth cycle is used as a calibration shot. In this shot the Rydberg laser is not turned on and the frequency of the laser is not changed. With this calibration it is possible to cancel out the long-time fluctuations of the fluorescence and it is possible to normalize our measurement to the loss, which is caused by turning off the slower light. Typical raw data is shown in figure 4.2.

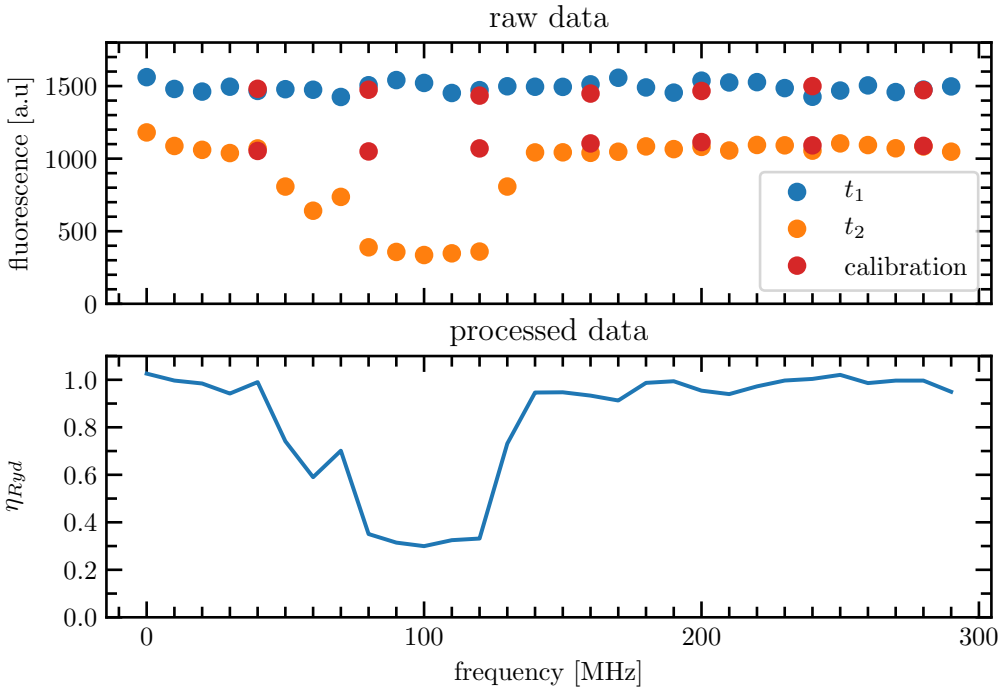


**Figure 4.2.:** *Raw and processed data from the 80 $^1S_0$ state. The data is taken with the first setup of the experiment with 3 V applied to the electrode. The Upper graph shows the raw data. Blue dots are the fluorescence taken at time $t_1$. The orange dots are measured at time $t_2$. The red dots are the calibration shots, where the frequency shift and the Rydberg laser are turned off. The lower graph shows the processed data of the scan, according to equation 4.1.*

The relative intensity $\eta_{Ryd}$, that is caused by the Rydberg excitation is given by:

$$\eta_{Ryd} = \frac{I_{Ryd}}{I_{MOT} \cdot r_{cal}}, \tag{4.1}$$

where $I_{Ryd}$ is the fluorescence of the trap after production interval (at time $t_2$ in the cycle). $I_{MOT}$ is the fluorescence after the loading interval (at time $t_1$) and $r_{cal}$ is the normalization factor derived from the calibration shots. For the normalization a polynomial function of the 3rd order is fitted to the relative intensity of the calibration shots. The relative intensity of one calibration shot is given by,

$$\eta_{calibration} = \frac{I_{t_2}}{I_{t_1}}. \tag{4.2}$$

Where $I_{t_2}$ is the fluorescence after the production interval without a Rydberg laser and

$I_{t_1}$ is the fluorescence of the MOT after the loading interval. The calibration factor $r_{cal}$ is determined by a fit to the relative intensity of the calibration shots $\eta_{calibration}$ and their time stamp during the complete scan. Therefore the calibration factor is given by,

$$r_{cal}(t_{cycle}) = c_1 \cdot t_{cycle} + c_2 \cdot t_{cycle}^2 + c_3 \cdot t_{cycle}^3. \tag{4.3}$$

Where $c_1$,$c_2$ and $c_3$ are the fit parameters and the time $t_{cycle}$ is the time of the cycle during a complete scan. With this fit it is possible to interpolate the loss, caused by turning off the slower, for every shot in the run. It is also possible to determine the long time fluctuations of the atom number inside the MOT, which is caused by a shift of the MOT laser frequency. Both factors are canceled out of the data by the normalization.

To determine the binding energies of the Rydberg states we measure the wavelength $\lambda_R$ of the Rydberg excitation laser with a self-built Michelson-Morley wavemeter over the complete run. With a linear fit function it is possible to determine the wavelength of every cycle of the corresponding run. The estimated absolute frequency error of this method is 150 MHz ([77]). With this step scan technique it is possible to scan over a Rydberg transition. But to determine the binding energy of a Rydberg state precisely we measure a complete Stark map of the state.

A standard method to measure the energy level and the polarizability of a Rydberg state precisely is measure the dependency of the binding energy on an external electric field and determine its value for vanishing of the total electric field. Therefore the strength of the background electric field is varied and the transition is shifted by the Stark effect, see section 2.3.1. A graph which shows the binding (or excitation) energy as a function of electric field is thus often referred to a Stark map. The energy of the Rydberg state shifts quadratic with the electric field according to,

$$\Delta E = \frac{1}{2}\alpha_0 \cdot F^2, \tag{4.4}$$

where F is the amount of the electric field and $\alpha_0$ is the polarizability of the state. By fitting a quadratic function

$$E = E_0 + E_1 \cdot F + E_2 \cdot F^2 \tag{4.5}$$

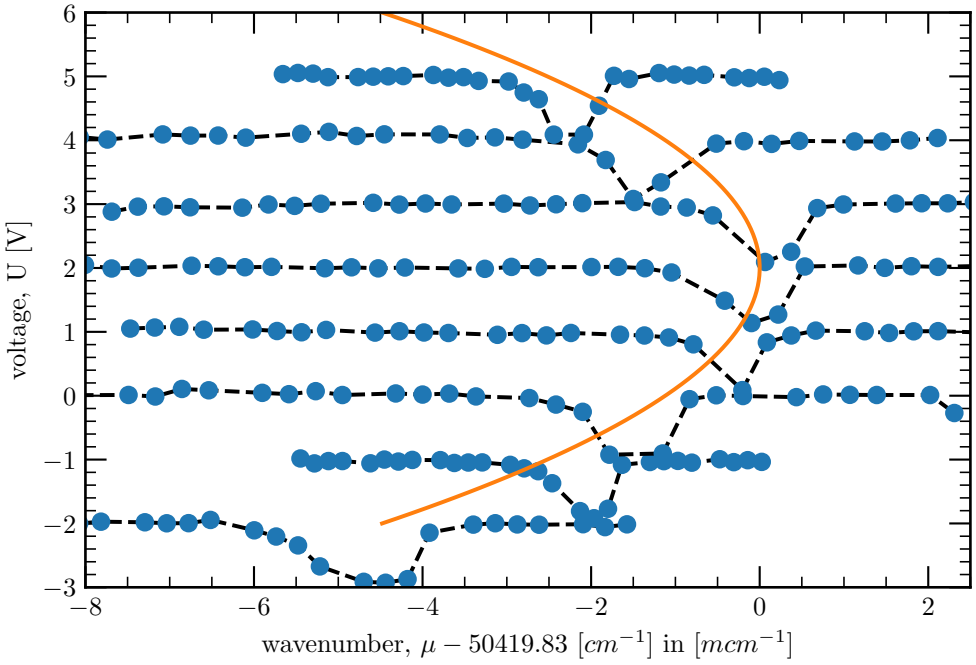


**Figure 4.3.:** *Stark map of the $6s73s\ ^1S_0$ state. The shift of the transition is shown as a function of voltage applied to the top window electrode of the first stage of the experiment. There is no electric field conversion because of an insufficient control of the absolute value of the electric field simulation of the first setup. Blue dots are scans of the transition, made with the step scan technique. The black dashed lines are plotted to guide the eye. The red solid line is a quadratic fit to the center position of the Gaussian fits. From the wavenumber corresponding to the excitation energy a value of* $50420.496\,\mathrm{cm}^{-1}$ *is subtracted to show the Stark shift more directly.*

to the energy of the transitions, the Stark map is generated (see figure 4.3) . The vertex $E_0$ is thereby the unperturbed energy level of the state and the polarizability is given by $\alpha_0 = -2 \cdot E_2$. The advantages of this method are, that it determines the energy level and the polarizability of the Rydberg state at the same time. Because the electric field mixes the Rydberg states, it is also possible to measure the actually forbidden transitions such as the $6s6p\ ^1P_1 \rightarrow 6snp\ ^1P_1$ transition. By varying the electric field, the method also ensures that an electric background field is cancelled out by the measurement. In figure 4.3 the energy level of the Rydberg transition is shown in units of wavenumber, which is a common way to express the energy level of states. Another way to express the energy is in the unit of frequency, which is mostly used to show the spacing of the Rydberg states. The relation

between the frequency $\nu$, wavenumber $\mu$ and energy $E$ of the state is given by,

$$\mu = \frac{\nu}{c} = \frac{1}{\lambda} = \frac{E}{hc}, \tag{4.6}$$

where $h$ is the Planck constant and $c$ is the speed of light.

## 4.2. Spectroscopic study of ytterbium Rydberg states

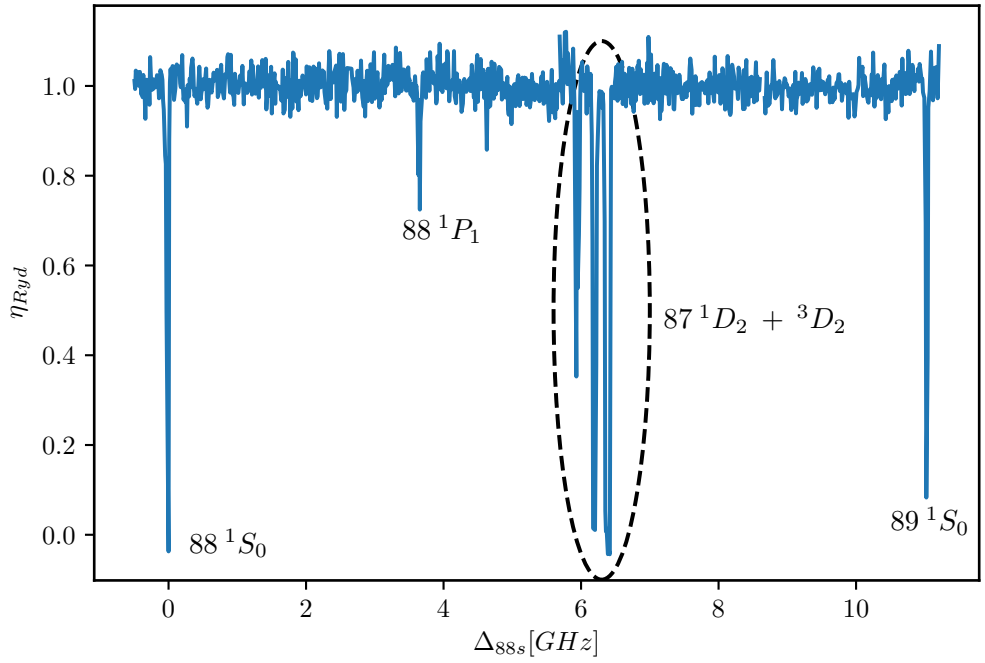


**Figure 4.4.:** *A complete scan from $88\,^1S_0$ to $89\,^1S_0$. The identification was done by comparing the data to [7],[76]. Because of a non zero electric background field the scan shows not only the transition to the S and D Rydberg states but also the actually forbidden transition p state. The frequency of the Rydberg transitions is shown as a difference to the frequency of the $88\,^1S_0$ transition.*

By using the MOT depletion method, as described in section 4.1, we have made an extensive study of highly excited Rydberg states ($n > 50$) of ytterbium. A typical scan over one principal quantum number is shown in figure 4.4. The identification of the Rydberg states is done by comparing the data to previous studies of ytterbium Rydberg states ([7],[76]). The scan was done with a non-zero electric field applied to the Rydberg atoms,

leading to a mixing between the Rydberg states. Therefore it was possible to measure the forbidden transition $6s6p\ ^1P_1 \rightarrow 6snp\ ^1P_1$. The non-zero electric field causes also a splitting of the P and D-states and a stark shift of all Rydberg states. This behavior is described in detail in section 2.3.1.

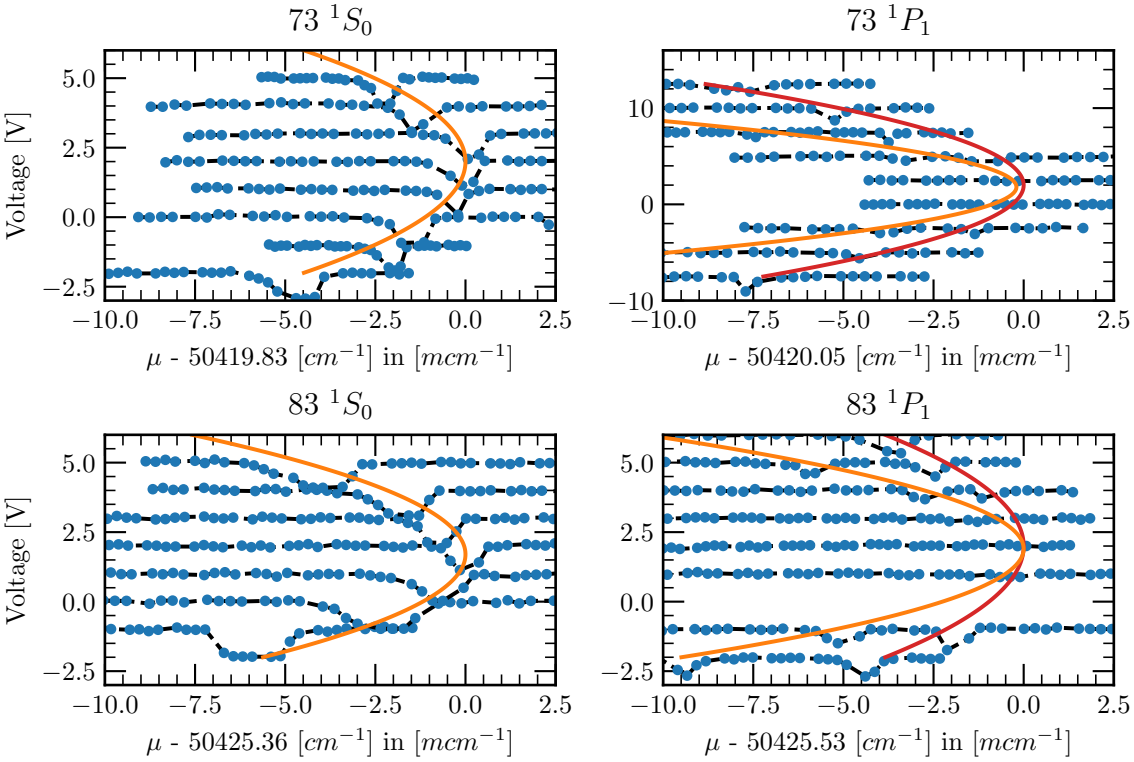


**Figure 4.5.:** *Stark map of the $^1S_0$ and $^1P_1$ Rydberg with $n = 73$ and $n = 83$. The orange and red solid lines are fits of the equation 4.5 to the transition peaks as a function of the electric field. The orange lines are the fits to $m_j = 0$ states and the red lines are fitted $m_j = 1$ states. Near the total electric field zero the transition to $^1P_1$ state is suppressed.*

For the spectroscopic study of the Rydberg states we first scan over a specific energy region, where we predict a Rydberg state (using formula 2.22). After we have found the state, we measure a stark map to determine the zero-field binding energy of the state. Figure 4.5 shows a selection of Stark maps, more precisely the $^1S_0$ and $^1P_1$ state with the principal quantum numbers $n = 73$ and $n = 83$. The external electric field is changed by changing the potential of the plate electrode on the top window (setup shown in section 3.1). Because we use a stark map to determine the binding energies, it is also possible to measure the binding energies of the $^1P_1$ series. As shown in figure 4.5, in the vicinity

of the inversion point of the parabola, i.e. with very small or zero total electric field, no excitation of the $^1P_1$ state is possible. This is, as already mentioned, because this transition is prohibited for vanishing external field. But by fitting the parabola to the transition lines with higher total electric field it is still possible to determine the zero-field binding energy of the P states. With this procedure we identify various Rydberg states which are listed in table 4.1. We also determined the relative polarizability of the $^1S_0$ and $^1P_0$ series, which are discussed in detail in section 5.2. In figure 4.6 the energy of the $^1S_0$ and $^1P_0$ series are

**Table 4.1.:** Experimental energies $E_{exp}$ of the $6sns\,^1S_0$ and the $6sns\,^1P_1$ Rydberg series of $^{174}Yb$ in the range of $n = 70$ to 90. The absolute frequency errors for both series are $\Delta_{^1S_0} = 64\,\mathrm{MHz}$ and $\Delta_{^1P_1} = 50\,\mathrm{MHz}$.

| n | $^1S_0\ E_{exp}\,[\mathrm{cm}^{-1}]$ | $^1P_1\ E_{exp}\,[\mathrm{cm}^{-1}]$ |
|---|---|---|
| 70 | 50417.6765 | 50417.9147 |
| 71 | 50418.4198 | 50418.6607 |
| 72 | 50419.1425 | 50419.3723 |
| 73 | 50419.8349 | 50420.0510 |
| 74 | 50420.4973 | 50420.7051 |
| 75 | 50421.1363 | 50421.3282 |
| 76 | 50421.7370 | 50421.9279 |
| 77 | 50422.3259 | 50422.5053 |
| 78 | 50422.8811 | 50423.0583 |
| 79 | 50423.4223 | 50423.5880 |
| 80 | 50423.9353 | 50424.0945 |
| 81 | 50424.4317 | 50424.5854 |
| 82 | 50424.9074 | 50425.0527 |
| 83 | 50425.3645 | 50425.5098 |
| 84 | 50425.8045 | 50425.9446 |
| 85 | 50426.2281 | 50426.3638 |
| 86 | 50426.6382 | 50426.7651 |
| 87 | 50427.0312 | 50427.1601 |
| 88 | 50427.4132 | 50427.5321 |
| 89 | 50427.7808 | 50427.8976 |
| 90 | 50428.1368 | 50428.2440 |

plotted as a function of the principal quantum number $n$. In the graph one can see that the energy of the states follow equation 2.21. The quantum defect used in this equation is taken from the Rydberg-Ritz fit from the reference [7] ($^1S_0$ series) and from [76] ($^1P_1$ series).

A more detailed comparison can be done by determining the quantum defect $\delta_{n,l}$ from our

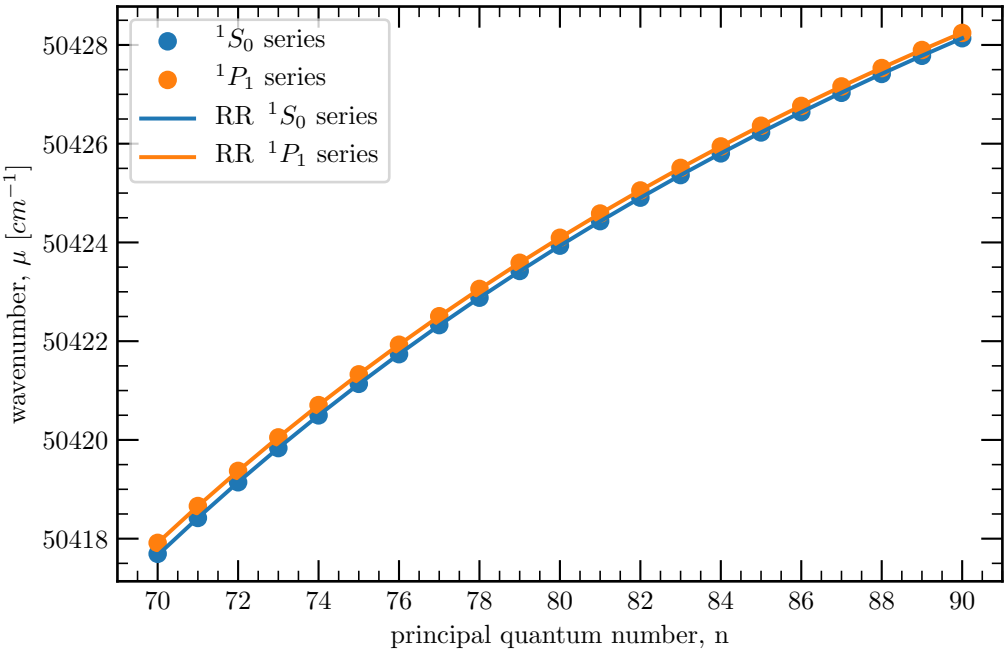


**Figure 4.6.:** *Energy level of the $^1S_0$ and $^1P_1$ series versus the principal quantum number $n$. The sold lines are determined with the equation 2.21 and the the Rydberg-Ritz fits from [7] ($^1S_0$ series) and from [76] ($^1P_1$ series).*

spectroscopic study. By Using the equation 2.21 and the ionisation limit of Yb with the reduced Rydberg constant (both taken from [7]), it is possible to calculate the quantum defect of each state. In figure 4.7 the resulting quantum defects of the $^1S_0$ and $^1P_1$ series, are compared with the Rydberg-Ritz fit, taken from [7] and [76]. With the exception of the $6s70s$ $^1S_0$ state, our quantum defects are in good agreement with values determined in the references. The deviation is maybe attributed to a defective calibration of the wavemeter, which leads to an error in the absolute frequency of the measured state.

A closer comparison of the data with [7] and [76], is shown in figure 4.8. The blue bars are deviations between the measured binding energies and the Rydberg-Ritz fits. The orange bars represent the difference to actually measured energies from the references [7] and [76]. Both comparisons show a similar deviation from our data. Therefore it is a valid assumption to use the Rydberg-Ritz fits for the complete comparison of all binding energies we have measured with the references [7] and [76].

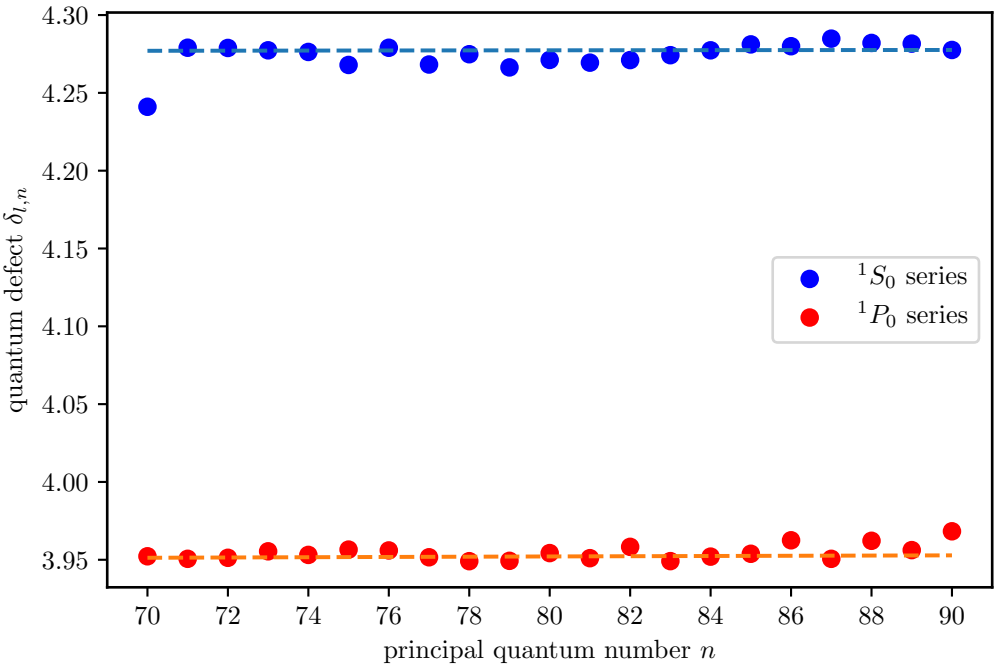


**Figure 4.7.:** *Quantum defect of the $^1S_0$ (blue) and $^1P_1$ (red) series over $n = 70$ to $n = 90$. Dashed lines are Rydberg-Ritz fits taken from [7] and [76].*

The difference in frequency $\mu_\Delta$ between the reference and our data is within the error of our self-built wavemeter, which has an absolute frequency error of 150 MHz ([77]). The mean differences in frequency $\Delta_{^1S_0} = 64\,\text{MHz}$ and $\Delta_{^1P_1} = 50\,\text{MHz}$ in both Rydberg series, are even smaller than the absolute error of the wavemeter (which is maybe overestimated).

Therefore within the accuracy of our wavemeter, we can confirm the binding energies of the $^1S_0$ and $^1P_1$ series published in [7] and [76]. We could also expand the range of measured energy levels in both series over several principal quantum numbers. In the $^1S_0$ series from $n = 80$ to $n = 90$ and in the $^1P_1$ series from $n = 77$ also to $n = 90$. With these measurements, we show that the simple approach of depletion spectroscopy combined with a simple electrode setup is sufficient for a decent spectroscopyic study of Rydberg states.

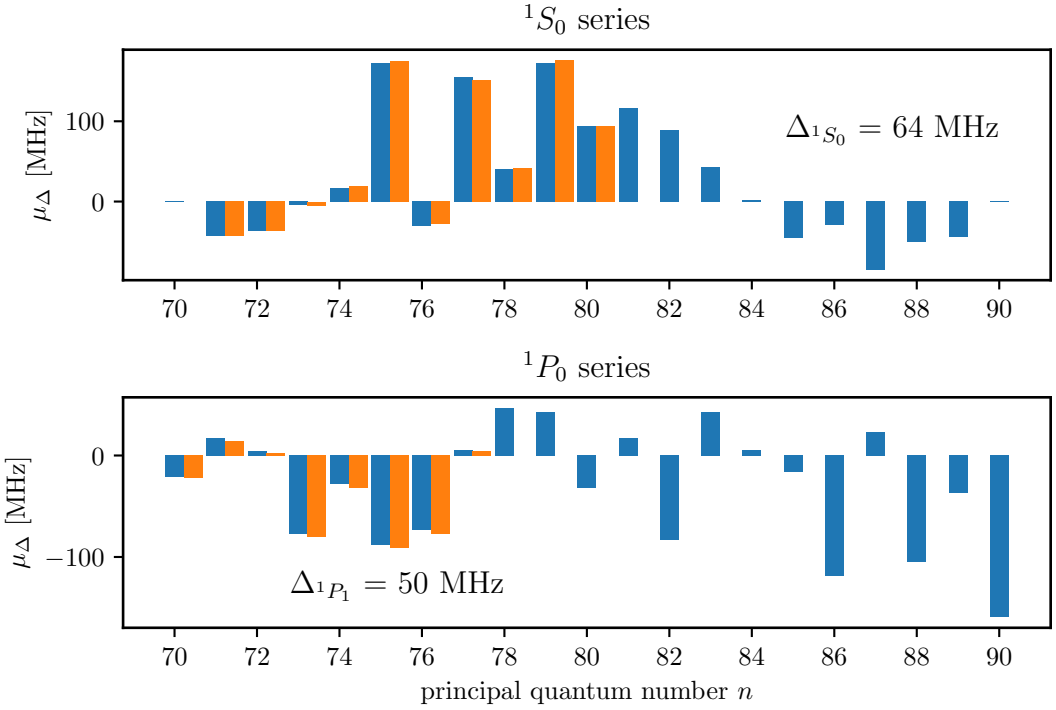


**Figure 4.8.:** *Difference between the binding energies (expressed in units of frequency) as determined in our measurements and in [7, 76]. Orange bars are the differences to individual published measurements, while blue bars are the differences to the Rydberg-Rits fits to the experimental data of [7, 76]. $\Delta_{^1S_0}$ and $\Delta_{^1P_1}$ are the mean deviations between our study and the Rydberg-Ritz fits in [7, 76].*

# 5.

# Polarizability of S and P Rydberg states

Here we present our measurements of the electronic polarizability of Rydberg S- and P-states of Ytterbium and compare them with the numerical calculations. The (electric) polarizability describes the response of an atom in a specific quantum state to an external electric field. A brief introduction into the polarizability of Rydberg states can be found in section 2.3.1. We first take a closer look at the single active electron approximation, with which the polarizability can be calculated *ab initio*. There we introduce two methods with which the dipole matrix can be determined. Finally, the *ab initio* calculations are compared with the measured data and discussed.

## 5.1. Single active electron approximation

For an explicit calculation of the dipole matrix-element between states (see equation 5.2) we need the electron wavefunctions in the atomic potential. While for hydrogen there are analytic solutions, multi-shell atoms need a numerical approach. There are well-established methods for alkali atoms with one single valence electron [78]. In case of a divalent atom, like ytterbium, we have two valence electrons and therefore we have to modify the model. Here we assume that the problem can be modeled as a single valence electron in a modified potential, as already assumed in the reference [76] for strontium. The following derivation for the behavior of Rydberg state in an external electric fields is taken from [78].

First we start with a radial dipole operator which is given by,

$$\hat{d} = e \cdot \hat{r}. \tag{5.1}$$

Where $\hat{r}$ is the radial position operator.Using the second-order perturbation theory the scalar polarizability is given by,

$$\alpha_0(n,l,j) \quad = \quad 2e^2 \sum_{n'l'j'} \frac{\left|\langle\psi_{n'l'j'm'}|\hat{r}|\psi_{nljm}\rangle\right|^2}{E_{n'l'j'} - E_{nlj}}. \tag{5.2}$$

Because this method is limited to small electric fields (see section 2.3.1) one has to use another approach to describe full behavior of Rydberg state in an external electric field. The direct diagonalisation of the Hamilton operator $\mathcal{H}$ instead gives accurate solutions to all orders. The Hamilton operator of an atom in an external electric field is given by,

$$\mathcal{H} \quad = \quad \mathcal{H}_0 + \mathcal{H}_{int} \cdot F. \tag{5.3}$$

Where $\mathcal{H}_0$ is the unperturbed Hamiltonian and $\mathcal{H}_{int}$ gives the coupling between states by the dipole matrix,

$$\mathcal{H}_{int} \quad = \quad e\, a_0 \cdot \ \mathcal{R}\,, \tag{5.4}$$

where $\mathcal{R}$ is the radial dipole matrix. The radial dipole matrix elements are given by,

$$\mathcal{R}_{nLJS,n'L'J'S'} \quad = \quad \left|\langle\psi_{n'l'j'm'}|\hat{r}|\psi_{nljm}\rangle\right|^2 \qquad \text{where} \quad n'l'j'm' \neq nljm \tag{5.5}$$

Where $\psi_{nljm}$ is the wavefunction of the target state and $\psi_{n'l'j'm'}$ is a wavefunction from the set of basis states, which dipole couples to the observed state.

There are multiple approaches to calculate the off-diagonal elements $R_{nLJS,n'L'J'S'}$ of the dipole matrix, which are relevant here. One of them is the calculation of the overlap integral between radial wave functions of the corresponding states (see section 5.1.1). Another approach is a direct calculation of the elements with a semi-classical approach (see section 5.1.2). Both of them are described below and are compared in the case of ytterbium in section 5.1.3.

In both cases it is important, that the set of basis states is large enough to achieve convergence. For larger $n$ the basis has to be bigger, because of the reduction of the energy spacing between the states.

### 5.1.1. Coulomb functions

The following method to calculate the off-diagonal elements $R_{nLJS,n'L'J'S'}$ of the dipole matrix are taken from [78]. One way to calculate the dipole matrix elements is to calculate the radial overlap integral between the states defined in a given basis set. The overlap integral is given by,

$$\mathcal{R}_{nLJS,n'L'J'S'} = \int_{r_i}^{r_0} R_{nLJ}(r)\, r\, R_{n'L'J'}(r)\, r^2\, dr\,, \tag{5.6}$$

where $R_{nLJ}$ is the radial wave function and with $S = S' = 0$ or 1. In the case of a non-hydrogen atom the non relativistic QDT gives a solution for this wave function. As

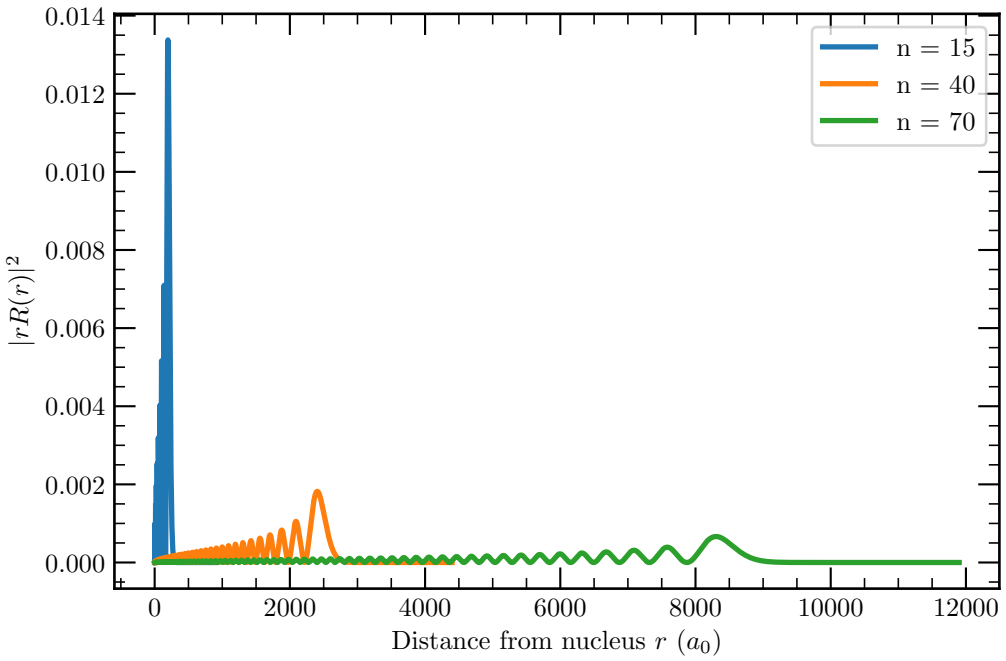


**Figure 5.1.:** *Three electron wavefunctions of Yb with three different principal quantum numbers, $n = 15$ $n = 40$ $n = 70$, where the orbital momentum $l$ and the total angular momentum $j$ are zero. The wavefunctions were calculated using the Coulomb function approach 5.7 with the quantum defect of Yb which are calculated for the three different principal quantum numbers with the Rydberg-Ritz fit (see table A.1 for the fit parameters).*

already discussed in section 2.2.1, the basic idea of the QDT is to consider only large

distances r from the nucleus, where the nucleus is screened by the inner electrons. There the problem is reduced to the hydrogen case, with the exception of effective principal quantum number $n^*$, which is defined by the quantum defect $\delta_{n,l}$. With this reduction to the hydrogen case the problem can be solved analytically using *Coulomb functions* $\mathcal{W}$ [79][80]. The solutions for the wave function are then given by:

$$\begin{aligned} R_{n^*LJ}(r) &= \left(\frac{1}{a_0}\right)^{3/2} \frac{1}{\sqrt{(n^*)^2\Gamma\left(n^*+l+1\right)\Gamma\left(n^*-1\right)}} \\ &\quad \times \mathcal{W}_{n^*,l+1/2}\left(\frac{2r}{n^*a_0}\right) . \end{aligned} \tag{5.7}$$

This approximate wave function has the correct behavior regarding the binding energy and the form of the wavefunction for large $r$, which are important criteria for the calculation of the dipole matrix elements. The information, for which atom the wavefunction is calculated is imprinted in the effective principal quantum number $n^*$. As can be seen in section 2.2.1, effective principal quantum number is defined by the quantum defect, which is unique for every atom species. In figure 5.1 three radial wavefunctions are shown, which are determined using the Coulomb function approach. The electron is in the $s$ state with $j = 0$ and the principal quantum number varies from $n = 15$ to $n = 70$.

### 5.1.2. Semi-classical approach

Instead of calculating the transition dipole matrix using the approximate solution for the radial wave functions, another approach is to directly determine the dipole matrix elements with a semi-classical ansatz [8]. In this ansatz the exact solutions of the dipole matrix elements from the hydrogenic cases are extrapolated to the nonhydrogenic case for large $n$, by using the radial integral method described in [81][82]. The dipole element $\mathcal{R}$ between $|n, L, J, S\rangle$ and $|n', L', J', S'\rangle$ is then given by:

$$\mathcal{R}_{nLJS,n'L'J'S'} = \frac{3}{2} n_c^{*2} \left[1 - \left(\frac{l_c}{n_c^*}\right)^2\right]^{1/2} \sum_{p=0}^{\infty} \gamma^p \, g_p(\Delta n^*) \tag{5.8}$$

with $S = S' = 0$ or 1, $n^*$ is the effective principal quantum number and $l_c, n_c^*, \gamma, \Delta l$ and $\Delta n^*$ are defined as

$$\begin{aligned} l_c &\equiv \frac{L + L' + 1}{2}, \\ n_c^* &\equiv \sqrt{n^{*\prime} n^*}, \\ \gamma &\equiv \frac{\Delta l \, l_c}{n_c^*}, \\ \Delta l &\equiv L' - L, \\ \Delta n^* &\equiv n^* - n^{*'}. \end{aligned}$$

Moreover the first four terms of the MacLaurin series [8] are:

$$\begin{aligned} g_0(\Delta n^*) &= \frac{1}{3\Delta n^*} \left[\mathcal{T}_{\Delta n^*-1}(-\Delta n^*) - \mathcal{T}_{\Delta n^*+1}(-\Delta n^*)\right] \\ g_1(\Delta n^*) &= -\frac{1}{3\Delta n^*} \left[\mathcal{T}_{\Delta n^*-1}(-\Delta n^*) + \mathcal{T}_{\Delta n^*+1}(-\Delta n^*)\right] \\ g_2(\Delta n^*) &= g_0(\Delta n^*) - \frac{\sin \pi \Delta n^*}{\pi \Delta n^*} \\ g_3(\Delta n^*) &= \frac{\Delta n^*}{2} g_0(\Delta n^*) + g_1(\Delta n^*) \end{aligned}$$

Where $\mathcal{T}_{\Delta n^*-1}(-\Delta n^*)$ are the Anger function:

$$\mathcal{T}_s(x) \equiv \frac{1}{\pi} \int_0^\pi d\theta \cos\left[s\theta - x \sin(\theta)\right] . \tag{5.9}$$

As can be seen from equation 5.8 the information about the atom species is only given by the effective principal quantum $n^*$, as with the Coulomb function approach.

### 5.1.3. Comparison of the models

To compare both models we calculate with each approach a Stark map of a specific Rydberg state. The python package *Alkali.ne Rydberg Calculator (ARC)* [62] has proven to be a powerful tool for calculating various properties of alkali Rydberg atoms like the polarizability, the lifetime of states or even the interaction of Rydberg atoms. In a recent update of the package a divalent atom class [83] with Ytterbium was implemented. This update uses the semi classical approach to determine the Stark map of a Rydberg state. For a comparison

of both approaches we added a new function to the divalent atom class, which uses the Coulomb wavefunctions (section 5.1.1) to determine the dipole matrix elements.
For the simulation of the Stark map the already implemented Rydberg-Ritz parameters for the singlet S-,P- and D-Rydberg series are further completed and updated with the spectroscopic data from [76]. The used parameters for the simulations are shown in the table 5.1. A more complete set of the Rydberg-Ritz parameters with the triplet states are shown in the appendix in table A.1.

In both approaches the diagonalisation of the Hamilton operator as a function of an

**Table 5.1.:** The Rydberg-Ritz parameters for the $6sns^1S_0$ and $6sns^1D_2$ series, are taken from [7]. The remaining parameters are taken from fits to spectroscopy data, published in [76]

| Series | $\delta_0$ | $\delta_1$ | $\delta_2$ | $\delta_3$ | $\delta_4$ | $\delta_5$ |
|---|---|---|---|---|---|---|
| $6sns^1S_0$ | 4.278337 | -5.625 | 91.65 | -156050 | -49725000 | 1.1021e+10 |
| $6sns^1P_1$ | 3.95601286 | -30.8616930 | 60222.3884 | -76358128.9 | 3.6197e+10 | – |
| $6sns^1D_2$ | 2.713094 | -1.8646 | -2145.5 | 3940500 | -3103600000 | 1.069e+12 |
| $6sns^1F_3$ | 1.28169811 | -16.8480354 | 806.185504 | – | – | – |

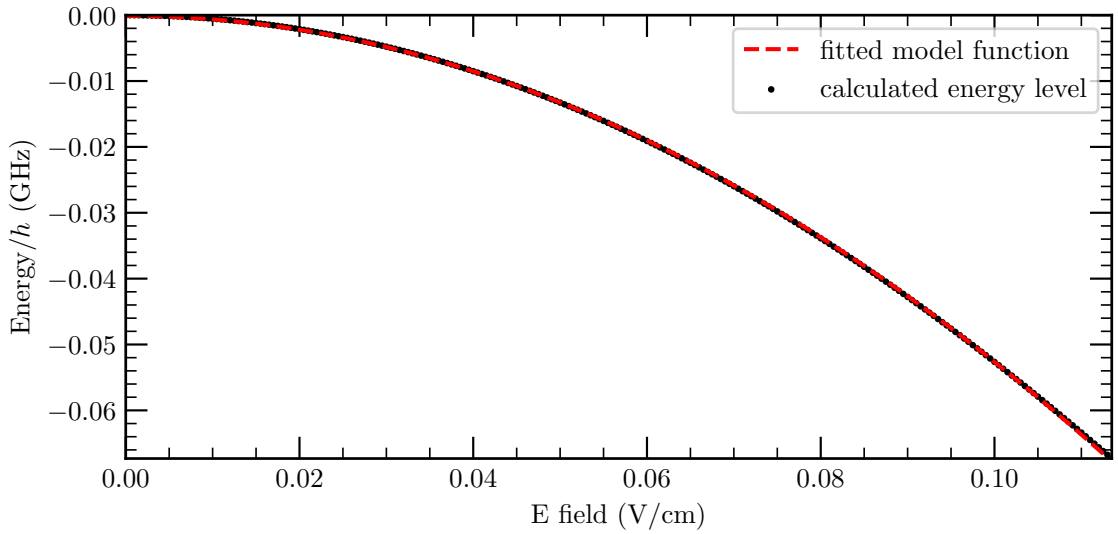


**Figure 5.2.:** *Stark map of the $80^1S_0$ state. The calculation of the dipole matrix is done with the semi classical approach. The model function $\Delta E = 1/2\alpha_0 F^2$ is fitted to the data to determine the polarizability of the state. The graph was created with the ARC package [62] including the divalent atom extension [83].*

external electric field gives a Stark map of a specific state like it is depicted in figure 5.2, where the effect of the electric field to the energy of the $80^1S_0$ of ytterbium is shown. For

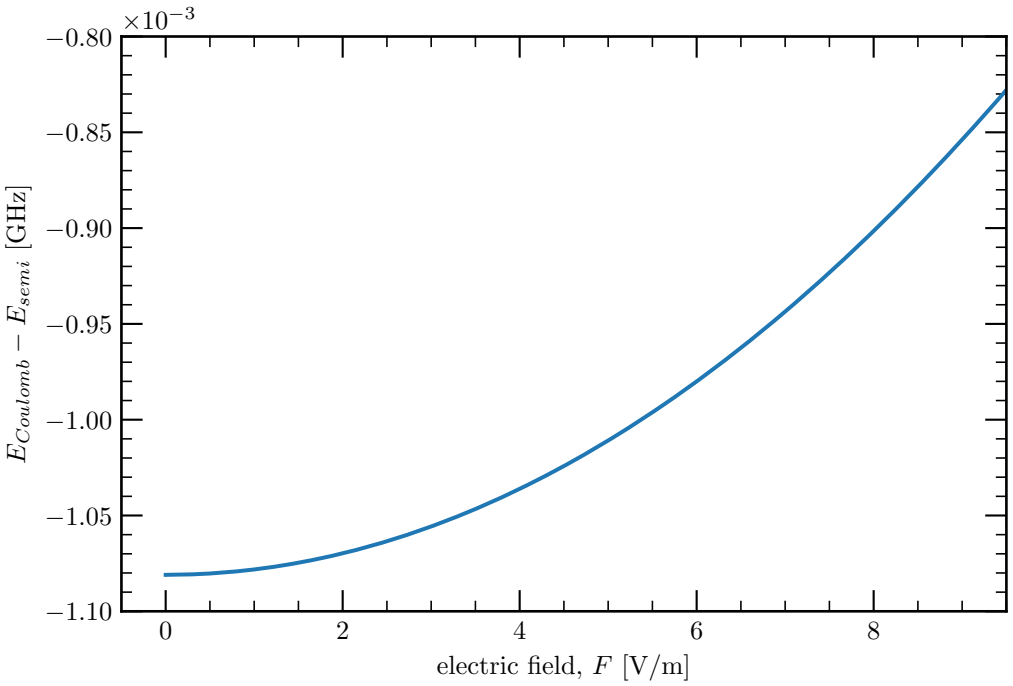


**Figure 5.3.:** *Difference between the semi classical and the Coulomb function approach. The energy difference $E_{Cloumb} - E_{semi}$ is derived from the Stark maps of the $70^1S_0$ state, which are independently calculated with both approaches. The Stark maps were created with the ARC package [62] including the divalent atom extension [83].*

a comparison of both methods a Stark map of the $70\,^1S_0$ state is calculated with both approaches. The energy difference $E_{Cloumb} - E_{semi}$ of those two Stark maps is shown in figure 5.3. As can be seen the difference between both approaches is approximately 1 Mhz at zero external electric field, where the energy level from the semi classical approach is slightly higher. With increasing electric field the difference between both approaches decreases. The polarizability of the $70\,^1S_0$ state from the semi classical approach is smaller than the polarizability which results from the Coulomb function approach. This deviation causes the reduction of the energy difference between both approaches with increasing external electric field. To determine the difference between polarizabilities of both approaches, the model function $\Delta E = 1/2\alpha_0 F^2$ is fitted to the state energy to both approaches. Both

models, the Coulomb wavefunction approach and the semi classical approach, yield the same polarizability within a 2% error. This coincides with the investigations made in [78]. There these two methods were also compared with each other in the context of alkali atoms. Since the computational effort of the semi classical approach is many times lower and the systematic experimental error caused by the uncertainty of the electric field is 25% (see section 5.2), the semi classical method is used to analyze the experimental measurements, made in this thesis.

## 5.2. Experimental determination of ytterbium polarizabilities

The data shown in this section were measured during the two different setups (stage 1 and stage 2) as described in section 3.1. Because of the not well-controlled electrode setup of the first stage, it was not possible to accurately simulate an electric field as a function of the applied voltage. Therefore, only relative values of the scalar polarizability $\alpha_0(n, l, j)$ of the Rydberg states could be determined from the Stark maps, which were measured with the MOT depletion method (see figure 4.5). All polarizabilities are normalized to the polarizability of the $6s70s\,^1S_0$ state.

In the second stage it was possible to simulate the electric field precisely, as shown in section 3.2. Knowing the electric field it is possible to measure precise Stark maps of the Rydberg states from which the scalar polarizability can be determined.

In the second stage of the experiment setup, the detection of the Rydberg atoms changed from the indirect MOT depletion method (see section 4.1) to the direct field ionisation method. With this method the Rydberg atoms are first ionized by an external electric field pulse and then detected by a MCP. A detailed description of the ionisation process can be found in chapter 6.

The experimental procedure for determining the Stark map of a particular Rydberg state is shown in figure 5.4. The first step is to set the external electric field to a specific value by defining the amplitude parameter $A$ of the electric compensation field (see section 3.2.3). Then the Rydberg laser is scanned over specific frequency band to determine the energy binding of the Rydberg state. The frequency of the Rydberg laser is thereby changed in steps. For each frequency step the Rydberg transition is probed 100 times. In each probing the ytterbium atoms are radiated by a 500 ns Rydberg laser light pulse. Then an external

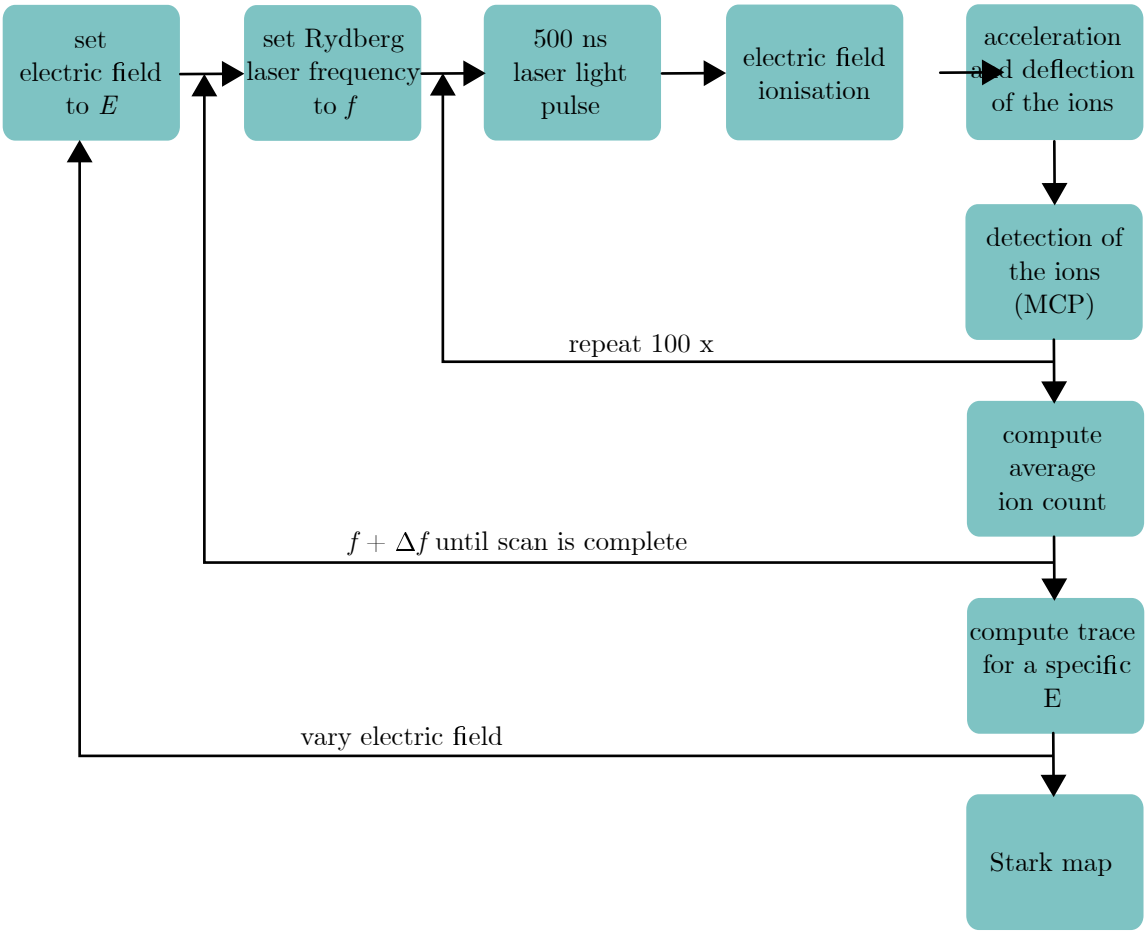


**Figure 5.4.:** *Experimental sequence to determine the Stark map of a Rydberg state using the field ionization method. The amplitude of the compensation field is varied by approximately ±10%. The frequency of the Rydberg laser is scanned over the Rydberg transition to compensate frequency drifts of the Rydberg laser. To minimize counting the error the measurement is repeated 100 times per Rydberg laser frequency and ionisation field.*

electric field is applied to ionize the Rydberg atoms. Subsequently, a different electric field pulse directs the ions toward the MCP (see section 3.2.5). After the Rydberg laser is completely scanned over the Rydberg transition, the measurement is repeated with a different amplitude parameter $A$, thus with a different value of the external electrical field.

Several Stark maps measured using the field ionization method are shown in figure 5.5. From these maps the polarizability of observed Rydberg states can be determined, as with the MOT depletion method (section 4.1). The polarizability for both stages is shown in table 5.2 and 5.3(measured in the second stage of the apparatus).

As can be seen in figure 5.6 the polarizability matches within the error with the *ab initio*

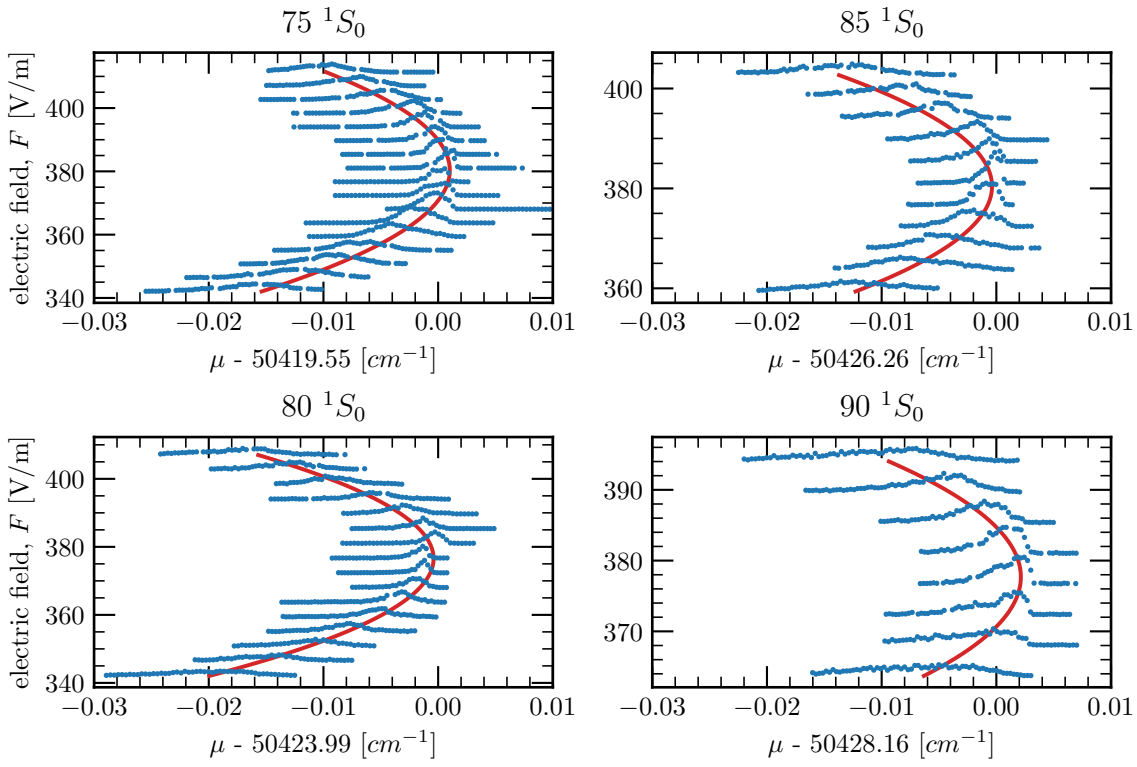


**Figure 5.5.:** *Stark map of the $80^1S_0$ state. The calculation of the dipole matrix is done with the semi classical approach. The model function $\Delta E = 1/2\alpha_0 F^2$ is fitted to the data to determine the polarizability of the state. The graph was created with the ARC package [62] including the divalent atom extension [83].*

calculations, which are based on the semi classical approach (see section 5.1.2). Therefore it is demonstrated that this approach is suitable to calculate scalar polarizabilities of Ytterbium Rydberg states.

The error of the measured polarizability arises from the position uncertainty of the MOT and the inter-electrode distance. Here, the MOT position has the greatest influence on the error. A deviation of ±2 mm in the MOT position causes a change of the absolute value of the compensation field of approximately 15% (see figure 3.11). The uncertainty of the electrode distance increases the change by 1.5% to 16.5% (see section 3.2.4)).

Since the polarizability scales quadratic with the electric field, the position uncertainty causes an relative error of 36% in determination of the polarizability of the Rydberg states.

With polarizabilities of the ytterbium Rydberg states measured in the second stage of the apparatus it is also possible to re-scale the relative polarizabilities that are measured in the first stage of the experiment. To determine the re-scaling factor $s$ we have to minimize the

**Table 5.2.:** Scalar polarizability $\alpha_0$ of the $6sns^1S_0$ and the $6sns^1P_1$ Rydberg series of $^{174}Yb$, measured in the first stage of the experiment, normalized to the polarizability of the $6s70s^1S_0$ state.

| | $^1S_0$ | $^1P_1$ | |
|---|---|---|---|
| n | $\alpha_0(n,0,0)$ | $\alpha_0(n,1,1)$ $m_j=0$ | $\alpha_0(n,1,1)$ $m_j=1$ |
| 70 | 1.00 | 0.85 | 0.38 |
| 71 | 0.88 | 1.00 | 0.37 |
| 72 | 1.02 | 1.00 | 0.43 |
| 73 | 1.18 | 1.59 | 0.56 |
| 74 | 1.37 | 1.20 | 0.54 |
| 75 | 1.80 | 1.27 | 0.42 |
| 76 | 1.77 | 1.59 | 0.56 |
| 77 | 1.55 | 1.60 | 0.65 |
| 78 | 1.53 | 1.78 | 0.63 |
| 79 | 2.09 | 2.10 | 0.72 |
| 80 | 2.83 | 2.19 | 0.76 |
| 81 | 2.45 | 2.65 | 0.79 |
| 82 | 2.64 | 3.05 | 1.01 |
| 83 | 2.84 | 3.13 | 1.03 |
| 84 | 3.54 | 3.22 | 1.02 |
| 85 | 3.17 | 3.69 | 1.45 |
| 86 | 3.70 | 3.78 | 1.51 |
| 87 | 3.91 | 4.41 | 1.45 |
| 88 | 4.92 | 4.41 | 1.57 |
| 89 | 4.69 | 4.67 | 1.56 |
| 90 | 5.60 | 3.80 | 1.07 |

function,

$$\mathcal{F}(s) \;=\; \sum_n \left[\alpha_{0,2nd}(n,l,j) - s\cdot\alpha_{0,1st}(n,l,j)\right]^2 . \tag{5.10}$$

Where $\alpha_{0,1st}(n,l,j)$ are the relative polarizabilities measured in the first stage and $\alpha_{0,2nd}(n,l,j)$ are the absolute polarizabilities measured in the second stage. The sum is over all states measured in both stages of the experiment. The minimization of the Function $\mathcal{F}$ yields a re-scaling factor of

$$s \;=\; 3258.2\,\mathrm{MHz\,cm^2/V^2} . \tag{5.11}$$

**Table 5.3.:** Scalar polarizability $\alpha_0$ of the $6sns\,^1S_0$ Rydberg series of $^{174}Yb$, measured in the second stage of the experiment.

| | $^1S_0$ |
|---|---|
| n | $\alpha_0(n,0,0)\left[\text{MHz cm}^2/\text{v}^2\right]$ |
| 40 | 211 |
| 50 | 452 |
| 60 | 1579 |
| 70 | 5674 |
| 75 | 6404 |
| 80 | 10424 |
| 85 | 15368 |
| 90 | 24688 |

The result of the re-scaling of the relative polarizabilities of the S-Rydberg series is shown in figure 5.7. It can be seen that the measured polarizabilities from the first stage have the same scaling behavior with the principal quantum number $n$ as the polarizabilities measured in the second stage. It is also shown, that the measured polarizabilities are smaller than the *ab initio* calculation which is most likely caused by underestimating the electric field in the experiment.

To determine how much weaker the electric field would have to be for the measured polarizabilities to match the numerical ones, an additional scaling factor can be determined. As before, this minimizes the sum 5.10. This time, however, the relative polarizabilities are compared with the numerical determined polarizabilities. The minimization yields a new re-scaling factor of

$$s_{new} \quad = \quad 4599.0\,\text{MHz cm}^2/\text{V}^2\,. \tag{5.12}$$

Comparing s with $s_{new}$ and taking into account that the polarizability scales quadratically with the electric field, an increase of the electric field of about 18% is necessary for the measured values to agree with the numerically determined values. As shown in chapter 3.2.4, this deviation can be explained by the error of the position of the MOT to the electrodes. Therefore it is shown, that with the MOT depletion method and a precise knowledge of the

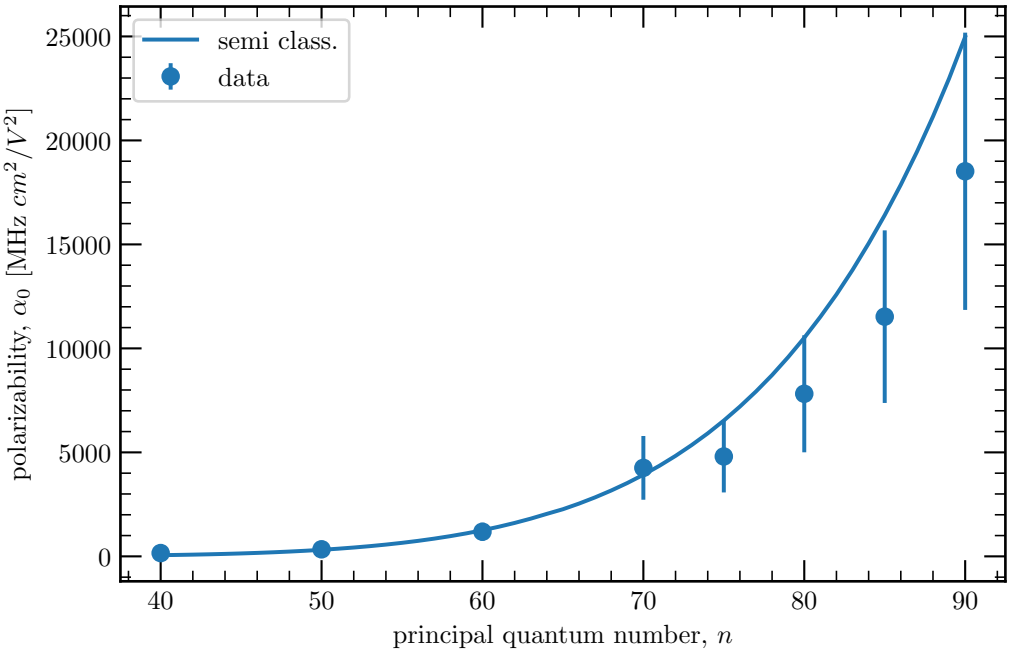


**Figure 5.6.:** *Scalar polarizability $\alpha_0$ in dependency to the principal quantum $n$. The solid blue line is ab initio calculated polarizability with the semi-classical approach (described in section 5.1.2). The calculations are done with [62] and [83]. Blue points are the polarizability $\alpha_0$, measured during the second stage of the experiment. The error from the measurement is estimated from the position uncertainty of the MOT and the uncertainty in the inter-electrode distance (see section 3.2.4).*

electric field it is possible to measure accurately the polarizabilities of ytterbium Rydberg states.

As in section 4.1 described, it was also possible to measure Stark maps of the $^1P_1$ series, although the transition is actually forbidden. This is possible because the external electric field mixes the Rydberg states, which cancels the parity selection rules. In figure 5.8 the polarizabilities of the S and P states, measured in the first stage of experiment are shown. The measurements of the first stage are scaled to the measurements of the second stage as before, by applying the re-sclaing factor $s_{new} = 4599.0\,\mathrm{MHz\,cm^2/V^2}$ to all relative polarizabilities. The measurement shows an agreement between the polarizabilities of the S states and the polarizabilities of the $m_J = 0$ P states. The *ab intio* calculations confirms this agreement.

A comparison of the measured polarizabilities of the $m_J = 0$ and $m_J = 1$ $^1P_1$ states in the

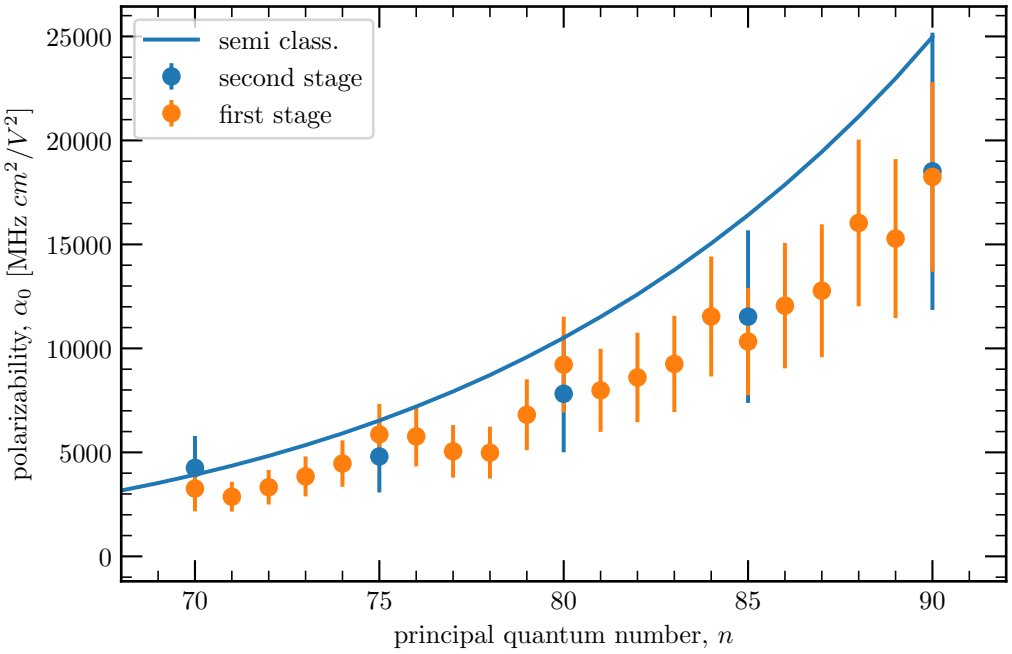


**Figure 5.7.:** *Re-scaling of the relative polarizabilities of the* $^1S_0$ *series from the first stage. The re-scaling is done by finding the minimum of the function 5.10. The resulting re-sclaing factor* $s = 3258.2\,\mathrm{MHz\,cm^2/V^2}$*. The re-scaled polarizabilities are in good agreement with the ab initio calculation,based on the semi classical approach (see section 5.1.2)*

interval from $n = 70$ to $n = 90$ yields a mean ratio of $r_{measured} = 2.82 \pm 0.34$. The analysis of the *ab intio* numerical calculated polarizabilities yields a mean ratio of $r_{abinitio} = 2.36 \pm 0.04$. The ratios $r_{measured}$ and $r_{abinitio}$ agree almost within the error. However, the deviation is so minimal that, for example, a larger series of measurements could well lead to a matching of the ratios.

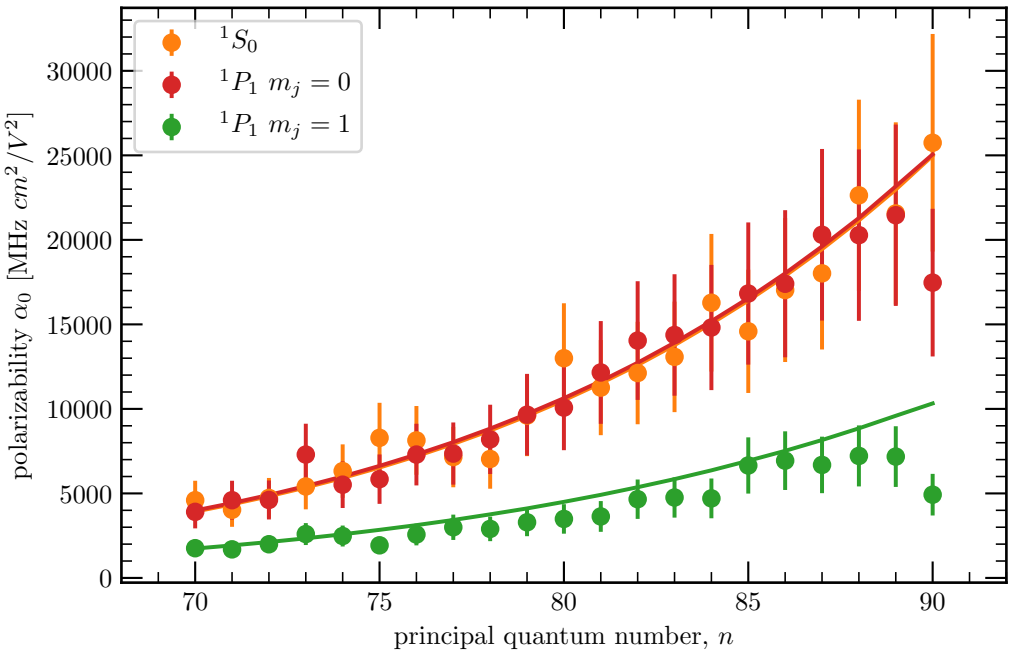


**Figure 5.8.:** *Scalar polarizability $\alpha_0$ of the $6sns\,^1S_0$ and the $6sns\,^1P_1$ Rydberg series of $^{174}Yb$, from $n = 70$ to $n = 90$. Solid lines are ab initio calculations, done with [62] and [83]. Orange is the polarizability of the $6sns\,^1S_0$ series. Green ($m_j = 1$) and red ($m_j = 0$) represents the $6sns\,^1P_1$ series. All data are scaled with the factor $s_{new} = 4599.0\,\mathrm{MHz\,cm^3/V^2}$, as described in section 5.2.*

# 6.

# Electric field Ionisation

Electric field ionisation is a standard tool to detect Rydberg atoms. In principal it can be 100% efficient and all Rydberg atoms can be detected. Using this method it is possible to measure properties of the Rydberg states like for example the lifetime (see chapter 7). To explain the complex phenomenon of the ionisation process of a Rydberg state, we start with the most basic model of a hydrogen atom. After field ionisation of hydrogen is introduced, the difference between hydrogen and other atoms is discussed. In the last part of this chapter the measurement of the ionisation threshold of the $^1S_0$ and $^1D_2$ Rydberg series is presented.

## 6.1. Electric field ionisation of atomic hydrogen

To explain the ionisation behavior of Rydberg atoms we start with the hydrogen atom. In this chapter we will follow reference [1]. The first order energies $E_R$ of an electron in a hydrogen atom potential with an external electric field $F$ applied along the z axis are given by,

$$E_R = -\frac{R_y}{n^2} + \frac{3}{2} F e a_0 n \left(n_1 - n_2\right). \tag{6.1}$$

Here the energy is given with respect to the ionisation limit. The quantum numbers $n_1$ and $n_2$ are the so-called parabolic quantum numbers. They are useful to describe the electron wavefunction, because the external electric field deforms the spherical symmetric potential such that the orientation of the electron wave function relative to the electric field becomes crucial. The orientation is quantized by the parabolic quantum numbers. For the parabolic

quantum number the relationship

$$n_1 + n_2 + m + 1 \quad = \quad n \tag{6.2}$$

applies. Thus it follows for a given $n$ and $m$, that there are $n - |m|$ Stark levels, as can be seen in figure 6.1. The energy levels that are shifted towards the ionisation limit are called blue states and the ones that are shifted away from the limit are called red states. Spatially, the wave functions of the blue states are shifted towards the +z axis side and the red states towards the -z axis side. The electric field where the extreme $m = 0$ red and blue stark levels of states with principal quantum number n and n+1 cross, is approximately given by

$$F = \frac{16\pi\epsilon_0}{3e^3} \cdot \frac{R_y^2}{n^5} \,. \tag{6.3}$$

This crossing field is connected to the Inglis-Teller limit where levels of adjacent $n$ become unresolvable [84]. This limit is used in astrophysics to determine the electron density of stars [85].

The electric field where the Rydberg atoms ionize can be estimated using the Coulomb-Stark potential. The potential is given by:

$$V\,(r, z) \quad = \quad -\frac{e}{4\pi\epsilon_0} \cdot \frac{1}{r} + F \cdot z \,. \tag{6.4}$$

Where $F$ is the applied electric field along the $z$ axis, $e$ is elementary charge, $\epsilon_0$ the dielectric constant and $r$ the radial distance to the hydrogen core.

The electric field deforms the atomic potential so that the highly excited Rydberg states are no longer bound to the nucleus, which is illustrated in figure 6.2. The atom ionizes when the energy level of the Rydberg state is above the saddle point of the Coulomb-Stark-potential.To investigate the saddle point further, we express $r$ in terms $z$. Using cylinder coordinates where, $r^2 = \rho^2 + z^2$. Therefore equation 6.4 can be written as,

$$V\,(\rho, z) \quad = \quad -\frac{e}{4\pi\epsilon_0} \cdot \frac{1}{(\rho^2 + z^2)^{1/2}} + F \cdot z \tag{6.5}$$

The saddle point of the atomic potential can be determined using the derivative of the

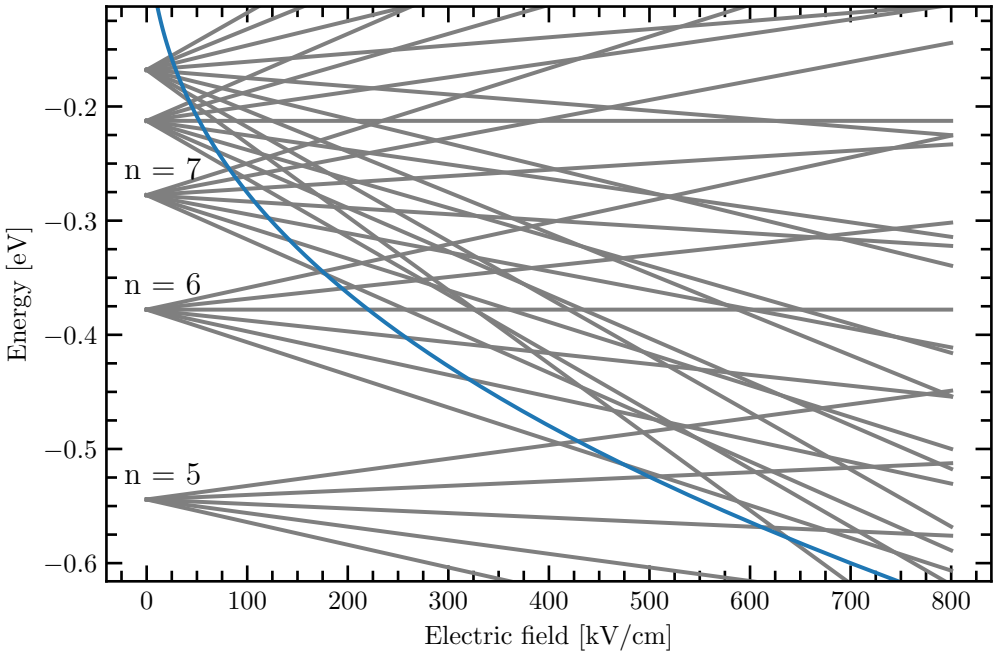


**Figure 6.1.:** *Hydrogen Stark manifold for $m = 0$. The energy levels (grey lines) splitted into the parabolic state according to equation 6.1. The Inglis-Teller limit (blue line) indicates the electric field, where the states starts to cross each other [84].*

potential along the z-direction according to

$$\frac{\partial V(\rho, z)}{\partial z} = \frac{e}{4\pi\epsilon_0} \cdot \frac{z}{(\rho^2 + z^2)^{3/2}} + F \equiv 0 \tag{6.6}$$

For the ionisation process the position of the saddle point along the electric field is important. Therefore it can be assumed that $\rho \equiv 0$ and equation 6.6 simplifies to

$$0 = \frac{e}{4\pi\epsilon_0} \cdot \frac{\pm z}{\left((\pm z)^2\right)^{3/2}} + F = \pm\frac{e}{4\pi\epsilon_0} \cdot \frac{1}{z^2} + F\,. \tag{6.7}$$

The solution of this equation yields the position of the saddle point:

$$z_0 = -\frac{1}{\sqrt{4\pi\epsilon_0/e \cdot F}} \tag{6.8}$$

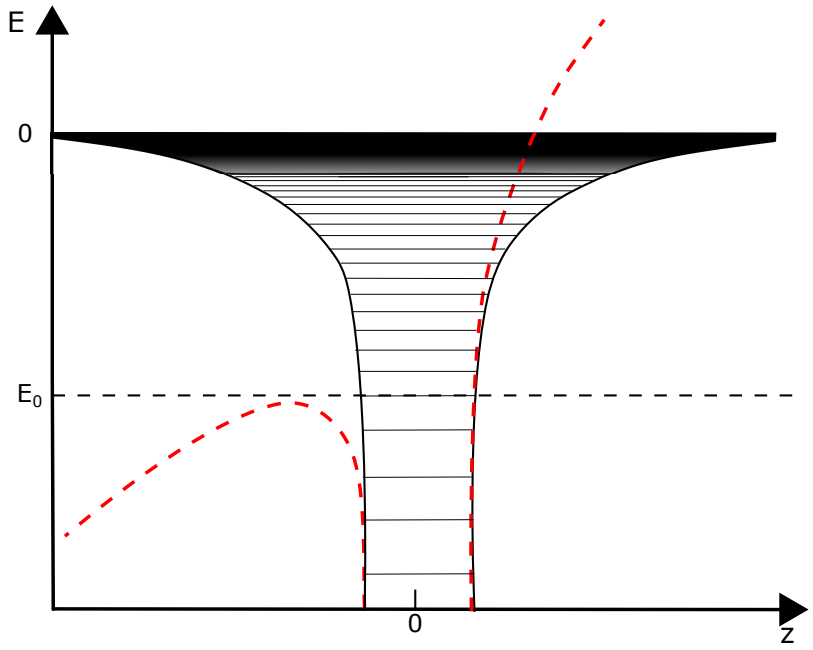


**Figure 6.2.:** *Schematic drawing of the hydrogen potential. The red dashed line indicates the deformation of the potential due to an external electric field. $E_0$ is saddelpoint of the atom potential and specifies which Rydberg states ionize.*

and the potential at the saddle point

$$V_0 = -\frac{e}{2\pi\epsilon_0} \cdot \sqrt{4\pi\epsilon_0/e \cdot F}\,. \tag{6.9}$$

Using the relationship between energy and electric potential $E_0 = e \cdot V_0$, the classical ionisation field is given by,

$$F_0 = \frac{\pi\epsilon_0}{e^3} \cdot E_0^2\,. \tag{6.10}$$

Ignoring the Stark shift and setting the binding energy of the saddle point $E_0$ equal to the energy $E_R(n)$ of a specific Rydberg state, the electric field required to ionize the specific Rydberg state is given by,

$$F_0 = \frac{\pi\epsilon_0}{e^3} \cdot \frac{R_y^2}{n^4}\,. \tag{6.11}$$

where $R_y$ is the Rydberg constant in units of energy $R_y = R_\infty hc$. If we include the linear Stark effect, the binding energy of an electron changes with the electric field $F_0$. For the reddest (energetically lowest) state in a Stark manifold of a specific Rydberg state with

$m = 0$, the approximation $n_1 - n_2 - m \approx -n$ simplifies the equation 6.1 to

$$E_R(n) = -\frac{R_y}{n^2} - \frac{3}{2}F_0 \cdot e \cdot a_0 \cdot n^2 \,, \tag{6.12}$$

where $a_0$ is the Bohr radius. Thus the threshold field for the ionisation of a hydrogen Rydberg atom is given by,

$$\begin{aligned} F_0 &= \frac{\pi \cdot \epsilon_0}{e^3}\left(-\frac{R_y}{n^2} - \frac{3}{2}F_0 \cdot e \cdot a_0 \cdot n^2\right)^2 \\ &= \frac{\pi \cdot \epsilon_0}{e^3}\left(\frac{R_y^2}{n^4} + \frac{5}{8}\frac{e^3}{\pi\epsilon_0} \cdot F_0 + \frac{9}{4}e^2 n^4 a_0^2 \cdot F_0^2\right) \end{aligned} \tag{6.13}$$

This equation yields the following two solutions for the ionization limit of a Rydberg atom,

$$F_0 = \frac{\pi\epsilon_0}{e^3} \cdot \frac{R_y^2}{n^4} \cdot \frac{80 \pm 64}{9} \,. \tag{6.14}$$

The two solutions arise from the Stark shift of the Rydberg state. The lower limit describes the case when the deformation of the atomic potential is strong enough to ionize the atom. The upper limit describes the case when the Stark shift of the state is larger than the suppression of the atom potential, caused by the applied electric field. This behavior is illustrated in figure 6.3, where the two limits define the region (yellow) where the suppression of the atomic potential is larger than the Stark shift of the states and the atom ionizes. The upper limit only arises if the external electric field pulse duration is in the order of the Rydberg period, which is in the time scale of pico seconds. This regime can be achieved with single cycles laser pulses [86]. In this regime there are various ionisation mechanisms like the impulsive-kick ionisation [87] or the displacement-ionisation mechanism [88]. These mechanisms can change the scaling behavior of the ionisation with the principal quantum number (but they are not relevant here).

## 6.2. Nonhydrogen Rydberg atoms

The characteristic of a non-hydrogen atom in an electric field can be inferred from the behavior of the hydrogen atom as discussed in the previous chapter, but there are significant differences due to the finite sized ionic core. Due to the scattering of the electron with the core, the wave function is no longer separable in parabolic coordinates, $n_1$ is no longer a

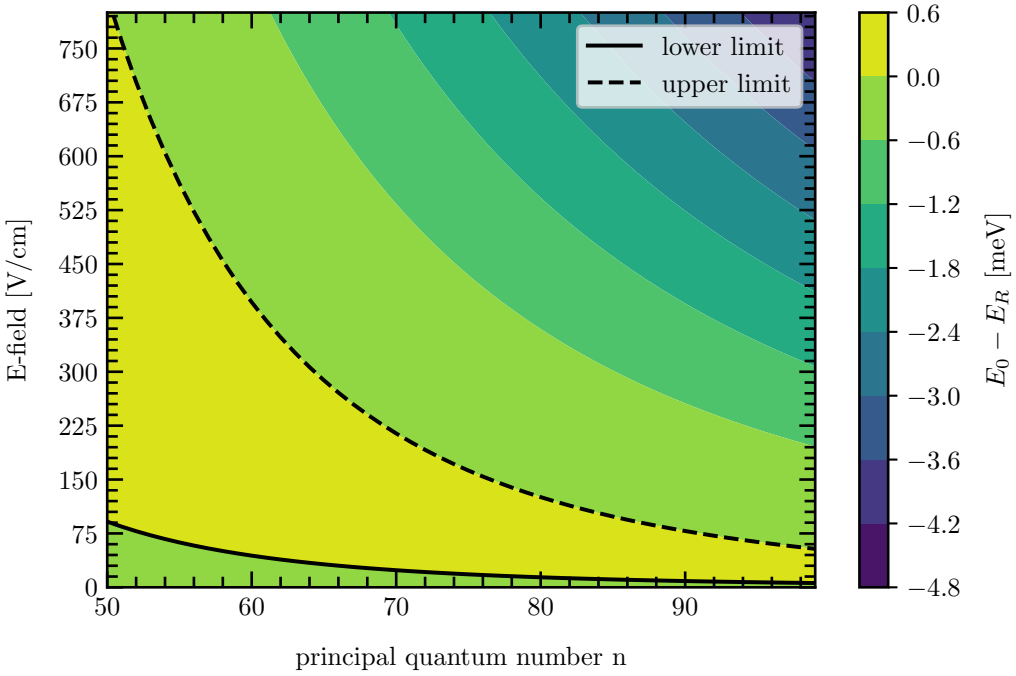


**Figure 6.3.:** *Contour plot of the energy difference between the Energy of the saddelpoint $E_0$ and the energy of stark shifted state $E_R$, with dependency to the external electric field and the principal quantum number n. The two black lines are the solution for the ionisation limits from equation 6.14. For the solid line the deformation is bigger than the shift of the states, which results in the ionisation of the atom. The dashed lines represents the case when star shit becomes bigger than the deformation which should suppress the ionisation.*

good quantum number. This implies that in non-hydrogen atoms the blue and red states of adjacent n are coupled via the core. On the one hand, this causes avoided crossings and on the other hand it leads to an autoionisation of blue states below the classical ionisation limit.

To investigate the behavior of the states it is convenient to look at the Hamiltonian of the system. As already described in section 5.1 the Hamiltonian for a single active electron is given by

$$\mathcal{H} \quad = \quad \mathcal{H}_0 + \mathcal{H}_{int} \cdot F \,, \tag{6.15}$$

where the diagonal elements of $\mathcal{H}_0$ are the zero electric field energy levels, which are shifted by the state dependent quantum defect compared to the hydrogen atom. In the off-diagonal

elements of $\mathcal{H}_{int}$ the overlap between the wavefunctions of the observed state and the neighboring $n$ and $l$ states is included. The eigenvalues of $\mathcal{H}$ correspond to the energy levels of an atom in an external electric field $F$. By diagonlizing the Hamiltonian for a set of external electric fields $F$, it is possible to generate a Stark map of Yb of specific state, as can be seen in figure 6.4, where a Stark map of the $80^1S_0$ is shown.
At an electric field value of 0.5 V/cm the $80^1S_0$ state is not crossing with the Stark manifold of an adjacent state, but the states are bending away from each other. This behavior is called avoided crossing. The avoided crossing between adjacent $l$ states stands in contrast to the behavior of hydrogen Rydberg states, where there is first no difference in the shift of different $l$ states with the same principal quantum number $n$ and second a crossing of the energy levels of Stark manifolds with different principal quantum number $n$ (see figure 6.1) is observed. In conclusion the crossing behavior of non hydrogen differs from hydrogen as follows.

- The energy levels of Rydberg states in non hydrogen atoms avoid crossing.
- The crossing in non-hydrogen atoms happens between energy levels with the same principal quantum number $n$ but with different orbital quantum $l$
- The avoided crossing happens at lower electric fields, compared to the crossing of the energy levels of hydrogen atoms.

According to [1] the energy gap of the avoided crossing $\Delta E$ is proportional to,

$$\Delta E \propto \frac{\delta_l}{n^4} \tag{6.16}$$

### 6.2.1. Pulsed field Ionisation

For the ionisation process of a Rydberg state the time profile of the electric field is crucial. Due to the avoided crossings of the states in the presence of the electric field, there are two pathways through a Stark manifold. Either the passage of the crossings is diabaticaly, which means that the electron transfers from one state to the adjacent state, or the electron stays in the original state, which is an adiabatic passage. In figure 6.5 the difference between these two types of passage is illustrated.

To distinguish between an adiabatic or a diabatic passage the energy gap of the crossing

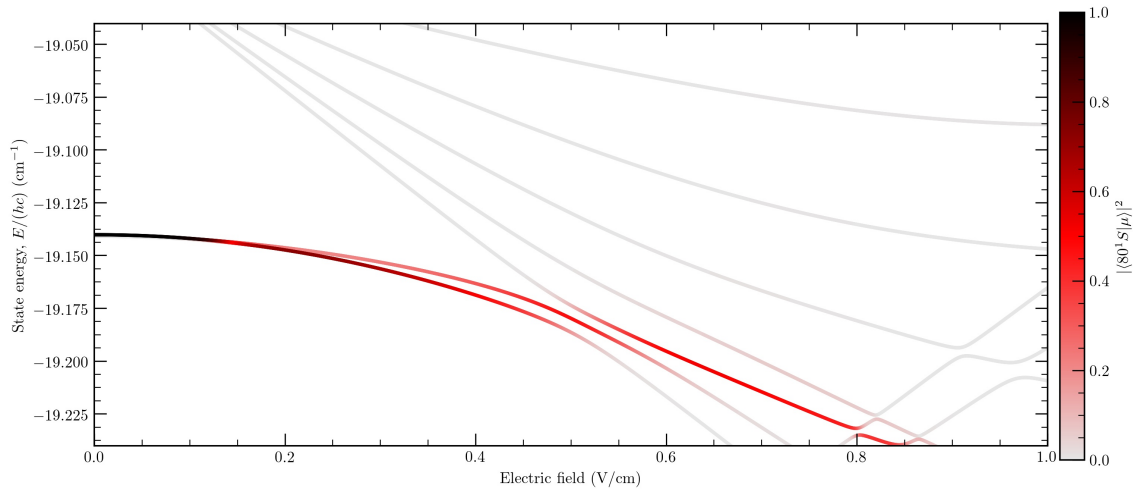


**Figure 6.4.:** *Calculated Stark map of the Yb $80^1S_0$ state. The Stark map is generated by diagonalizing the Hamiltonian 6.15. The calculation and figure is done with the python library "ARC" [62]. The Stark map, shows the avoided crossing with stark manifold of an adjacent state at $0.5\,\mathrm{V/cm}$. The color map shows the state mixing due to the avoided crossing.*

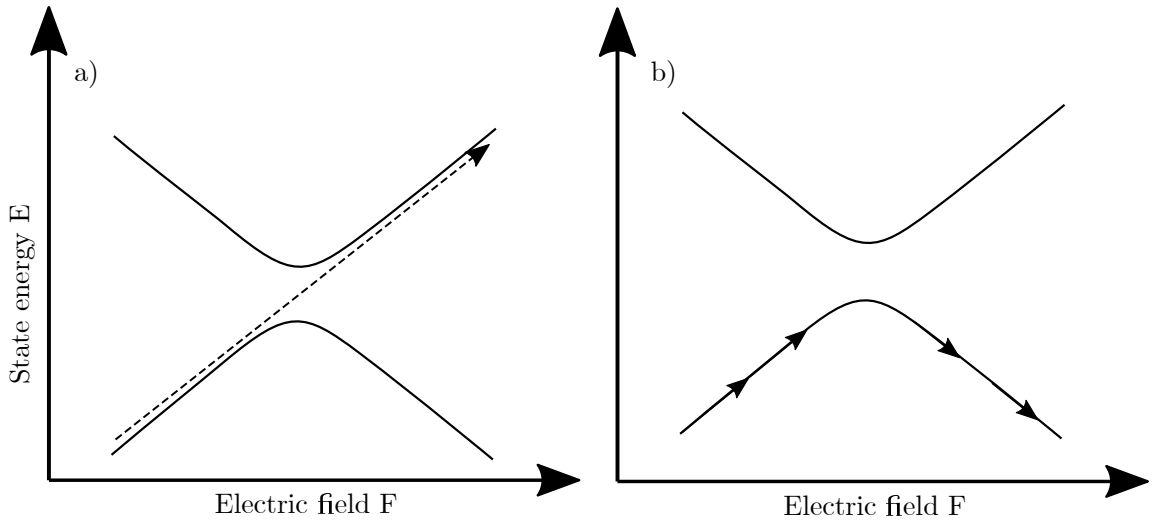


**Figure 6.5.:** *Dibatic and adiabatic passage of a avoided crossing in a Stark manifold. In a diabatic passage a) the electron transfers to the adjacent state. This passage becomes more likely when energy gap of the crossing is small and the slew rate of the electric field is fast. b) During an adiabtaic passage the electron remains in the original state, which is deflected by the adjacent one.*

and the slew rate of the electric field is important. The energy gap is influenced by the coupling of the states and is therefore is a property of the atom. If the coupling between the states is strong the resulting energy gap is big and an adiabatic passage becomes more

likely. As already described in the section before, the gap also scales with $\delta_l/n^4$, so with increasing $n$ and $l$ the passage of the avoided crossing becomes more likely diabatical. However the slew rate $S$ of the electric field is given by the experiment and thus can be influenced. If the electric field traverses the crossing in a short time period the crossing becomes more likely adiabatic. The relationship between slew rate and the energy gap is described by the critical slew rate $S_x$,which is given by [1],

$$S_x = \frac{\Delta\omega^2}{\frac{dE_1}{dF} - \frac{dE_2}{dF}}, \tag{6.17}$$

where $\frac{dE_1}{dF}$ and $\frac{dE_1}{dF}$ are the Stark shifts of the two crossing states. The energy gap expressed in frequency is,

$$\Delta\omega = \frac{\Delta E}{\hbar}. \tag{6.18}$$

In conclusion if $S << S_x$ the passage is adiabatic and if $S >> S_x$ the passage is diabatic. According to the assumptions and approximations made in [1], equation 6.17 implies an adiabatic passage even for a rise time of $\approx 1\,\mu$s and $n = 100$.
One method to investigate if the ionisation process is diabatic or adiabatic is to measure the ionisation threshold of Rydberg series. As can be seen in figure 6.6 the adiabatic passage of a red state through the Stark manifold results in a lower ionisation threshold (point A) compared to the pure diabatic passage (point B). This is caused by the suppression of the Stark shift of the state due to the avoided crossing. So a smaller ionisation threshold of a Rydberg series compared to the classical ionisation limit, indicates an adiabatic passage during the ionisation process.

## 6.3. Measuring the field ionisation threshold of ytterbium Rydberg atoms

Here we describe our experimental efforts to determine the ionisation threshold of various ytterbium Rydberg states. The field ionisation threshold is measured by using the experiment pattern, shown in figure 6.7. A detailed schematic of the high voltage pulse pattern is shown in figure 3.12. For the determination of the threshold, the Rydberg laser is scanned over the Rydberg state. More precisely, for each electric field value the Rydberg laser is scanned

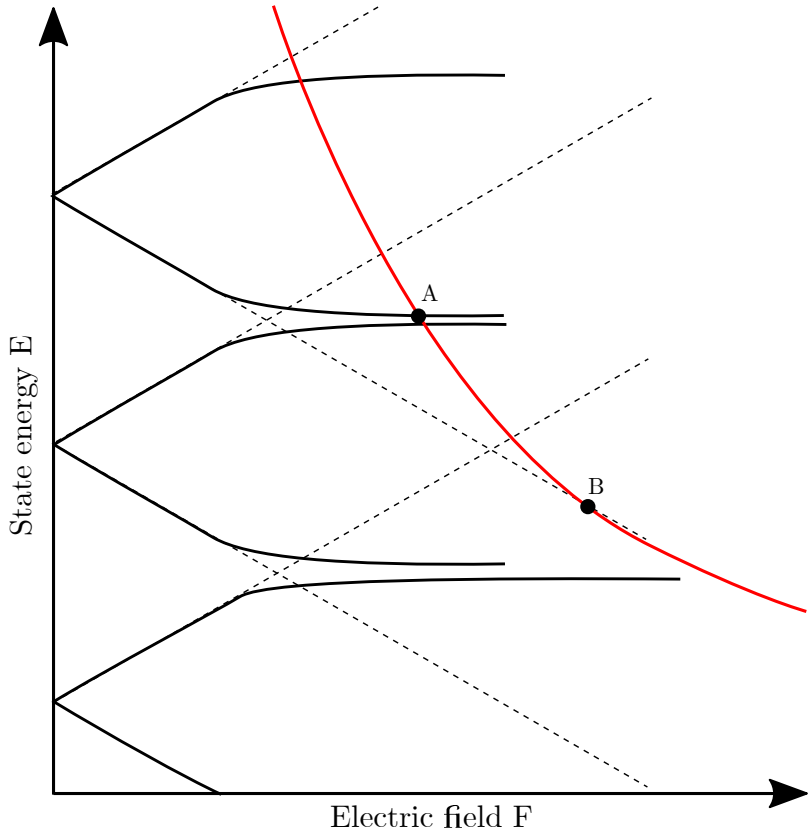


**Figure 6.6.:** *Sketch of the ionisation passage of a Rydberg state. The dashed lines are the state energies of blue and red states. They represent a pure diabatic passage of the state. The solid lines represent a maximally adibatic passage. The shift of the Rydberg state is suppressed at the point where the avoided crossing of the states first appear. The red line represents the ionisation threshold. At point A the adiabtic passage is ionizing, where at point B the diabatic passage reaches the ionisation threshold.*

over the Rydberg state and the ion count per 100 iterations of the high voltage pattern is measured. The amplitude of the ionisation pulse is changed from 13 V/cm to 192 V/cm for each state. The maximum ion count for each electric field is determined, which results in an ionisation threshold measurement, where some results for the $^1S_0$ and $^1D_2$ Rydberg series are shown in figure 6.8. For comparison, the ionisation rate for each $n$ is normalized to the ionisation rate at maximal electric field. As can be seen in figure 6.8 the number of detected ions increases smoothly over a range of $\approx 10$ V/cm. Therefore the ionisation threshold can not be determined unambiguously. The ionisation threshold of each state is assigned to the electric field, where 50% of the maximal ionisation signal is reached. The decrease of the ionisation signal after reaching the ionisation threshold is universal for all

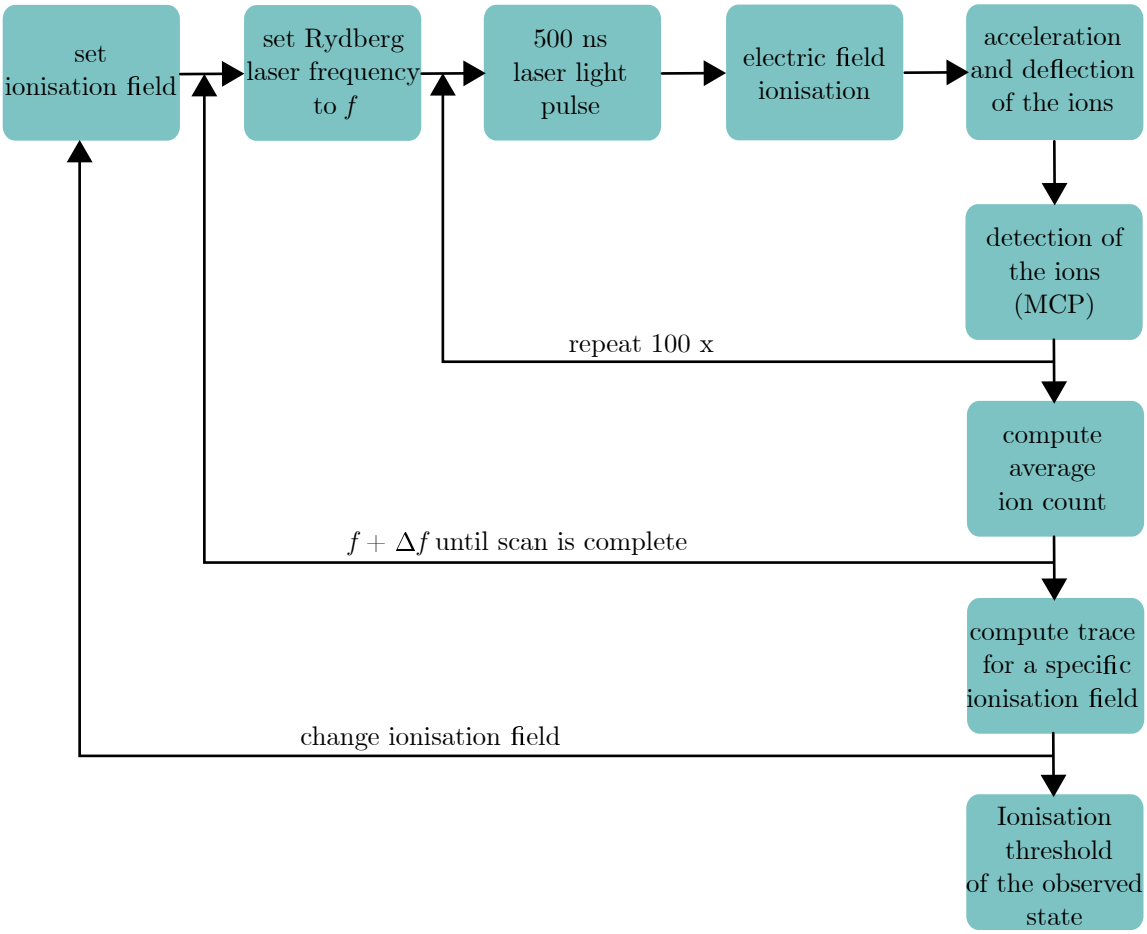


**Figure 6.7.:** *Experimental sequence of the ionisation threshold measurement. The amplitude of the ionisation field is limited by the apparatus from* 13 V/cm *to* 192 V/cm. *The frequency of the Rydberg laser is scanned over the Rydberg transition to compensate frequency drifts of the Rydberg laser. To minimize the error, the measurement is repeated 100 times per Rydberg laser frequency and ionisation field.*

states. This implies, that the decrease of the ionisation signal is caused by an effect, which acts after the ionisation and is therefore attributed the acceleration of the ytterbium ions caused by the ionisation pulse itself. This initial acceleration is not directed to the MCP and has to be therefore compensated by subsequently high pulses (see section 3.2.5). The influence of the first acceleration to the trajectories, increases with increasing electric field of the ionisation pulse. This leads to a decrease of the ion signal, which is universal for all Rydberg states. This effect has to be considered by the determination of electric field ionisation threshold, especially for the low $n$ states where the ionisation field is high and so the effect of the first acceleration.

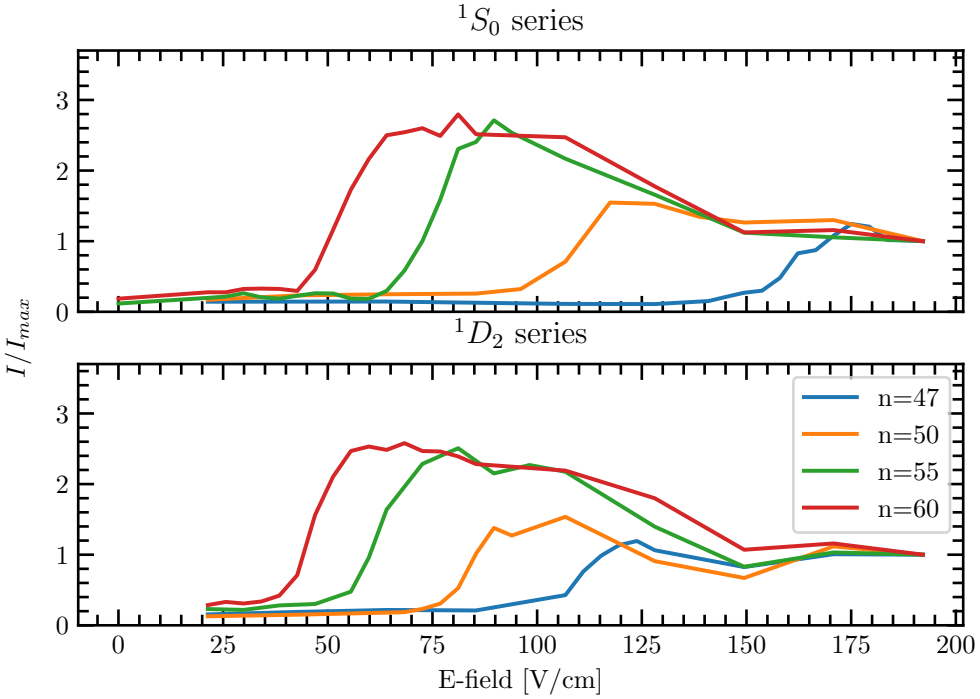


**Figure 6.8.:** *Ionisation signals of $^1S_0$ and $^1D_2$ Rydberg series versus the ionisation field. Each graph is normalized to ionisation rate with the maximal ionisation field. The scaling factor from chapter 3.2.5 was used to determine the electric field. The ionisation limit is computed from the data by determining the field where the ion reaches 50% of its maximal value.*

The ionisation threshold for $^1S_0$ and $^1D_2$ Rydberg series is shown in figure 6.9. The error is estimated by considering the uncertainty of the electric field of the ionisation pulse (see section 3.2.3) and the uncertainty of the threshold measurement itself (see above). The shown classical ionisation limit corresponds to lower limit from equation 6.14. As already described in section 6.2.1 the slew rate of the electric field is important for the ionisation process. The ionisation pulses for these measurements have a rise time of a few nano seconds, which leads to a maximal slew rate of the electric field of $2 \times 10^{10}$ V/cms. Since, to our knowledge, there are no pulsed ionization measurements with Yb, we can only use other elements to classify the slew rate. According to [89] S, P and D Rydberg states of sodium ionize adiabatic for this slew rate. Since the measured ionisation threshold of the s and d states are below the classical ionisation limit, the ionisation passage for both series are not purely diabatic. A purely diabatic passage would result in a ionisation limit which

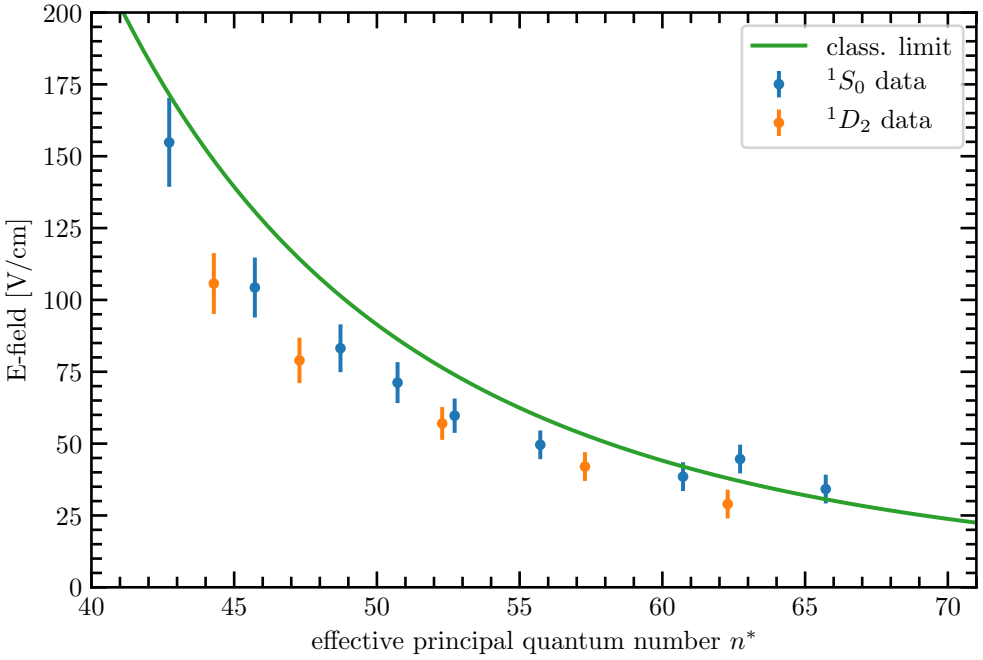


**Figure 6.9.:** *Ionisation threshold of the $^1S_0$ and $^1D_2$ Rydberg series in the range of $n = 45$ to $n = 70$. The error are taken from the electric field uncertainty derived in section 3.2.3. The ionisation limit is taken from equation 6.14.*

agrees with the ionisation limit of the hydrogen atom.

Since the passage also depends on the energy gap $\Delta E$ between the two crossing states, the characteristic of the passage can change from adiabatic to diabatic in the overall ionisation process. The whole ionisation process therefore consists of adiabatic and diabatic passages. This is also reflected by the increase of the ionisation limit for the s states above $n = 65$. This change of the ionisation behavior indicates that the proportion of the diabatic passages increases compared to adiabatic passages, which results from the scaling of the energy gap $\Delta E \propto \delta_l / n^4$. In general the ionisation of Rydberg atoms is a complex process, which depends on the slew rate of the electric field and the behavior of the stark manifold. With our measurements, only qualitative conclusions can be drawn about the ionization process.

# 7.

# Lifetime of ytterbium Rydberg states

The radiative lifetime of a Rydberg state in an ultra cold gas is dominated by two mechanisms, the spontaneous decay and the coupling to the black body radiation [1]. The spontaneous decay rate $\Gamma_0 = 1/\tau_0$ is intrinsic to the energy structure of the Rydberg atom and its general behavior is described in section 7.1. The impact of the black body radiation on the lifetime depends on the temperature of the environment, in which the Rydberg atoms are prepared. The black body radiation induced decay rate is discussed in section 7.2. The sum of theses two effects gives the total effective decay rate

$$\Gamma_{eff}(T) = \Gamma_0 + \Gamma_{BBR}(T) \ , \tag{7.1}$$

which is the quantity that is accessible in a typical experiment. In section 7.3 a measurement of the effective lifetime for ytterbium Rydberg states is presented and compared with theoretical predictions.

## 7.1. Natural lifetime of Rydberg states

The bare lifetime of a Rydberg state at a hypothetical temperature of 0 K is determined by the Einstein Coefficient $\mathcal{A}$ [1]. The coefficient $\mathcal{A}_{nl\to n'l'}$ defines the spontaneous decay from the state $nl$ to a lower lying state $n'l'$ and is given by,

$$\mathcal{A}_{nl\to n'l'} = \frac{4e^2\omega^3_{nl,n'l'}}{3\hbar c^3}\frac{l_{max}}{2l+1}\mathcal{R}^2_{nl\to n'l'} \ . \tag{7.2}$$

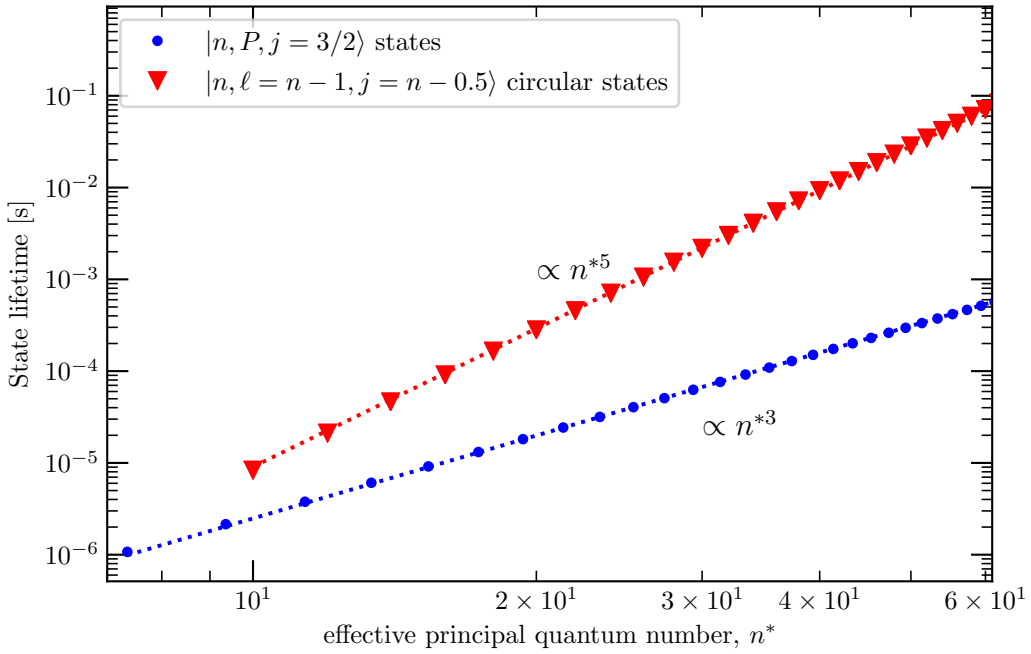


**Figure 7.1.:** *Lifetime scaling of $|n, P, j = 3/2\rangle$ and $|n, \ell = n - 1, j = n - 0.5\rangle$ states in Rubidium. The lifetimes are calculated with the python packages ARC [62].*

Where $\mathcal{R}_{nl \to n'l'}$ is the dipole matrix element between the the $nl$ and $n'l'$ state. The total decay rate of Rydberg state is given by,

$$\Gamma_0 = \sum_{n'l'} \mathcal{A}_{nl \to n'l'}. \tag{7.3}$$

Where the sum is over all dipole coupled states with an energy $E_{n'l'} < E_{nl}$. Since the overlap between neighbouring states is much larger than between the excited state and the ground state (e.g. for Cs $\langle 60S_{1/2}|er|60P_{3/2}\rangle = 4114\, ea_0$ compared to $\langle 6S_{1/2}|er|60P_{3/2}\rangle = 0.003\, ea_0$ [62]), one could assume that the decay into energetically close states dominates the decay rate of a Rydberg state. However, due to the prefactor of $\omega^3_{nl,n'l'}$ decay into the lowest level dominates the decay of a Rydberg state. More precisely this is generally the decay to the lowest lying state with $l - 1$, with the exception of $S$ Rydberg states where the dominant transition is to the lowest $P$ state.

For large $n$ the largest possible transition frequency difference approaches a constant.

Therefore the decay rate for high n scales only with the radial matrix elements between the Rydberg state and the ground state (see equation 7.2). In other words, it only depends on the spatial overlap between the Rydberg wavefunction and the wavefunction of the lowest state. Considering $\langle n^{'} l^{'} | r | nl \rangle \propto n^{*2}$ and the normalization of the Rydberg wavefunction, the corresponding radial matrix element exhibits a $n^{*-3}$ scaling. Therefore the lifetime of low l Rydberg states scales with,

$$\tau_{nl} \quad \propto \quad n^{*3} \,. \tag{7.4}$$

For high l states this assumption does not apply, because the only allowed transition from the $l = n - 1$ state is into the $n^{'} = n - 1$, $l^{'} = n - 2$ state. This means that the highest frequency transition is not constant and contributes to the decay rate with a scaling of $1/n^{*3}$ [1]. Together with the scaling of the size between the states $\langle n^{'} l^{'} | r | nl \rangle \propto n^{*2}$, this results in a scaling of

$$\tau_{nl=n-1} \quad \propto \quad n^{*5} \,. \tag{7.5}$$

In figure 7.1 the lifetime of $P$ and circular states of rubidium Rydberg atoms is shown. We have chosen rubidium as an example to demonstrate the scaling of the lifetime instead of ytterbium, because Rb is commonly used in Rydberg physics and therefore well understood. Ytterbium with its two valence electrons is a more complex system and as can be seen in section 7.3 the methods used to calculated the lifetime of the alkali Rydberg states cannot be transferred one-to-one to ytterbium Rydberg states. The lifetime of every state was calculated using equation 7.3 and the python package *ARC* [62]. As can be seen, the lifetime of $P$ states follows the scaling for low-l states 7.4 while the lifetime of the high-l circular states follows the scaling of equation 7.5. The natural lifetime of the circular states is also at least one order of magnitude higher than the lifetime of the $P$ states. However, the natural lifetime of the Rydberg states is difficult to measure experimentally because the black body radiation of the environment strongly influences the lifetime. This will be discussed in more detail in the section 7.2.

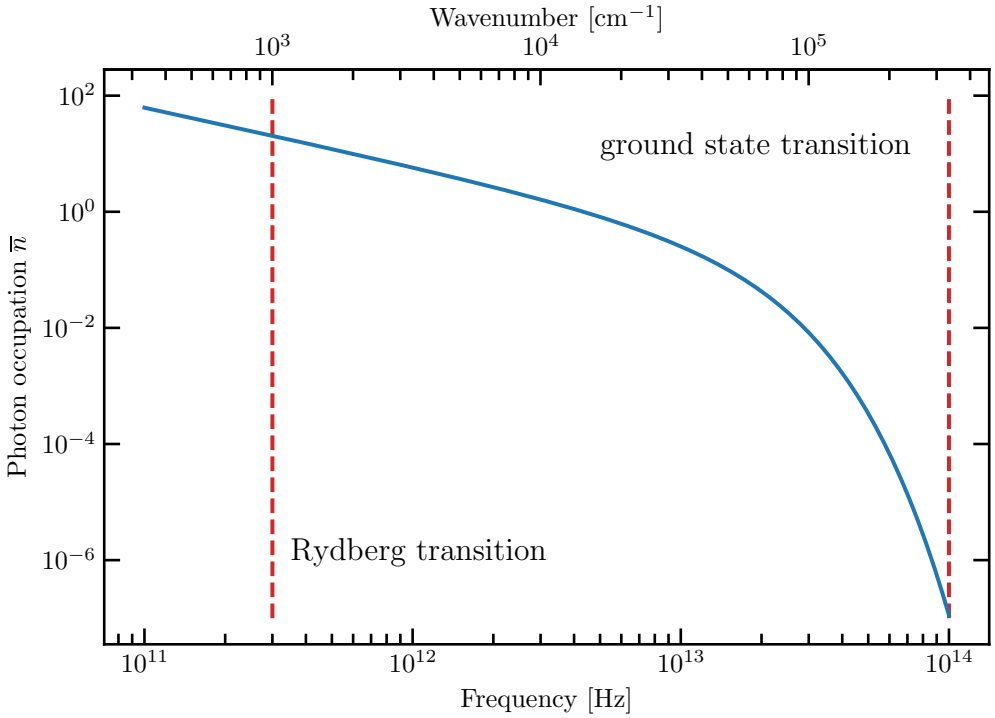


**Figure 7.2.:** *Photon occupation $\overline{n}$ of a 300 K thermal radiation spectrum. Red dashed lines indicate two different transition regions for a Rydberg state. The transition between neighboring Rydberg states at $\nu = 3 \times 10^{11}$ Hz and the transition into a ground state at $\nu = 3 \times 10^{14}$ Hz.*

## 7.2. Black-body radiation

As already mentioned, due to the thermal environment in which the Rydberg atoms are prepared the black-body radiation plays an important role for the experimental lifetime of the Rydberg states. The black-body radiation causes stimulated transitions to neighboring Rydberg states. To calculate the effect of theses transitions in the GHz to THz range on the lifetime of the states, it is convenient to look at the photon occupation numbers $\overline{n}$ of the thermal spectrum, which give the number of photons per mode of the radiation field. The following equation applies to the occupation number [1],

$$\overline{n} = \frac{1}{\exp\left(h\nu/kT\right) - 1} \tag{7.6}$$

Here $T$ is the temperature of the black body (i.e. experimental chamber). In figure 7.2 the dependence of the occupation number $\overline{n}$ on the frequency $\nu$ is shown. It shows that for a

temperature of 300 K the photon number in the Rydberg transition region ($\nu \approx 3 \times 10^{11}$ Hz) is approximately six orders of magnitude larger than for transitions to the ground state ($\nu \approx 3 \times 10^{14}$ Hz).

Therefore black-body stimulated transitions into neighboring Rydberg states become significant compared to stimulated transitions into the ground state. The stimulated transition rate due to the black-body radiation may be calculated using (taken from [90]),

$$\Gamma_{BBR} = \sum_{n'l'} \frac{\mathcal{A}_{nl \to n'l'}}{\exp(h\nu/kT) - 1}. \tag{7.7}$$

Figure 7.3 illustrates the effect of the black-body radiation on possible decay channels

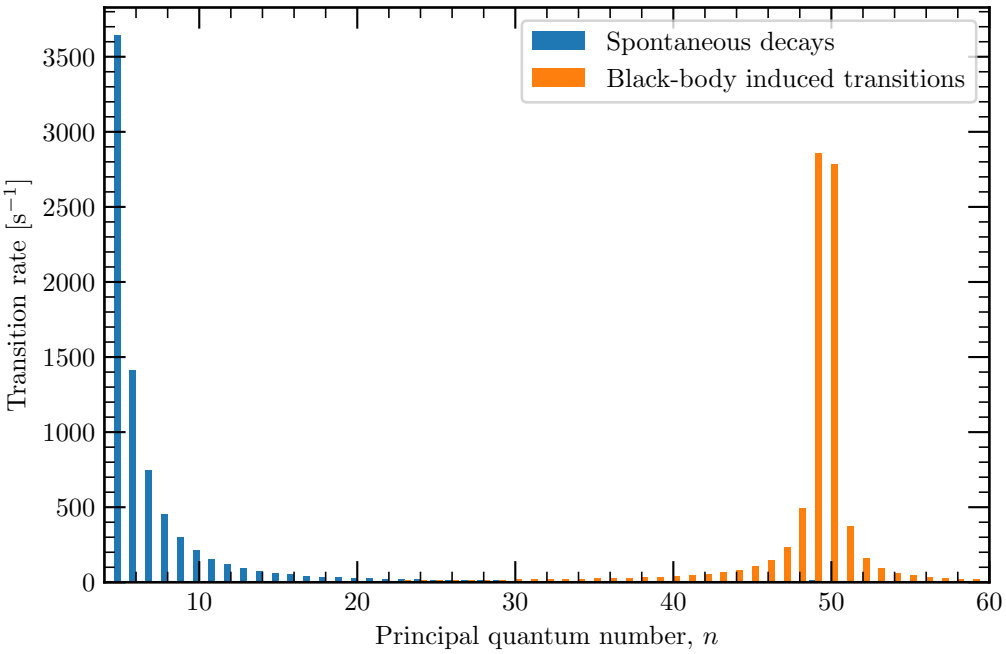


**Figure 7.3.:** *Transition rates for Rb from $50S_{1/2}$ to $n\,P_{1/2,3/2}$ state. Blue bars are the transition rates at 0 K. The orange bars are the black-body transition rates for 300 K. Spontaneous decay is dominated by decay into the lowest energy states, where as the black body radiation drives mostly transitions into neighboring Rydberg states. The figure is created with and inspired by [62].*

from the $50S_{1/2}$ state of rubidium into low lying states. The blue bars show the natural transitions rate from the $50S_{1/2}$ to $n\,P_{1/2,3/2}$, as described in section 7.1. The orange

bars show the black-body induced transition rate for $50S_{1/2}$ to $n\,P_{1/2,3/2}$ at 300 K. The black-body driven decay of the $50S_{1/2}$ state is dominated by decay into the neighboring Rydberg states, as discussed. It should be noted, that the black body radiation can drive transition to higher principal quantum numbers, which is not possible via a spontaneous decay.

In conclusion, the lifetime of a Rydberg state is determined by the spontaneous decay and the black-body radiation driven transition into neighboring and can be written as,

$$\frac{1}{\tau_{eff}} = \frac{1}{\tau_0} + \frac{1}{\tau_{BBR}}\,. \tag{7.8}$$

Figure 7.4 demonstrates the effect of the black body radiation on the lifetime of the $n\,P_{1/2}$ states in Rubidium. The logarithmic plot shows significant reduction of the lifetime with increasing effective quantum number. Thus, for the lifetime of Rydberg states with a high principal quantum the black body radiation becomes the limiting factor.

The behavior of the lifetime of Rydberg states in Ytterbium differs from alkali metal atoms, like Rubidium. The second valence electron changes the scattering between the wavefunction of Rydberg electron and the core potential. To model this system one would have to consider has to consider the MQDT (see chapter 2.2.2). The different channels which are introduced in the model influence the calculated lifetime of the Rydberg states. A detailed description for the implementation of MQDT into the *ab initio* calculation of the lifetime in Strontium (which is a two-electron atom) can be found in [91]. For the implementation it is crucial to fit the model to experimental data of several Rydberg series.

## 7.3. Lifetime of Ytterbium Rydberg states

In the following we present a preliminary measurement of the lifetime of the $^1S_0$ and $^1D_2$ series in Yb. To measure the lifetime of the Rydberg states in Yb we use the MCP and the electrode setup described in section 3.1. The time pattern of the light and the high voltage pulses is described in figure 7.5. To measure the lifetime, a delay is introduced between the excitation light pulse and the ionisation pulse. The voltage of the ionization pulse is chosen such that the electric field is large enough to ionize the observed state (see chapter 6). To

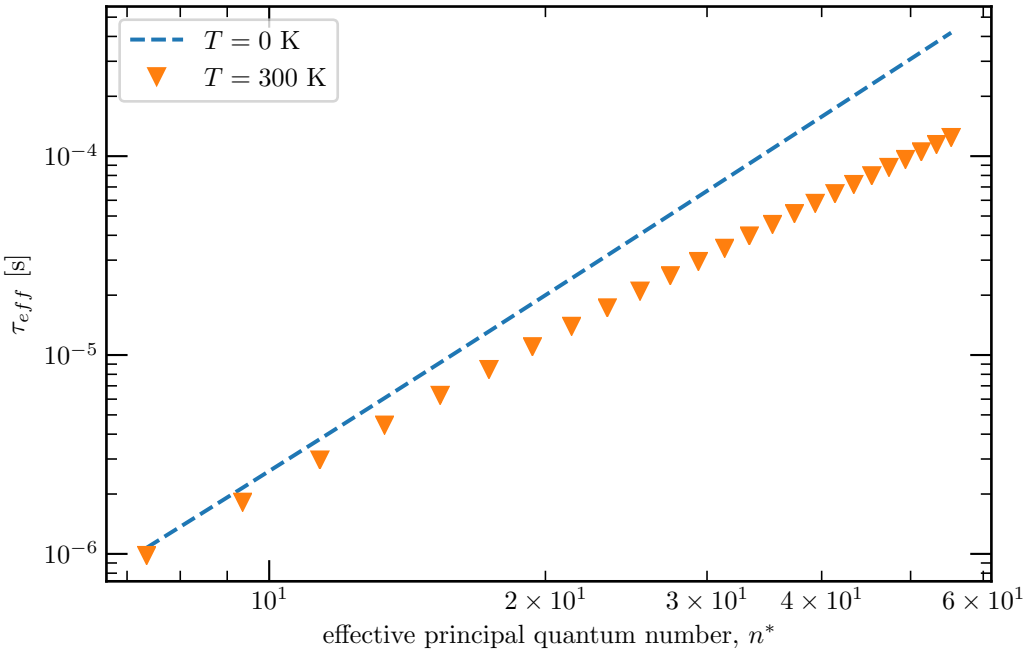


**Figure 7.4.:** *Difference in effective lifetime of the $n\,P_{1/2}$ state in Rubidium for $T = 0\,\mathrm{K}$ and $T = 300\,\mathrm{K}$. The black-body radiation reduces the lifetime with increasing principal quantum number. At $T = 300\,\mathrm{K}$ the lifetime no longer follows the $n^{*3}$ scaling. The figure is done with [62].*

reduce the statistical error from counting, the pulse pattern is repeated one hundred times and the ion count is averaged over all cycles. To compensate fluctuations of the Rydberg laser frequency we scan the Rydberg laser over the Rydberg transition for every chosen time delay between the light pulse and the high voltage pulses.

As can be seen in figure 7.6 we observe an exponential decay of the ion count as a function of the delay between the light pulse and the ionisation pulse. An exponential decay fit yields a lifetime of the ion signal. However, the measured lifetime is not the pure radiative lifetime of the examined state. As described in section 7.2, the black-body radiation due to the room-temperature environment induces a decay of the examined state into neighboring Rydberg states and since we cannot ionize state selectively with the electric field pulse, we measure with this method the lifetime of all states, which are populated by black-body radiation.

For every measurement it is also necessary to compensate the electric stray field, because

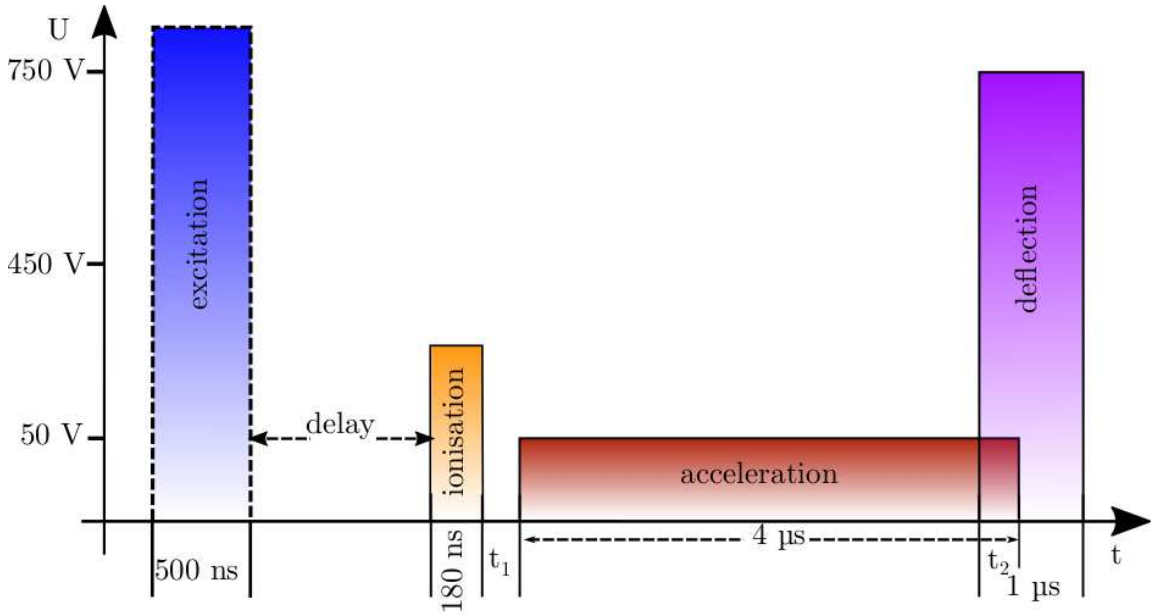


**Figure 7.5.:** *Time profile of the high voltage pulses and the light pulse for the lifetime measurement of the Rydberg atoms. For the lifetime measurement a variable time delay is introduced between the light pulse for Rydberg excitation and the electric field pulse for ionisation. The technical caused delay $t_1$ between ionisation pulse (yellow) and acceleration pulse (red) is* 330 ns. *The overlap $t_2$ between the acceleration pulse an the deflection pulse (purple) is* 570 ns. *The ionisation pulse is set to an amplitude, which is sufficient for the ionisation of examined state. The ionisation pulse and the acceleration pulse are applied to the plate electrode. The deflection pulse is applied to segment one, see figure 3.10.*

otherwise it causes a mixing of the Rydberg states, which has a big influence on the measured lifetime. In figure 7.7, the measured lifetime of the $^1S_0$ and $^1D_2$ series in the range from $n = 40$ to $n = 80$ is shown. The error for every measurement is taken from the exponential fit to the decay of the ion signal as a function of the delay of the ionisation pulse. For comparison, the calculated natural lifetime of the $^2S_{1/2}$ series in rubidium is also shown in the figure. We compare the measured lifetime to the natural lifetime of Rubidium not to the black-body reduced lifetime because with field ionisation method we measure the lifetime of all states, which are populated by the black-body radiation. Therefore, we measure a combined natural lifetime of these states rather than the lifetime of the examined state. As can be seen, the measured lifetime of the two ytterbium series are well below the natural lifetime of the $^2S_{1/2}$ series in Rubidium. This reduction of the lifetime compared to an atom with one valence electron could be caused by the larger extension of the core potential, due to the second valence electron. Furthermore there is an indication that the

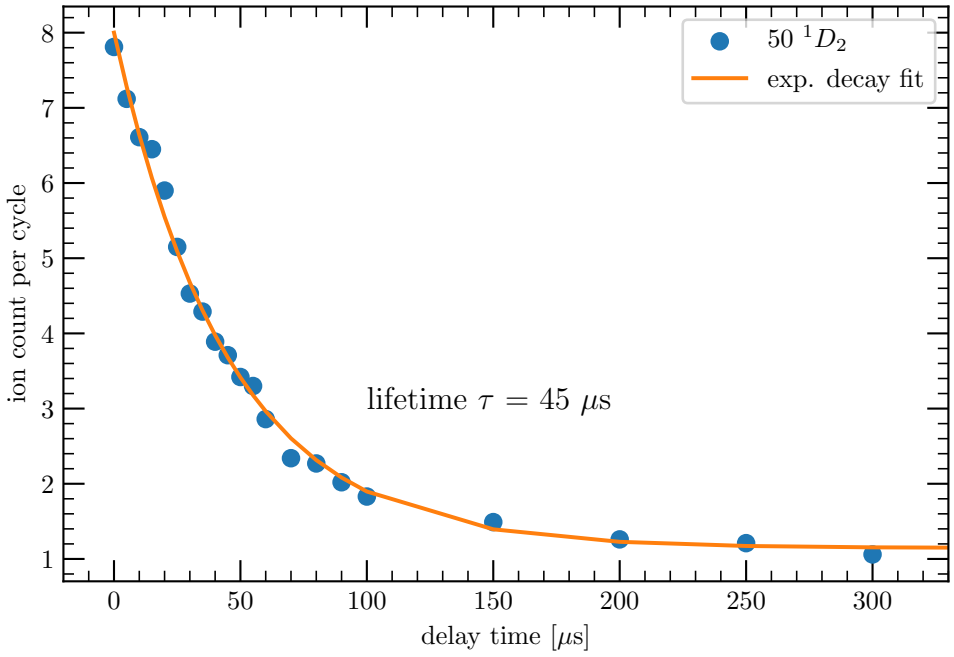


**Figure 7.6.:** *Measurement of the lifetime of the* $50\,^1D_2$ *state. Orange line is an exponential decay fit to the data. The ion count is averaged over one hundred repetition cycles.*

lifetime in the $^1D_2$ series saturates for large $n$. As described before, this saturation is due to the relevance of the black-body induced decay for large $n$. Since the number of states, that are dipole coupled to the $^1D_2$ series is bigger than to $^1S_0$ series, the effect of the black body radiation to the lifetime is stronger in $^1D_2$ series, which could explain the observation. With a further development of this measuring method, which makes it possible to ionize state-specifically, one could measure the specific radiative lifetime of a Rydberg state. This further development could be, for example, another laser that excites the second valence electron and thus causes auto-ionization (see reference [19]). Using these lifetimes, one could then test an MQDT model of ytterbium, like the model developed in the references [7, 76].

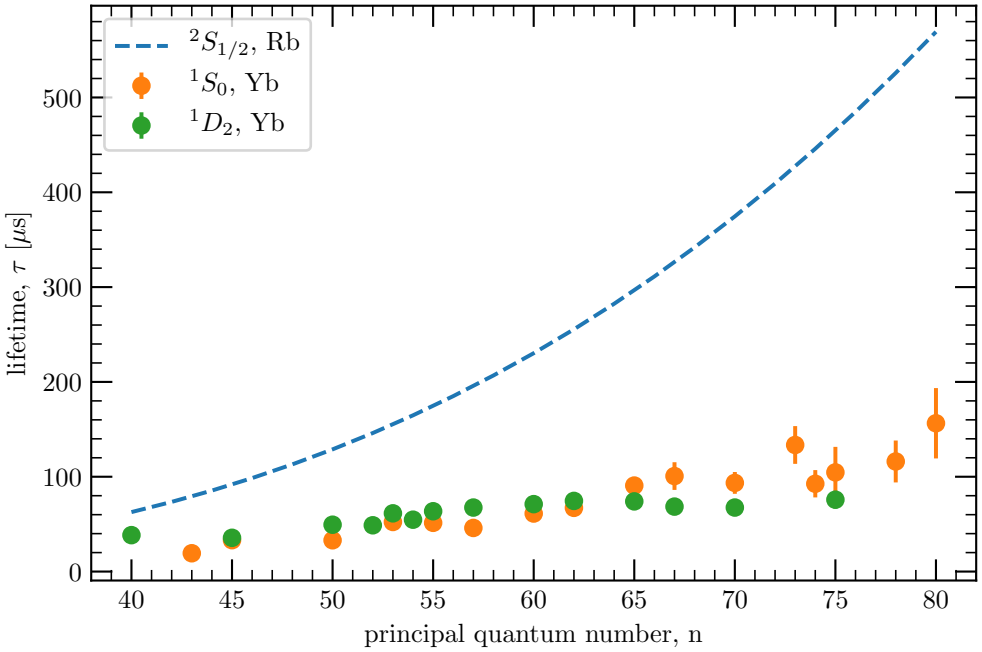


**Figure 7.7.:** *Lifetime of the $^1S_0$ and $^1D_2$ series in Ytterbium. The dashed line is a ab initio calculation of the natural lifetime of the $^2S_{1/2}$ series. The calculation is done with [62].*

# 8.

# Discussion and outlook

In this thesis we have described the setup of a new apparatus to explore Rydberg states in an ultra cold ytterbium gas. The apparatus can produce up to $1 \times 10^7$ ytterbium atoms in a magneto optical trap and simultaneous cool the ensemble to a temperature of $\approx 3.8 \pm 1.1\,\mathrm{mK}$. We developed various techniques and methods unique for Ytterbium. A simple and robust spectroscopy was build to frequency stabilize the cooling lasers for the MOT. The setup also offers the possibility for a two-color spectroscopy, which can be used to simultaneously stabilize an additional laser system on the ${}^1S_0 \rightarrow {}^3P_1$ transition.

We have implemented a MOT depletion spectroscopy to study a wide range of Rydberg states of Ytterbium. Unique for this method is its simplicity and robustness. Compared to the standard detection methods of Rydberg atoms this method has no need of an ion detector or a complex electrode setup, which create large electric fields. With the MOT depletion technique it was possible to excite and identify several Rydberg states which had not been measured before and confirm already identified states from a previous study of a French group in Paris [7].

As an application of the MOT depletion method the polarizabilities of ${}^1S_0$ and ${}^1P_1$ Rydberg series have been determined. With the results of this study a semi-classical approach for calculating the dipole matrix elements of Yb Rydberg states was tested. We found that the approach is consistent with the measurements.

With the setup of the second stage of the experimental study it was possible to

implement field-ionization as an additional technique for the detection of Rydberg atoms. The ionisation threshold for the field ionisation of the $^1S_0$ and $^1D_2$ Yb Rydberg series was determined. By comparing the threshold with the classical ionisation limit it was possible to explore the ionisation process of the $^1S_0$ and $^1D_2$ Yb Rydberg series, which consist of diabatic and adiabatic passages through the Stark manifold.

The electric field ionisation method also allowed to measure the lifetime of several Rydberg series, by introducing a delay between the Rydberg excitation and the field ionisation. With this method it was possible to measure the black-body reduced lifetimes of several Rydberg states in the $^1S_0$ and $^1D_2$ series. The comparison to the alkali metal Rubidium shows that the lifetime of both series lies below the lifetime of the $^2S_{1/2}$ series in Rubidium which could be caused by the influence of the second valence electron. The lifetime of $^1D_2$ shows a saturation in the high n region ($n > 50$) which could be attributed to a larger loss caused by the black-body radiation of the environment as compared to $^1S_0$ .

One goal of the research project is the observation of long-range interactions between Yb Rydberg atoms, such as the dipole blockade or the generation of ultra cold plasma [21]. The first experimental studies described in this thesis, however were all performed at low density ($10^9\,\mathrm{cm}^{-3}$). Therefore interactions between Rydberg atoms, the regime where the inter-atomic distance plays a role, has not been accessed yet. The next step is to cool the Ytterbium atoms further in a second magneto-optical trap, using the narrow $^1S_0 \rightarrow {}^3P_1$ transition, which allows for an increase of the density by two orders of magnitude. The density of the atom cloud can further be increased by transferring the Yb atoms into an optical dipole trap, like e.g. the two dimensional optical lattice, which can be realized using the already implemented intra-vacuum resonator. In this trap the mean distance of the atom ensemble is so small, that interactions become important. It will be even possible to condensate the bosonic isotopes of ytterbium into a BEC. With these prerequisites our experimental apparatus forms an ideal starting-point for exploring the dynamics of Yb Rydberg many-body system.

A possible study that can be pursued is the spatial measurement of the Rydberg

excitation. So far only a few imaging techniques are available to detect Rydberg atoms spatially. One possibility is to spatially image the Rydberg atoms indirect with a field ion microscope, which was demonstrated by Schwarzkopf et al. [43]. A more direct imaging technique was shown by Bloch et al. [92], where the Rydberg atoms are detected optically with high-resolution fluorescence imaging. The fluorescence is induced by de-exciting the Rydberg atoms to a short-lifetime intermediate state. Another state-of-the-art imaging technique is the interaction enhanced absorption imaging which was used by [93] to image Rydberg $P$ states in Rubidium. A unique property of the divalent Yb atom, namely optically induced autoionisation, is ideally suited for spatially resolved detection. As shown by [19] Rydberg states in a divalent atom autoionize when the second valence electron is excited. Using a tightly focussed laser beam, the excitation of the second electron may ionize Yb Rydberg atoms. Combined with an optical dipole trap this could be used to spatially resolve the Rydberg excitation and its time evolution without the need of an ion microscope or a complex coupling scheme.

Another interesting option for Yb Rydberg atoms is to use the optically active core to trap and cool the atoms even after the Rydberg excitation. This approach could be used to capture circular Rydberg states. They can be captured and cooled because they are impervious to autoionization, which has already been shown for strontium [6]. With their ultra long coherence time these states are particularly appealing for emerging quantum technologies [94] and ytterbium like strontium with its divalent nature is an ideal candidate for creating circular Rydberg states.

A possible future application for ytterbium Rydberg excitation arises from another experiment of our research group, which deals with mixtures of Rb and Yb atoms. Combining this experiment with Rydberg excitation could lead to a fascinating new class of ultra cold giant molecules with an exotic potential structure [95]. This new molecules class is extremely sensitive to external electric fields. Only small electric fields are needed to influence the electronic structure significantly [96]. Therefore, such molecules could be used as a probe for tiny electric fields.

# A.

# Appendix

## 1. Rydberg-Ritz fit parameters

The Rydberg-Ritz parameters are used for the theoretical determined energy levels of the $6sns^1S_0$ and $6sns^1P_1$ Rydberg series in the chapter 4. They are also used for the theoretical determination of the polarizability of the $6sns^1S_0$ and $6sns^1P_1$ Rydberg series in chapter 5.

**Table A.1.:** The Rydberg-Ritz parameters for the $6sns^1S_0$, $6sns^1D_2$ and $6sns^3D_2$ are taken from [7]. The remaining parameters are taken from fits to spectroscopy data, published in [76]

| Series | $\delta_0$ | $\delta_1$ | $\delta_2$ | $\delta_3$ | $\delta_4$ | $\delta_5$ |
|---|---|---|---|---|---|---|
| $6sns^1S_0$ | 4.278337 | -5.625 | 91.65 | -156050 | -49725000 | 1.1021e+10 |
| $6sns^1P_1$ | 3.95601286 | -30.8616930 | 60222.3884 | -76358128.9 | 3.6197e+10 | – |
| $6sns^3P_1$ | 4.81175803 | -315.289309 | 57586.9587 | -2.4924e+09 | 2.3725e+12 | – |
| $6sns^3P_2$ | 3.92562725 | -8.33773066 | 602.823896 | – | – | – |
| $6sns^1D_2$ | 2.713094 | -1.8646 | -2145.5 | 3940500 | -3103600000 | 1.069e+12 |
| $6sns^3D_2$ | 2.748679 | -0.5200 | -1186.01 | 1564600 | -981340000 | 2426e+11 |
| $6sns^1F_3$ | 1.28169811 | -16.8480354 | 806.185504 | – | – | – |
| $6sns^3F_3$ | 1.06342553 | -6.66067129 | -1190.80245 | – | – | – |

## 2. Spectroscopic data

**Table A.2.:** Measured energy levels of the $6sns^1S_0$ Rydberg series of $^{174}Yb$ in the range of $n = 70$ to 90. $E_{exp}$ are the measured energy values for the Rydberg states. $E_{ref}$ is taken from [7]. Energy levels with full circle are determined with the corresponding Rydberg-Ritz parameters from table A.1. The comparison between the measurement and the Reference leads to an absolute frequency error of 64 Mhz. $\alpha$ is the ratio of the experimental polarizability and the polarizability of the $6s70s^1S_0$ state.

| Assignment | $E_{exp}\,(cm^{-1})$ | $E_{ref}\,(cm^{-1})$ | $E_{exp} - E_{ref}\,(MHz)$ | $\alpha$ | Q. Defect |
|---|---|---|---|---|---|
| $6s70s^1S_0$ | 50417.6932 | 50417.6654 | | 1.00 | 4.24106 |
| $6s71s^1S_0$ | 50418.4198 | 50418.4212 | -43 | 0.88 | 4.27900 |
| $6s72s^1S_0$ | 50419.1425 | 50419.1438 | -37 | 1.02 | 4.27886 |
| $6s73s^1S_0$ | 50419.8349 | 50419.8350 | -4.0 | 1.18 | 4.27734 |
| $6s74s^1S_0$ | 50420.4973 | 50420.4966 | 17 | 1.37 | 4.27629 |
| $6s75s^1S_0$ | 50421.1363 | 50421.1305 | 173 | 1.80 | 4.26793 |
| $6s76s^1S_0$ | 50421.7370 | 50421.7379 | -30 | 1.77 | 4.27898 |
| $6s77s^1S_0$ | 50422.3259 | 50422.3208 | 155 | 1.55 | 4.26821 |
| $6s78s^1S_0$ | 50422.8811 | 50422.8797 | 40 | 1.53 | 4.27483 |
| $6s79s^1S_0$ | 50423.4223 | 50423.4164 | 173 | 2.09 | 4.26636 |
| $6s80s^1S_0$ | 50423.9353 | 50423.9322 | 94 | 2,83 | 4.27116 |
| $6s81s^1S_0$ | 50424.4317 | 50424.4278 ● | 116 | 2.45 | 4.26941 |
| $6s82s^1S_0$ | 50424.9074 | 50424.9045 ● | 89 | 2.64 | 4.27107 |
| $6s83s^1S_0$ | 50425.3645 | 50425.3630 ● | 44 | 2.84 | 4.27421 |
| $6s84s^1S_0$ | 50425.8045 | 50425.8045 ● | 2 | 3.54 | 4.27734 |
| $6s85s^1S_0$ | 50426.2281 | 50426.2299 ● | -46 | 3.17 | 4.28115 |
| $6s86s^1S_0$ | 50426.6382 | 50426.6392 ● | -30 | 3.70 | 4.27997 |
| $6s87s^1S_0$ | 50427.0312 | 50427.0341 ● | -85 | 3.92 | 4.28483 |
| $6s88s^1S_0$ | 50427.4132 | 50427.4148 ● | -51 | 4.92 | 4.28208 |
| $6s89s^1S_0$ | 50427.7808 | 50427.7822 ● | -44 | 4.69 | 4.28164 |
| $6s90s^1S_0$ | 50428.1368 | 50428.1368 ● | 1 | 5.60 | 4.27756 |

**Table A.3.:** Measured energies of the $6sns^1P_1$ Rydberg series of $^{174}Yb$ in the range of $n = 70$ to 90. $E_{exp}$ are the measured energy values for the Rydberg states. $E_{ref}$ is taken from [76]. Energy levels with full circle are determined with the corresponding Rydberg-Ritz parameters from table A.1. The comparison between the measurement and the Reference leads to an absolute frequency error of 50 Mhz. $\alpha_1(m_j = 0)$ and $\alpha_2(m_j = 1)$ are the polarizabilities to the polarizability of the $6s70s^1S_0$ state.

| Assignment | $E_{exp}\,(cm^{-1})$ | $E_{ref}\,(cm^{-1})$ | $E_{exp} - E_{ref}\,(MHz)$ | $\alpha_1$ | $\alpha_2$ | Q. Defect |
|---|---|---|---|---|---|---|
| $6s70s^1P_1$ | 50417.9147 | 50417.9154 | -21 | 0.85 | 0.38 | 3.9522 |
| $6s71s^1P_1$ | 50418.6607 | 50418.6602 | 17 | 1.00 | 0.37 | 3.9506 |
| $6s72s^1P_1$ | 50419.3723 | 50419.3723 | 5 | 1.00 | 0.43 | 3.9512 |
| $6s73s^1P_1$ | 50420.0510 | 50420.0537 | -77 | 1.59 | 0.56 | 3.9554 |
| $6s74s^1P_1$ | 50420.7051 | 50420.7061 | -29 | 1.20 | 0.54 | 3.9531 |
| $6s75s^1P_1$ | 50421.3282 | 50421.3312 | -88 | 1.27 | 0.42 | 3.9565 |
| $6s76s^1P_1$ | 50421.9279 | 50421.9305 | -73 | 1.59 | 0.56 | 3.9560 |
| $6s77s^1P_1$ | 50422.5053 | 50422.5051 | -5 | 1.60 | 0.65 | 3.9516 |
| $6s78s^1P_1$ | 50423.0583 | 50423.0568 ● | 47 | 1.78 | 0.63 | 3.9491 |
| $6s79s^1P_1$ | 50423.5880 | 50423.5865 ● | 43 | 2.10 | 0.72 | 3.9493 |
| $6s80s^1P_1$ | 50424.0945 | 50424.0955 ● | -32 | 2.19 | 0.76 | 3.9543 |
| $6s81s^1P_1$ | 50424.5854 | 50424.5849 ● | 17 | 2.65 | 0.79 | 3.9510 |
| $6s82s^1P_1$ | 50425.0527 | 50425.0555 ● | -83 | 3.05 | 1.01 | 3.9583 |
| $6s83s^1P_1$ | 50425.5098 | 50425.5084 ● | 43 | 3.13 | 1.03 | 3.9491 |
| $6s84s^1P_1$ | 50425.9446 | 50425.9444 ● | 5 | 3.22 | 1.02 | 3.9520 |
| $6s85s^1P_1$ | 50426.3638 | 50426.3644 ● | -16 | 3.69 | 1.45 | 3.9539 |
| $6s86s^1P_1$ | 50426.7651 | 50426.7691 ● | -118 | 3.78 | 1.51 | 3.9625 |
| $6s87s^1P_1$ | 50427.1601 | 50427.1593 ● | 24 | 4.41 | 1.45 | 3.9506 |
| $6s88s^1P_1$ | 50427.5321 | 50427.5356 ● | -104 | 4.41 | 1.57 | 3.9622 |
| $6s89s^1P_1$ | 50427.8976 | 50427.8988 ● | -36 | 4.67 | 1.56 | 3.9562 |
| $6s90s^1P_1$ | 50428.2440 | 50428.2493 ● | -160 | 3.80 | 1.07 | 3.9683 |

# 3. Electronic circuits

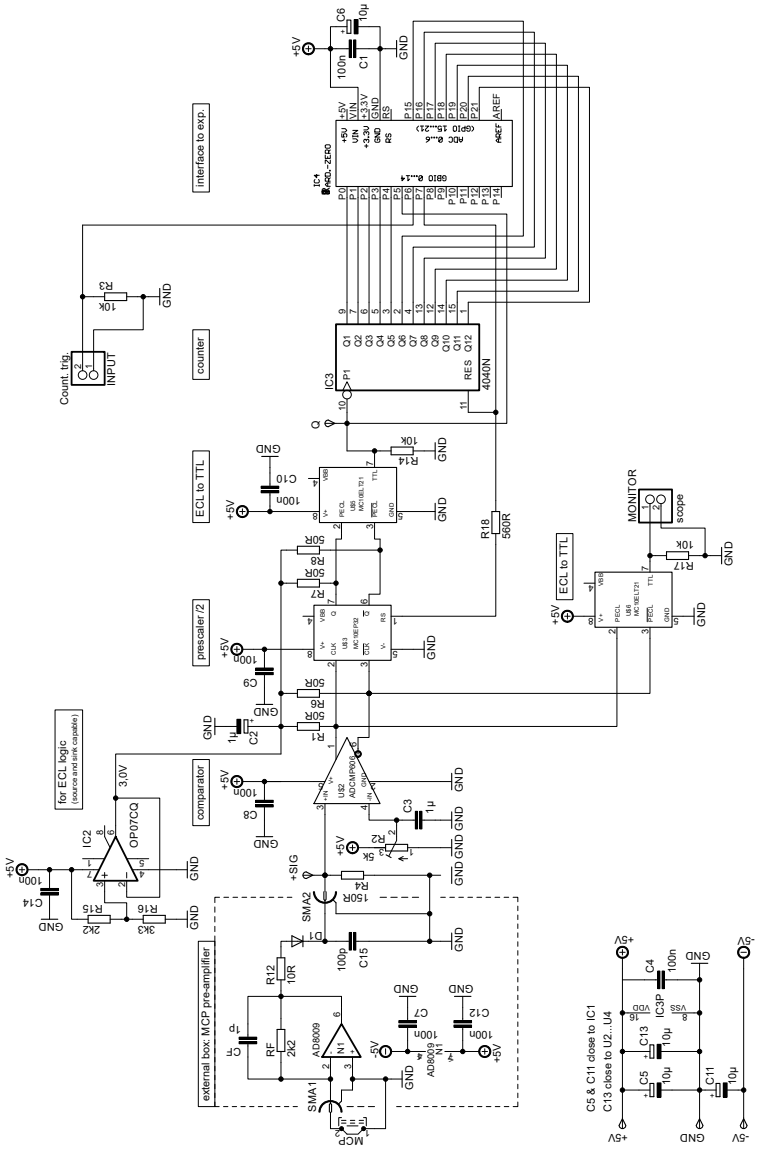


**Figure A.1.:** *Electric circuit diagram for the of the ion signal counter.*

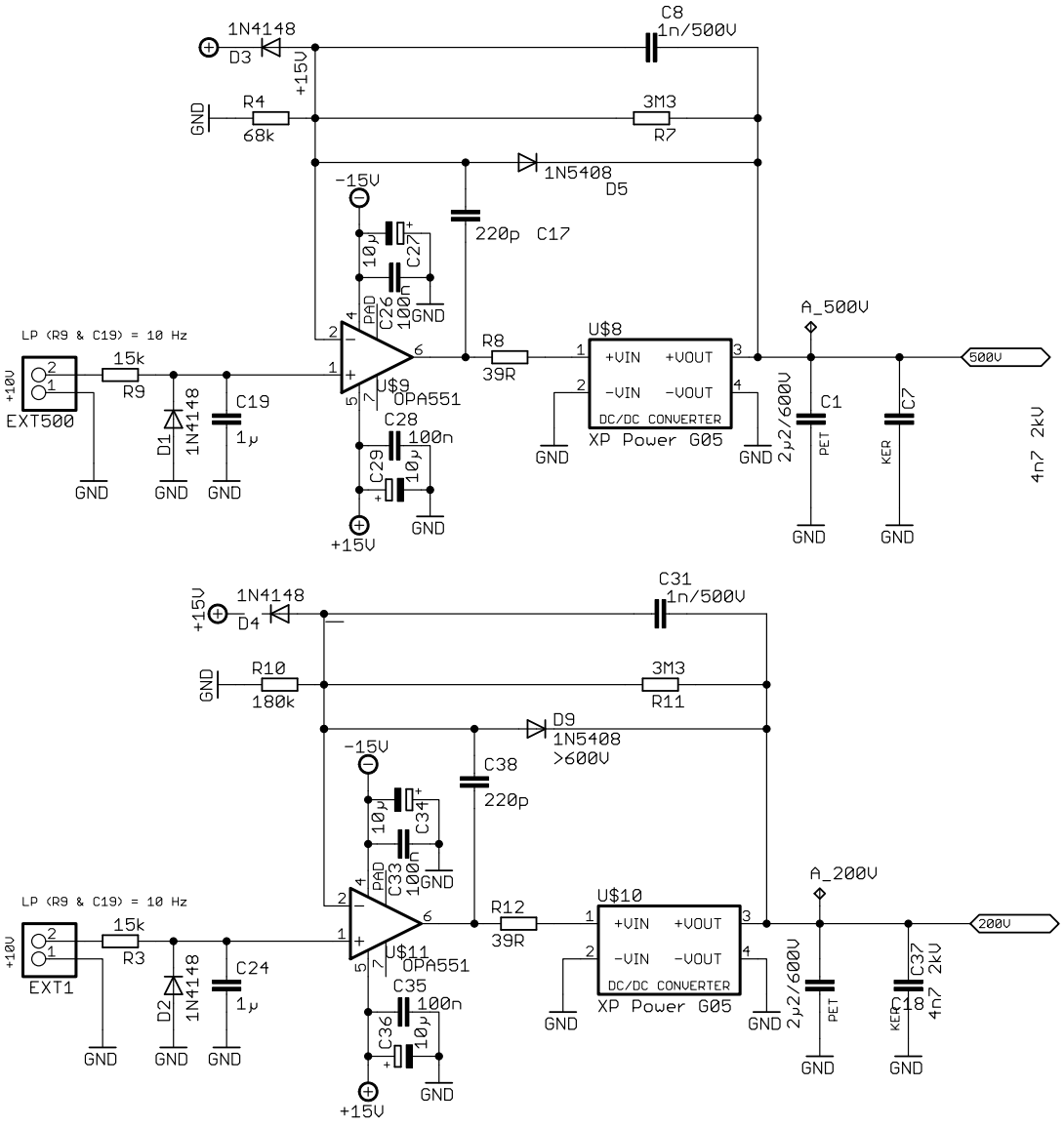


**Figure A.2.:** *Electric circuit diagram of the high voltage switch.*

# Bibliography


[1] Thomas F Gallagher. *Rydberg atoms*. Vol. 3. Cambridge University Press, 2005.

[2] M. Saffman, T. G. Walker, and K. Mølmer. "Quantum information with Rydberg atoms". In: *Rev. Mod. Phys.* 82 (3 2010), pp. 2313–2363. DOI: 10.1103/RevModPhys.82.2313. URL: https://link.aps.org/doi/10.1103/RevModPhys.82.2313.

[3] F. Camargo et al. "Lifetimes of ultralong-range Strontium Rydberg molecules in a dense BEC". In: *Journal of Physics: Conference Series* 875 (2017), p. 082001. DOI: 10.1088/1742-6596/875/9/082001. URL: https://doi.org/10.1088\%2F1742-6596\%2F875\%2F9\%2F082001.

[4] C. E. Simien et al. "Using Absorption Imaging to Study Ion Dynamics in an Ultracold Neutral Plasma". In: *Phys. Rev. Lett.* 92 (14 2004), p. 143001. DOI: 10.1103/PhysRevLett.92.143001. URL: https://link.aps.org/doi/10.1103/PhysRevLett.92.143001.

[5] F. Camargo et al. "Creation of Rydberg Polarons in a Bose Gas". In: *Phys. Rev. Lett.* 120 (8 2018), p. 083401. DOI: 10.1103/PhysRevLett.120.083401. URL: https://link.aps.org/doi/10.1103/PhysRevLett.120.083401.

[6] R. C. Teixeira et al. "Preparation of Long-Lived, Non-Autoionizing Circular Rydberg States of Strontium". In: *Phys. Rev. Lett.* 125 (26 2020), p. 263001. DOI: 10.1103/PhysRevLett.125.263001. URL: https://link.aps.org/doi/10.1103/PhysRevLett.125.263001.

[7] H. Lehec et al. "Laser and microwave spectroscopy of even-parity Rydberg states of neutral ytterbium and multichannel-quantum-defect-theory analysis". In: *Phys. Rev. A* 98 (6 2018), p. 062506. DOI: 10.1103/PhysRevA.98.062506. URL: https://link.aps.org/doi/10.1103/PhysRevA.98.062506.

[8] B. Oumarou et al. "New and rapid method for calculation of electric dipole and quadrupole radial integrals between atomic Rydberg states". In: *Phys. Rev. A* 37 (6 1988), pp. 1885–1894. DOI: 10.1103/PhysRevA.37.1885. URL: https://link.aps.org/doi/10.1103/PhysRevA.37.1885.

[9] P. McQuillen et al. "Imaging the evolution of an ultracold strontium Rydberg gas". In: *Phys. Rev. A* 87 (1 2013), p. 013407. DOI: 10.1103/PhysRevA.87.013407. URL: https://link.aps.org/doi/10.1103/PhysRevA.87.013407.

[10] J. E. Johnson and S. L. Rolston. "Interactions between Rydberg-dressed atoms". In: *Phys. Rev. A* 82 (3 2010), p. 033412. DOI: 10.1103/PhysRevA.82.033412. URL: https://link.aps.org/doi/10.1103/PhysRevA.82.033412.

[11] R Mukherjee et al. “Many-body physics with alkaline-earth Rydberg lattices”. In: *Journal of Physics B: Atomic, Molecular and Optical Physics* 44.18 (2011), p. 184010. DOI: 10.1088/0953-4075/44/18/184010. URL: https://doi.org/10.1088\%2F0953-4075\%2F44\%2F18\%2F184010.

[12] B. Vaucher, S. J. Thwaite, and D. Jaksch. “Ultralarge Rydberg dimers in optical lattices”. In: *Phys. Rev. A* 78 (4 2008), p. 043415. DOI: 10.1103/PhysRevA.78.043415. URL: https://link.aps.org/doi/10.1103/PhysRevA.78.043415.

[13] K. Overstreet, A. Schwettmann, and J. et al Tallant. “Observation of electric-field-induced Cs Rydberg atom macrodimers”. In: *Nature Phys 5* 581–585 (2009) (2009). DOI: https://doi.org/10.1038/nphys1307.

[14] D. Jaksch et al. “Fast Quantum Gates for Neutral Atoms”. In: *Phys. Rev. Lett.* 85 (10 2000), pp. 2208–2211. DOI: 10.1103/PhysRevLett.85.2208. URL: https://link.aps.org/doi/10.1103/PhysRevLett.85.2208.

[15] V. Bendkowsky et al. “Observation of ultralong-range Rydberg molecules”. In: *Nature* 458,7241 (2009). DOI: doi:10.1038/nature07945.

[16] Brendan Wyker et al. “Decoherence of high-l Rydberg wave packets by collisions and electrical noise”. In: *Journal of Physics: Conference Series* 388 (June 2011). DOI: 10.1088/1742-6596/388/3/032003.

[17] Fabian Ripka et al. “A room-temperature single-photon source based on strongly interacting Rydberg atoms”. In: *Science* 362.6413 (2018), pp. 446–449. ISSN: 0036-8075. DOI: 10.1126/science.aau1949. eprint: https://science.sciencemag.org/content/362/6413/446.full.pdf. URL: https://science.sciencemag.org/content/362/6413/446.

[18] B Zygelman. “Recombination and cascade of Rydberg antihydrogen”. In: *Journal of Physics B: Atomic, Molecular and Optical Physics* 38.2 (2005), S387–S400. DOI: 10.1088/0953-4075/38/2/029. URL: https://doi.org/10.1088\%2F0953-4075\%2F38\%2F2\%2F029.

[19] J Millen et al. “Spectroscopy of a cold strontium Rydberg gas”. In: *Journal of Physics B: Atomic, Molecular and Optical Physics* 44.18 (2011), p. 184001. DOI: 10.1088/0953-4075/44/18/184001. URL: https://doi.org/10.1088\%2F0953-4075\%2F44\%2F18\%2F184001.

[20] T. M. Weber et al. “Mesoscopic Rydberg-blockaded ensembles in the superatom regime and beyond”. In: *Nature Physics* 11 (2015), 157–161. DOI: 10.1038/nphys3214. URL: https://doi.org/10.1038/nphys3214.

[21] A D Bounds et al. “Coulomb anti-blockade in a Rydberg gas”. In: *New J. of Phys.* 21 (May 2019). URL: https://doi.org/10.1088/1367-2630/ab1c0e.

[22] L. Isenhower et al. “Demonstration of a Neutral Atom Controlled-NOT Quantum Gate”. In: *Phys. Rev. Lett.* 104 (1 2010), p. 010503. DOI: 10.1103/PhysRevLett.104.010503. URL: https://link.aps.org/doi/10.1103/PhysRevLett.104.010503.

[23] X. L. Zhang et al. "Deterministic entanglement of two neutral atoms via Rydberg blockade". In: *Phys. Rev. A* 82 (3 2010), p. 030306. DOI: 10.1103/PhysRevA.82.030306. URL: https://link.aps.org/doi/10.1103/PhysRevA.82.030306.

[24] B Sun and F Robicheaux. "Numerical study of two-body correlation in a 1D lattice with perfect blockade". In: *New Journal of Physics* 10.4 (2008), p. 045032. DOI: 10.1088/1367-2630/10/4/045032. URL: https://doi.org/10.1088\%2F1367-2630\%2F10\%2F4\%2F045032.

[25] B. Olmos, R. González-Férez, and I. Lesanovsky. "Fermionic Collective Excitations in a Lattice Gas of Rydberg Atoms". In: *Phys. Rev. Lett.* 103 (18 2009), p. 185302. DOI: 10.1103/PhysRevLett.103.185302. URL: https://link.aps.org/doi/10.1103/PhysRevLett.103.185302.

[26] T. Pohl, E. Demler, and M. D. Lukin. "Dynamical Crystallization in the Dipole Blockade of Ultracold Atoms". In: *Phys. Rev. Lett.* 104 (4 2010), p. 043002. DOI: 10.1103/PhysRevLett.104.043002. URL: https://link.aps.org/doi/10.1103/PhysRevLett.104.043002.

[27] Vsevolod F Gantmakher and Valery T Dolgopolov. "Superconductor–insulator quantum phase transition". In: *Physics-Uspekhi* 53.1 (2010), pp. 1–49. DOI: 10.3367/ufne.0180.201001a.0003. URL: https://doi.org/10.3367\%2Fufne.0180.201001a.0003.

[28] Qimiao Si and Frank Steglich. "Heavy Fermions and Quantum Phase Transitions". In: *Science* 329.5996 (2010), pp. 1161–1166. ISSN: 0036-8075. DOI: 10.1126/science.1191195. eprint: https://science.sciencemag.org/content/329/5996/1161.full.pdf. URL: https://science.sciencemag.org/content/329/5996/1161.

[29] Andrei Derevianko. "Feasibility of Cooling and Trapping Metastable Alkaline-Earth Atoms". In: *Phys. Rev. Lett.* 87 (2 2001), p. 023002. DOI: 10.1103/PhysRevLett.87.023002. URL: https://link.aps.org/doi/10.1103/PhysRevLett.87.023002.

[30] G. Audi et al. "The Nubase evaluation of nuclear and decay properties". In: *Nuclear Physics A* 729.1 (2003). The 2003 NUBASE and Atomic Mass Evaluations, pp. 3 –128. ISSN: 0375-9474. DOI: https://doi.org/10.1016/j.nuclphysa.2003.11.001. URL: http://www.sciencedirect.com/science/article/pii/S0375947403018074.

[31] Masaaki Kitagawa et al. "Two-color photoassociation spectroscopy of ytterbium atoms and the precise determinations of $s$-wave scattering lengths". In: *Phys. Rev. A* 77 (1 2008), p. 012719. DOI: 10.1103/PhysRevA.77.012719. URL: https://link.aps.org/doi/10.1103/PhysRevA.77.012719.

[32] Yosuke Takasu et al. "Spin-Singlet Bose-Einstein Condensation of Two-Electron Atoms". In: *Phys. Rev. Lett.* 91 (4 2003), p. 040404. DOI: 10.1103/PhysRevLett.91.040404. URL: https://link.aps.org/doi/10.1103/PhysRevLett.91.040404.

[33] N. Hinkley et al. “An Atomic Clock with 10–18 Instability”. In: *Science* 341.6151 (2013), pp. 1215–1218. ISSN: 0036-8075. DOI: 10.1126/science.1240420. eprint: https://science.sciencemag.org/content/341/6151/1215.full.pdf. URL: https://science.sciencemag.org/content/341/6151/1215.

[34] Yosuke Takasu and Yoshiro Takahashi. “Quantum Degenerate Gases of Ytterbium Atoms”. In: *Journal of the Physical Society of Japan* 78.1 (2009), p. 012001. DOI: 10.1143/JPSJ.78.012001. eprint: https://doi.org/10.1143/JPSJ.78.012001. URL: https://doi.org/10.1143/JPSJ.78.012001.

[35] J. E. Johnson and S. L. Rolston. “Interactions between Rydberg-dressed atoms”. In: *Phys. Rev. A* 82 (3 2010), p. 033412. DOI: 10.1103/PhysRevA.82.033412. URL: https://link.aps.org/doi/10.1103/PhysRevA.82.033412.

[36] Alexander W. Glaetzle et al. “Designing Frustrated Quantum Magnets with Laser-Dressed Rydberg Atoms”. In: *Phys. Rev. Lett.* 114 (17 2015), p. 173002. DOI: 10.1103/PhysRevLett.114.173002. URL: https://link.aps.org/doi/10.1103/PhysRevLett.114.173002.

[37] R. M. W. van Bijnen and T. Pohl. “Quantum Magnetism and Topological Ordering via Rydberg Dressing near Förster Resonances”. In: *Phys. Rev. Lett.* 114 (24 2015), p. 243002. DOI: 10.1103/PhysRevLett.114.243002. URL: https://link.aps.org/doi/10.1103/PhysRevLett.114.243002.

[38] N. Henkel, R. Nath, and T. Pohl. “Three-Dimensional Roton Excitations and Supersolid Formation in Rydberg-Excited Bose-Einstein Condensates”. In: *Phys. Rev. Lett.* 104 (19 2010), p. 195302. DOI: 10.1103/PhysRevLett.104.195302. URL: https://link.aps.org/doi/10.1103/PhysRevLett.104.195302.

[39] F. Maucher et al. “Rydberg-Induced Solitons: Three-Dimensional Self-Trapping of Matter Waves”. In: *Phys. Rev. Lett.* 106 (17 2011), p. 170401. DOI: 10.1103/PhysRevLett.106.170401. URL: https://link.aps.org/doi/10.1103/PhysRevLett.106.170401.

[40] F B Dunning et al. “Recent advances in Rydberg physics using alkaline-earth atoms”. In: *Journal of Physics B: Atomic, Molecular and Optical Physics* 49.11 (2016), p. 112003. DOI: 10.1088/0953-4075/49/11/112003. URL: https://doi.org/10.1088/0953-4075/49/11/112003.

[41] W. Li et al. “A Homonuclear Molecule with a Permanent Electric Dipole Moment”. In: *Science* 334.6059 (2011), pp. 1110–1114. ISSN: 0036-8075. DOI: 10.1126/science.1211255. eprint: https://science.sciencemag.org/content/334/6059/1110.full.pdf. URL: https://science.sciencemag.org/content/334/6059/1110.

[42] J.P. Shaffer, S.T. Rittenhouse, and H.R. Sadeghpour. “Ultracold Rydberg molecules”. In: *Nature Communications* 9 (2018), p. 1965. DOI: 10.1038/s41467-018-04135-6. URL: https://doi.org/10.1038/s41467-018-04135-6.

[43] A. Schwarzkopf, R. E. Sapiro, and G. Raithel. "Imaging Spatial Correlations of Rydberg Excitations in Cold Atom Clouds". In: *Phys. Rev. Lett.* 107 (10 2011), p. 103001. DOI: 10.1103/PhysRevLett.107.103001. URL: https://link.aps.org/doi/10.1103/PhysRevLett.107.103001.

[44] M. P. Robinson et al. "Spontaneous Evolution of Rydberg Atoms into an Ultracold Plasma". In: *Phys. Rev. Lett.* 85 (21 2000), pp. 4466–4469. DOI: 10.1103/PhysRevLett.85.4466. URL: https://link.aps.org/doi/10.1103/PhysRevLett.85.4466.

[45] P. McQuillen et al. "Imaging the evolution of an ultracold strontium Rydberg gas". In: *Phys. Rev. A* 87 (1 2013), p. 013407. DOI: 10.1103/PhysRevA.87.013407. URL: https://link.aps.org/doi/10.1103/PhysRevA.87.013407.

[46] Peter van der Straten Harold J. Metcalf. *Laser Cooling and Trapping*. Vol. 1. Springer, 1999. ISBN: 978-1-4612-1470-0.

[47] S. Tassy. "Sympathetische Kühlung von Ytterbium mit Rubidium". PhD thesis. Heinrich-Heine-Universität Düsseldorf, 2007.

[48] L. Russell et al. "Measurements on release–recapture of cold 85Rb atoms using an optical nanofibre in a magneto-optical trap". In: *Optics Communications* 309 (2013), pp. 313 –317. ISSN: 0030-4018. DOI: https://doi.org/10.1016/j.optcom.2013.07.080. URL: http://www.sciencedirect.com/science/article/pii/S0030401813007189.

[49] U. Fano. "Unified treatment of perturbed series, continuous spectra and collisions∗†". In: *J. Opt. Soc. Am.* 65.9 (1975), pp. 979–987. DOI: 10.1364/JOSA.65.000979. URL: http://www.osapublishing.org/abstract.cfm?URI=josa-65-9-979.

[50] C L Vaillant, M P A Jones, and R M Potvliege. "Multichannel quantum defect theory of strontium bound Rydberg states". In: *Journal of Physics B: Atomic, Molecular and Optical Physics* 47.15 (2014), p. 155001. DOI: 10.1088/0953-4075/47/15/155001. URL: https://doi.org/10.1088/0953-4075/47/15/155001.

[51] Wenhui Li et al. "Millimeter-wave spectroscopy of cold Rb Rydberg atoms in a magneto-optical trap: Quantum defects of the ns, np, and nd series". In: *Phys. Rev. A* 67 (5 2003), p. 052502. DOI: 10.1103/PhysRevA.67.052502. URL: https://link.aps.org/doi/10.1103/PhysRevA.67.052502.

[52] Luc Couturier et al. "Measurement of the strontium triplet Rydberg series by depletion spectroscopy of ultracold atoms". In: *Phys. Rev. A* 99 (2 2019), p. 022503. DOI: 10.1103/PhysRevA.99.022503. URL: https://link.aps.org/doi/10.1103/PhysRevA.99.022503.

[53] J. L. Dehmer and U. Fano. "Phase-Amplitude Method in Atomic Physics. I. Basic Formulas for an Electron in an Ionic Potential". In: *Phys. Rev. A* 2 (2 1970), pp. 304–309. DOI: 10.1103/PhysRevA.2.304. URL: https://link.aps.org/doi/10.1103/PhysRevA.2.304.

[54] W. E. Cooke and C. L. Cromer. "Multichannel quantum-defect theory and an equivalent N-level system". In: *Phys. Rev. A* 32 (5 1985), pp. 2725–2738. DOI: 10.1103/PhysRevA.32.2725. URL: https://link.aps.org/doi/10.1103/PhysRevA.32.2725.

[55] W. E. Cooke and C. L. Cromer. "Multichannel quantum-defect theory and an equivalent N-level system". In: *Phys. Rev. A* 32 (5 1985), pp. 2725–2738. DOI: 10.1103/PhysRevA.32.2725. URL: https://link.aps.org/doi/10.1103/PhysRevA.32.2725.

[56] M Aymar. "Eigenchannel R-matrix calculation of the photoabsorption spectrum of strontium". In: *Journal of Physics B: Atomic and Molecular Physics* 20.24 (1987), pp. 6507–6529. DOI: 10.1088/0022-3700/20/24/005. URL: https://doi.org/10.1088\%2F0022-3700\%2F20\%2F24\%2F005.

[57] J Mitroy, M S Safronova, and Charles W Clark. "Theory and applications of atomic and ionic polarizabilities". In: *Journal of Physics B: Atomic, Molecular and Optical Physics* 43.20 (2010), p. 202001. DOI: 10.1088/0953-4075/43/20/202001. URL: https://doi.org/10.1088/0953-4075/43/20/202001.

[58] David H Meyer et al. "Assessment of Rydberg atoms for wideband electric field sensing". In: *Journal of Physics B: Atomic, Molecular and Optical Physics* 53.3 (2020), p. 034001. DOI: 10.1088/1361-6455/ab6051. URL: https://doi.org/10.1088\%2F1361-6455\%2Fab6051.

[59] T. Wang et al. "Superradiance in ultracold Rydberg gases". In: *Phys. Rev. A* 75 (3 2007), p. 033802. DOI: 10.1103/PhysRevA.75.033802. URL: https://link.aps.org/doi/10.1103/PhysRevA.75.033802.

[60] Kilian Singer et al. "Long-range interactions between alkali Rydberg atom pairs correlated to thens–ns,np–np andnd–nd asymptotes". In: *Journal of Physics B: Atomic, Molecular and Optical Physics* 38.2 (2005), S295–S307. DOI: 10.1088/0953-4075/38/2/021. URL: https://doi.org/10.1088/0953-4075/38/2/021.

[61] Robert J. Le Roy. "Long-Range Potential Coefficients From RKR Turning Points: C6 and C8 for B(3ΠOu+)-State Cl2, Br2, and I2". In: *Canadian Journal of Physics* 52.3 (1974), pp. 246–256. DOI: 10.1139/p74-035. eprint: https://doi.org/10.1139/p74-035. URL: https://doi.org/10.1139/p74-035.

[62] N. Šibalić et al. "ARC: An open-source library for calculating properties of alkali Rydberg atoms". In: *Computer Physics Communications* 220 (2017), pp. 319 –331. ISSN: 0010-4655. DOI: https://doi.org/10.1016/j.cpc.2017.06.015. URL: http://www.sciencedirect.com/science/article/pii/S0010465517301972.

[63] Bastian Scheppers. "Aufbau einer Apparatur für Experimente mit lasergekühltem Ytterbium". Master thesis. Heinrich-Heine-Universität Düsseldorf, 2016.

[64] Gregor Mura. "Optimierung und Charakterisierung einer transportablen optischen Gitteruhr mit Ytterbium". PhD thesis. Heinrich-Heine-Universität Düsseldorf, 2015.

[65] M. Clemens and T. Weiland. "Discrete Electromagnetism with the Finite Integration Technique". In: *Progress In Electromagnetics Research* 32 (2001), pp. 65–87. DOI: 10.2528/PIER00080103. URL: http://www.jpier.org/PIER/pier.php?paper=00080103.

[66] Aviv Keshet and Wolfgang Ketterle. "A distributed, graphical user interface based, computer control system for atomic physics experiments". In: *Review of Scientific Instruments* 84.1 (Jan. 2013), p. 015105. ISSN: 1089-7623. DOI: 10.1063/1.4773536. URL: http://dx.doi.org/10.1063/1.4773536.

[67] Nils Nemitz. "Production and spectroscopy of ultracold YbRb* molecules". PhD thesis. Heinrich-Heine-Universität Düsseldorf, 2008.

[68] J Migdalek and W E Baylis. "Relativistic transition probabilities and lifetimes of low-lying levels in ytterbium". In: *Journal of Physics B: Atomic, Molecular and Optical Physics* 24.4 (1991), pp. L99–L102. DOI: 10.1088/0953-4075/24/4/001. URL: https://doi.org/10.1088\%2F0953-4075\%2F24\%2F4\%2F001.

[69] T. Kuwamoto et al. "Magneto-optical trapping of Yb atoms using an intercombination transition". In: *Phys. Rev. A* 60 (2 1999), R745–R748. DOI: 10.1103/PhysRevA.60.R745. URL: https://link.aps.org/doi/10.1103/PhysRevA.60.R745.

[70] T. Loftus et al. "Power-dependent loss from an ytterbium magneto-optic trap". In: *Phys. Rev. A* 61 (5 2000), p. 051401. DOI: 10.1103/PhysRevA.61.051401. URL: https://link.aps.org/doi/10.1103/PhysRevA.61.051401.

[71] J. E. Bjorkholm. "Collision-limited lifetimes of atom traps". In: *Phys. Rev. A* 38 (3 1988), pp. 1599–1600. DOI: 10.1103/PhysRevA.38.1599. URL: https://link.aps.org/doi/10.1103/PhysRevA.38.1599.

[72] Thierry Chanelière et al. "Extra-heating mechanism in Doppler cooling experiments". In: *J. Opt. Soc. Am. B* 22.9 (2005), pp. 1819–1828. DOI: 10.1364/JOSAB.22.001819. URL: http://josab.osa.org/abstract.cfm?URI=josab-22-9-1819.

[73] M. D. Lukin et al. "Dipole Blockade and Quantum Information Processing in Mesoscopic Atomic Ensembles". In: *Phys. Rev. Lett.* 87 (3 2001), p. 037901. DOI: 10.1103/PhysRevLett.87.037901. URL: https://link.aps.org/doi/10.1103/PhysRevLett.87.037901.

[74] Alexander Batär. "Erzeugung und Charakterisierung ultrakalter Rubidium- und Ytterbiumatome - Auf dem Weg zu einem gemischten Quantengas". PhD thesis. Heinrich-Heine-Universität Düsseldorf, 2005.

[75] T.W. Hansch and B. Couillaud. "Laser frequency stabilization by polarization spectroscopy of a reflecting reference cavity". In: *Optics Communications* 35.3 (1980), pp. 441 –444. ISSN: 0030-4018. DOI: https://doi.org/10.1016/0030-4018(80)90069-3. URL: http://www.sciencedirect.com/science/article/pii/0030401880900693.

[76] Henri Lehec. "Rydberg spectrocopy and isolated core excitation of ultra-cold ytterbium atoms". Theses. Université Paris-Saclay, Dec. 2017. URL: https://tel.archives-ouvertes.fr/tel-01698466.

[77] Cristian Bruni. "Exploring strategies for the production of ultracold RbYb molecules in conservative traps". PhD thesis. Heinrich-Heine-Universität Düsseldorf, 2015.

[78] Sebastian Weber et al. "Calculation of Rydberg interaction potentials". In: *Journal of Physics B: Atomic, Molecular and Optical Physics* 50.13 (2017), p. 133001. DOI: 10.1088/1361-6455/aa743a. URL: https://doi.org/10.1088\%2F1361-6455\%2Faa743a.

[79] M J Seaton. "Quantum defect theory". In: *Reports on Progress in Physics* 46.2 (1983), pp. 167–257. DOI: 10.1088/0034-4885/46/2/002. URL: https://doi.org/10.1088\%2F0034-4885\%2F46\%2F2\%2F002.

[80] David Robert Bates, Agnete Damgaard, and Harrie Stewart Wilson Massey. "The calculation of the absolute strengths of spectral lines". In: *Philosophical Transactions of the Royal Society of London. Series A, Mathematical and Physical Sciences* 242.842 (1949), pp. 101–122. DOI: 10.1098/rsta.1949.0006. eprint: https://royalsocietypublishing.org/doi/pdf/10.1098/rsta.1949.0006. URL: https://royalsocietypublishing.org/doi/abs/10.1098/rsta.1949.0006.

[81] J Picart et al. "Calculation of octupole radial integrals in the Coulomb approximation". In: *Journal of Physics B: Atomic, Molecular and Optical Physics* 23.5 (1990), pp. L61–L65. DOI: 10.1088/0953-4075/23/5/001. URL: https://doi.org/10.1088\%2F0953-4075\%2F23\%2F5\%2F001.

[82] S Klarsfeld. "A modified Bates-Damgaard method". In: *Journal of Physics B: Atomic, Molecular and Optical Physics* 21.24 (1988), pp. L717–L721. DOI: 10.1088/0953-4075/21/24/002. URL: https://doi.org/10.1088\%2F0953-4075\%2F21\%2F24\%2F002.

[83] Elizabeth J. Robertson et al. "ARC 3.0: An expanded Python toolbox for atomic physics calculations". In: *arXiv e-prints*, arXiv:2007.12016 (July 2020), arXiv:2007.12016. arXiv: 2007.12016 [physics.atom-ph].

[84] D. R. Inglis and E. Teller. "Ionic Depression of Series Limits in One-Electron Spectra." In: *apj* 90 (Oct. 1939), p. 439. DOI: 10.1086/144118.

[85] Y. P. Varshni. "Electron density in the emission-line region of Wolf-Rayet stars". In: *Astrophysics and Space Science* 56 (1978), pp. 385–388. DOI: AstrophysicsandSpaceScience. URL: http://articles.adsabs.harvard.edu/cgi-bin/nph-iarticle_query?1978Ap\%26SS..56..385V&data_type=PDF_HIGH&whole_paper=YES&type=PRINTER&filetype=.pdf.

[86] Sha Li and R. R. Jones. "Ionization of Excited Atoms by Intense Single-Cycle THz Pulses". In: *Phys. Rev. Lett.* 112 (14 2014), p. 143006. DOI: 10.1103/PhysRevLett.112.143006. URL: https://link.aps.org/doi/10.1103/PhysRevLett.112.143006.

[87] C.O. Reinhold et al. "Creating and probing coherent atomic states". In: *Nuclear Instruments and Methods in Physics Research Section B: Beam Interactions with Materials and Atoms* 132.2 (1997). Atomic Collisions, pp. 316 –325. ISSN: 0168-583X. DOI: https://doi.org/10.1016/S0168-583X(97)00433-3. URL: http://www.sciencedirect.com/science/article/pii/S0168583X97004333.

[88] Baochun Yang and Francis Robicheaux. "Field-ionization threshold and its induced "ionization window" phenomenon for Rydberg atoms in a short single-cycle pulse". In: *Physical Review A* 90 (Oct. 2014). DOI: 10.1103/PhysRevA.90.063413.

[89] T. F. Gallagher et al. "Field ionization of highly excited states of sodium". In: *Phys. Rev. A* 16 (3 1977), pp. 1098–1108. DOI: 10.1103/PhysRevA.16.1098. URL: https://link.aps.org/doi/10.1103/PhysRevA.16.1098.

[90] I. I. Beterov et al. "Quasiclassical calculations of blackbody-radiation-induced depopulation rates and effective lifetimes of Rydberg $nS$, $nP$, and $nD$ alkali-metal atoms with $n \leq 80$". In: *Phys. Rev. A* 79 (5 2009), p. 052504. DOI: 10.1103/PhysRevA.79.052504. URL: https://link.aps.org/doi/10.1103/PhysRevA.79.052504.

[91] C L Vaillant, M P A Jones, and R M Potvliege. "Multichannel quantum defect theory of strontium bound Rydberg states". In: *Journal of Physics B: Atomic, Molecular and Optical Physics* 47.15 (2014), p. 155001. DOI: 10.1088/0953-4075/47/15/155001. URL: https://doi.org/10.1088\%2F0953-4075\%2F47\%2F15\%2F155001.

[92] Peter Schauß et al. "Observation of spatially ordered structures in a two-dimensional Rydberg gas". In: *Nature* 491 (10 2012), pp. 87–91. DOI: 10.1038/nature11596. URL: https://doi.org/10.1038/nature11596.

[93] Vladislav Gavryusev et al. "Interaction Enhanced Imaging of Rydberg P states". In: *The European Physical Journal Special Topics* 225 (15 2016), pp. 2863–2889. DOI: 10.1140/epjst/e2015-50339-8. URL: https://doi.org/10.1140/epjst/e2015-50339-8.

[94] T. L. Nguyen et al. "Towards Quantum Simulation with Circular Rydberg Atoms". In: *Phys. Rev. X* 8 (1 2018), p. 011032. DOI: 10.1103/PhysRevX.8.011032. URL: https://link.aps.org/doi/10.1103/PhysRevX.8.011032.

[95] Seth T. Rittenhouse and H. R. Sadeghpour. "Ultracold Giant Polyatomic Rydberg Molecules: Coherent Control of Molecular Orientation". In: *Phys. Rev. Lett.* 104 (24 2010), p. 243002. DOI: 10.1103/PhysRevLett.104.243002. URL: https://link.aps.org/doi/10.1103/PhysRevLett.104.243002.

[96] Seth T. Rittenhouse and H. R. Sadeghpour. "Ultracold Giant Polyatomic Rydberg Molecules: Coherent Control of Molecular Orientation". In: *Phys. Rev. Lett.* 104 (24 2010), p. 243002. DOI: 10.1103/PhysRevLett.104.243002. URL: https://link.aps.org/doi/10.1103/PhysRevLett.104.243002.

# Danksagung

Zu guter Letzt möchte ich mich bei allen bedanken, die mich bei der Umsetzung dieser Arbeit unterstützt haben. Mein besonderer Dank gilt natürlich allen Mitarbeitern des Instituts für Experimentalphysik an der Universität Düsseldorf. Einige Personen möchte ich allerdings besonders hervorheben:

An erster Stelle bedanke ich mich natürlich bei Prof. Axel Görlitz, der mir während meiner Dissertation mit seiner offenen und kompetenten Art immer mit Rat und Tat zur Seite stand. Ich möchte mich auch für das sorgfältige Korrekturlesen dieser Arbeit bedanken. Er hat mit seiner konstruktiven Kritik diese Arbeit maßgeblich geprägt. Außerdem bedanke ich mich für die Übernahme und zügige Fertigstellung des Hauptberichtes.

Herrn Prof. Thomas Heinzel danke ich dafür, dass er meine Promotion als Mentor begleitet hat. Ganz besonders bedanke ich mich für die Übernahme des Koreferates und die schnelle Fertigstellung des Gutachtens.

Besonders bedanken möchte ich bei meinem langjährigen Freund und Vorgänger Bastian Schepers. Er hat mit seiner Masterarbeit den soliden Grundstein für das Experiment gelegt, auf dem diese Arbeit fußt. Die gemeinsame Arbeit an dem Experiment, auch wenn sie nur kurz war, hat mir sehr viel Spaß bereitet.

Gleiches gilt auch für meinen Nachfolger Alexander Miehtke. Es hat mir sehr viel Freude bereitet ihm bei seiner Masterarbeit zu unterstützen und ich weiß, dass das Experiment bei ihm in guten Händen ist. Ich wünsche ihm auf seinem Weg alles Gute und viel Erfolg! Außerdem danke ich ihm für das sorgfältige Korrekturlesen und die konstruktive Kritik, die diese Arbeit mit geformt hat.

Nicht unerwähnt dürfen natürlich all jene sein, die mich so herzlich in die Arbeitsgruppe aufgenommen haben und mit denen ich sehr viel Zeit im Labor und in Boulderhallen verbracht habe. Danke an Tobias Franzen, der mir mit seinem schier unendlichen Wissen bei unzähligen Fragestellungen weitergeholfen hat. Danke auch an Bastian Pollklesener dafür, dass er mir das Bouldern nähergebracht hat. Besonders bedanken möchte ich mich auch bei meinem Büronachbar Christian Sillus für die unterhaltsame Zeit und für die Unterstützung. Er hat mit seiner Masterarbeit einen nicht unwesentlichen Teil zu dieser Arbeit beigetragen. Desweitern will ich all denen danken, die ich während meiner Promotion betreuen durfte und die mich bei meiner Arbeit unterstützt haben. Vielen Dank an Apoorva Hegde, Mariya Krasteva und Mustafa Jumaah.

Eine Person darf natürlich nicht unerwähnt bleiben! Ralph Stephan, er ist der Techniker der Arbeitsgruppe und damit das Herz und die Seele. Ich kann gar nicht aufzählen wie oft er mir mit seiner offenen und zuvorkommenden Art weitergeholfen hat. Ohne seine Hilfe wäre diese Arbeit nicht möglich gewesen, vielen Dank!

Ich möchte mich natürlich auch bei den Menschen bedanken, die mich außerhalb des Labors unterstützt haben. Ihr Anteil an dieser Arbeit ist gar nicht zu messen!

Ich möchte mich bei meiner Mutter, bei meinem Bruder und bei meinem Stiefvater bedanken. Ihr standet mir immer zur Seite und habt mir Kraft und Mut gegeben. Auch vielen Dank für das Korrekturlesen, Michael!

Unermesslich dankbar bin ich auch dir Greta dafür, dass du mir die Kraft und den Rückhalt gegeben hast weiter zu machen, um diese Arbeit abschließen zu können, vielen Dank!

Abschließend möchte ich mich bei allen nochmal für die lehrreiche, unterhaltsame und abwechslungsreiche Zeit bedanken. Es hat mir sehr viel Spaß gemacht mit euch zusammen zu arbeiten und darüber hinaus. Vielen Dank!

## Erklärung

Hiermit versichere ich, dass ich die vorliegende Arbeit selbständig angefertigt und dabei nur die angegebenen Quellen und Hilfsmittel benutzt habe. Zitate habe ich unter Angabe der Quellen eindeutig kenntlich gemacht.

Düsseldorf, den 20. June 2022

---

(Christian Halter)